

EARTHQUAKE FOCAL MECHANISM AND STRESS TENSOR ANALYSIS
ALONG THE CENTRAL SEGMENT OF THE NORTH ANATOLIAN FAULT

A THESIS SUBMITTED TO
THE GRADUATE SCHOOL OF NATURAL AND APPLIED SCIENCES
OF
MIDDLE EAST TECHNICAL UNIVERSITY

BY

EZGİ KARASÖZEN

IN PARTIAL FULFILLMENT OF THE REQUIREMENTS FOR
THE DEGREE OF MASTER OF SCIENCE
IN GEOLOGICAL ENGINEERING

JULY 2010

Approval of the thesis:

**EARTHQUAKE FOCAL MECHANISM AND STRESS TENSOR ANALYSIS
ALONG THE CENTRAL SEGMENT OF THE NORTH ANATOLIAN FAULT**

submitted by **EZGİ KARASÖZEN** in partial fulfillment of the requirements for the degree of **Master of Science in Geological Engineering Department, Middle East Technical University** by,

Prof. Dr. Canan Özgen
Dean, **Graduate School of Natural and Applied Sciences**

Prof. Dr. Zeki Çamur
Head of Department, **Geological Engineering**

Assist. Prof. Dr. A. Arda Özacar
Supervisor, **Geological Engineering Dept., METU**

Assoc. Prof. Dr. Nuretdin Kaymakcı
Co-Supervisor, **Geological Engineering Dept., METU**

Examining Committee Members:

Prof. Dr. Erdin Bozkurt
Geological Engineering Dept., METU

Assist. Prof. Dr. A. Arda Özacar
Geological Engineering Dept., METU

Assoc. Prof. Dr. Nuretdin Kaymakcı
Geological Engineering Dept., METU

Assoc. Prof. Dr. F. Bora Rojay
Geological Engineering Dept., METU

Assist. Prof. Dr. Gonca ÖRGÜLÜ
Geophysical Engineering Dept., İTÜ

Date: 19.07.2010

I hereby declare that all information in this document has been obtained and presented in accordance with academic rules and ethical conduct. I also declare that, as required by these rules and conduct, I have fully cited and referenced all material and results that are not original to this work.

Name, Last name: Ezgi Karasözen

Signature:

ABSTRACT

EARTHQUAKE FOCAL MECHANISM AND STRESS TENSOR ANALYSIS ALONG THE CENTRAL SEGMENT OF THE NORTH ANATOLIAN FAULT

Karasözen, Ezgi

M.Sc., Department of Geological Engineering

Supervisor: Assist. Prof. Dr. A. Arda Özacar

Co-Supervisor: Assoc. Prof. Dr. Nuretdin Kaymakcı

July 2010, 205pages

The North Anatolian Fault (NAF) is one of the world's largest active continental strike-slip faults, and forms the northern margin of the Anatolian plate. Although its geologic and geomorphologic features are well defined, crustal deformation and associated seismicity around central segment of the NAF is relatively less-known. In this study, we analyzed locations and focal mechanisms of 172 events with magnitude ≥ 3 , which are recorded by 39 broadband seismic stations deployed by the North Anatolian Passive Seismic Experiment (2005-2008). Distribution of the events shows that the local seismicity in the area is widely distributed, suggesting a widespread continental deformation, particularly in the southern block. For the entire data set, *P*- and *S*- arrival times are picked and events are relocated using the HYPOCENTER program. Then, relocated events which have a good azimuthal coverage with a maximum gap of 120° and at least 13 *P*- wave readings are selected and 1-D inversion algorithm, VELEST, is used to derive the 1-D seismic velocity model of the region. The final model with updated locations is later put together to the FOCMEC program, to obtain focal mechanisms solutions. In this step, an iterative scheme is applied by increasing the number of data errors. To obtain more unique solutions, first motions of *P* and *SH*

phases are used along with SH/P amplitude ratios. Resultant 109 well-constrained focal mechanisms later used to perform stress tensor inversion across the region.

Our focal mechanisms suggest a dominant strike-slip deformation along two major fault sets in the region. In the east, E-W trending splays (Ezinepazarı, Almus, and Laçın Kızılırmak) show right-lateral strike-slip motion similar to the NAF whereas in the west, N-S trending faults (Dodurga, Eldivan) show left lateral strike-slip motion. Overall, stress orientations are found as: maximum principal stress, σ_1 , is found to be subhorizontal striking NW-SE, the intermediate principle stress, σ_2 , is vertically orientated and the minimum principal stress, σ_3 , is found to be NE –SW striking, consistent with the strike-slip regime of the region.

Keywords: North Anatolian Fault, hypocenter relocation, strike-slip faults, stress tensor inversion

ÖZ

KUZEY ANADOLU FAYI ORTA KESİMİNDEKİ DEPREMLERİN ODAK MEKANİZMA VE STRES TENSÖR ANALİZİ

Karasözen, Ezgi

Yüksek Lisans, Jeoloji Mühendisliği Bölümü

Tez Yöneticisi: Yrd. Doç. Dr. A. Arda Özacar

Ortak Tez Yöneticisi: Doç. Dr. Nuretdin Kaymakcı

Temmuz 2010, 205 sayfa

Kuzey Anadolu Fay hattı (KAF) dünyanın en büyük aktif kıtasal doğrultu atımlı faylarından biridir ve Anadolu Levhası'nın kuzey kenarını oluşturur. Jeolojik ve jeomorfolojik özellikleri oldukça iyi tanınmasına rağmen, KAF'nin orta kısmındaki kabuksal bozulmalar ile ilgili depremselliği görece az bilinmektedir. Bu çalışmada, Kuzey Anadolu Pasif Sismik Deneyi (2005-2008) kapsamında yerleştirilmiş 39 genişbant sismik istasyonunda kaydedilmiş, büyüklüğü 3 ve 3'den büyük 172 jeolojik olayın konumu ve odak mekanizması analiz edilmiştir. Jeolojik olayların dağılımına göre yerel depremsellik geniş bir alanda yayılım göstermekte ve özellikle güney blokta yaygın bir kıtasal bozulmaya işaret etmektedir. Tüm veri kümesi için *P*- ve *S*- varış zamanları seçilmiş ve olaylar HYPOCENTER programı kullanılarak yeniden konumlandırılmıştır. Ardından, en fazla 120° boşluk ve en az 13 *P*- dalga okuması ile iyi azimut kapsamına sahip olan yeniden konumlandırılmış olaylar seçilmiş ve alanın 1 boyutlu sismik hız modelini oluşturmak için 1 boyutlu dönüşüm algoritması olan VELEST kullanılmıştır. Son model, güncellenmiş konumlarla birlikte odak mekanizmalarının çözümlerinin elde edilmesi için FOCMEC programında çalıştırılmıştır. Bu aşamada veri hatası sayısı arttırılarak bir tekrarlamalı taslak uygulanmıştır. Daha özgün çözümler elde etmek için *P*'nin ilk hareketleri ve SH fazları SH/P dalga genişlik oranları ile birlikte kullanılmıştır. Eldeki 109 adet iyi belirlenmiş

odak mekanizması, daha sonra bölgenin gerilme tensörü dönüşümünü elde etmek için kullanılmıştır.

Bizim odak mekanizmalarımız, bölgede iki ana fay seti boyunca baskın bir doğrultu atımlı deformasyon olduğunu önermektedir. Doğuda, D-B gidişli kollar (Ezinepazarı, Almus ve Laçın Kızılırmak) KAF'a benzer şekilde sağ-yönlü doğrultulu atım hareketi gösterirken; batıda, K-G gidişli faylar (Dodurga, Eldivan) sol-yönlü doğrultulu atım hareketi göstermektedir. Bütünde, gerilme yönelimleri, bölgenin doğrultu atımlı rejimiyle tutarlı olarak şu şekilde bulunmuştur: maksimum asal gerilme, σ_1 , yataya yakın KB-GD doğrultusundadır; ortaç asal gerilme, σ_2 , dikey doğrultudadır; minimum asal gerilme, σ_3 , ise KD-GB doğrultusundadır.

Anahtar sözcükler: Kuzey Andolu Fayı, odak mekanizma çözümleri, doğrultu atımlı faylar, gerilme tensörü dönüşümü

To My Parents Zerrin & Bülent

ACKNOWLEDGEMENTS

First of all, I would like to thank my advisor Assist. Prof. Dr. A. Arda Özacar for his invaluable guidance, critical vision, motivation, understanding and kindness throughout the course of my M.Sc. studies.

I would also like to express my thanks to Assoc.Prof.Dr. Bora Rojay, Assoc.Prof.Dr. M. Lütfi Süzen, and my co-supervisor Assoc. Prof. Dr. Nuretdin Kaymakçı.

Special thanks are extended to Berk Biryol, who helped me a lot throughout the difficulties I encountered in the initial stages of this thesis.

I want to thank to my “roomie” Kıvanç Yücel, who shared all the stages of this thesis, providing me a joyful working atmosphere. Also, I would like to thank my dear friend Ezgi Ünal for her continuous support and endless motivation.

I would like to thank to my dear F.R.I.E.N.D.S., Ezgi Tinçer, Merve Genç, Çiğdem Cankara and Gizem Tinçer, it would be very hard to accomplish this study without them.

I would like to thank to Çağdaş Öztük for all the happiness and cheering he provided, he kept me sane and made this thesis possible. I would be “Lost” without him.

Finally, I am very grateful to my dearest parents Zerrin and Bülent Karasözen, who truly merit the dedication of this thesis. I am really very lucky to have them.

TABLE OF CONTENTS

ABSTRACT	iv
ÖZ	vi
ACKNOWLEDGEMENTS	ix
TABLE OF CONTENTS	x
LIST OF TABLES	xii
LIST OF FIGURES	xiii
CHAPTER	
1. INTRODUCTION	1
1.1 Purpose and Scope	1
1.2 Data and Methods of the Study	2
1.3 Organization of the Thesis	3
2. TECTONIC SETTING	4
2.1 Geology of the Region	4
2.2 North Anatolian Fault Zone	7
2.2.1 Major Splays	10
2.3 Seismicity of the Region	11
2.3.1 Earthquake statistics	18
2.3.2 Focal Mechanisms	20
3. EARTHQUAKE RELOCATION	24

3.1 Data Processing	24
3.2 Earthquake Relocation	26
3.3 Calculation of 1-D Crustal Velocity Model.....	28
3.4 Results.....	31
3.4.1 Velocity Model	31
3.4.2 Station Delays	33
3.4.3 Earthquake Locations	34
4. FOCAL MECHANISMS AND STRESS TENSOR ANALYSIS	38
4.1 Focal Mechanism Determination.....	38
4.2 Stress Tensor Inversion.....	46
4.3 Results.....	47
4.3.1. Çorum Cluster.....	65
5. RESULTS AND DISCUSSION	69
REFERENCES.....	73
<u>APPENDICES</u>	<u>82</u>
A. TABLES.....	82
B. OUTPUTS OF CALCULATED FOCAL MECHANISMS (Attached in CD)....	96

LIST OF TABLES

TABLES

Table 1. Initial trial velocity models (IASP, Toksoz et al., 2003).	28
Table 2. Selected 1-D velocity model.	32
Table 3. Tectonic regime assignment (Zoback, 1992; taken from World Stress Map Project).	52

LIST OF FIGURES

FIGURES

- Figure 1. Simplified tectonic map of Turkey (modified from Bozkurt, 2001). The box indicates the location of the study area and blue diamonds represents broadband seismic stations of North Anatolian Passive Seismic Experiment....2
- Figure 2. Simplified geological map of the study area (M.T.A. 1:500000) geological map of Turkey; sutures and faults are compiled from Bozkurt 2001 and Rojay, B., Kaymakcı, N., personal communication, 2010). IAES= İzmir-Ankara-Erzincan Suture, IPS= Inner Pontide Suture, ITS = Inner Tauride Suture.5
- Figure 3. Topographic map showing surface ruptures along the central segment of NAF with seismic station locations. Ruptured segments of the NAF during major earthquakes of the last century are color coded and related fault displacements taken from USGS are shown in the inset figure. NAFZ= North Anatolian Fault Zone, LKFZ= Laçın-Kızılırmak Fault Zone, EZFZ= Ezinepazarı Fault Zone AFZ= Almus Fault Zone, DFZ= Dodurga Fault Zone, EFZ= Eldivan Fault Zone.8
- Figure 4. Distribution of local seismicity within the study area that took place during 1990-2004, with magnitude ≥ 3 (KOERI). The earthquakes are scaled to their magnitudes. White stars indicates major earthquakes of the past century. Diamonds denote seismic stations and major faults are shown by black line. . 12
- Figure 5. Distribution of local seismicity within the study area that took place during 2004-2009, with magnitude ≥ 1 (KOERI). The earthquakes are scaled to their magnitudes. White stars indicates major earthquakes of the past century..... 14
- Figure 6. Cumulative moment release of the combined catalog, plotted as a function of time. 15
- Figure 7. Temporal distribution of the earthquakes, plotted as a function of magnitude. 16

Figure 8. Time histogram of the combined catalog.	16
Figure 9. Quarry blast mapping of the earthquakes.	17
Figure 10. Frequency-magnitude distribution of the combined catalog. Both the cumulative (squares) and non-cumulative (triangles) plots are shown.	19
Figure 11. Manually picked frequency-magnitude distribution of the combined catalog. Circles represent cumulative plot.	20
Figure 12. Rake-based ternary diagram of 36 earthquakes that occurred in the study area between 1939 and 2010.	21
Figure 13. Fault plane solutions of 36 earthquakes that occurred in the study area between 1939 and 2010, with $M \geq 4.3$. The focal mechanisms are scaled to their magnitudes. For the sources and parameters of the solutions, see Appendices 1 and 2.	22
Figure 14. Distribution of all <i>P</i> - and <i>T</i> -axes orientations of 36 earthquakes that occurred in the study area between 1939 and 2010. Black diamonds show <i>T</i> -axes and white diamonds show <i>P</i> -axes.	23
Figure 15. Example for emergent (left) and impulsive (right) arrivals of two different events, recorded by the same station.	25
Figure 16. Wadati diagram for all events.	25
Figure 17. Example of a record section of well-picked phases.	26
Figure 18. Wadati diagram of events after the elimination of the phases lying far of the main trend. The V_p/V_s ratio is 1.73.	27
Figure 19. Wadati diagram after the selection of events for the velocity inversion. The V_p/V_s ratio is 1.73.	29
Figure 20. Initial trial velocity models (IASP, Toksoz et al., 2003).	30
Figure 21. Velocity models showing the results of first inversion and the average model selected from this result.	30
Figure 22. Velocity models resulted from the second inversion.	31
Figure 23. Selected 1-D velocity model.	32
Figure 24. <i>P</i> -wave station corrections for the final 1-D <i>P</i> -wave velocity model. Red circles and green triangles on the map show the negative and positive station	

	delays relative to the reference station, respectively. The reference station KGAC is marked by a black diamond. The correction values equal to 0.0 s are shown as inverse triangle. Sizes of the all symbols are scaled to correction values, except reference station. See Table A. 4 for detailed information.	34
Figure 25.	Epicentral and hypocentral shifts relative to the preliminary hypocenter location, after the final earthquake relocation. New epicentral locations are shown with red circles (see Table A.4). The vectors indicate epicentral shifts between initial and final locations. Major faults are shown by gray line. See table A. 5 for detailed information.....	35
Figure 26.	Comparison of RMS values between initial and final relocation results of all 172 earthquakes.	36
Figure 27.	Epicentral and hypocentral shifts relative to the preliminary hypocenter location, after the final earthquake relocation of Çorum cluster.....	37
Figure 28.	Schematic view illustrating the basic concept of the determination of focal mechanism from P- wave first motions, for a strike-slip earthquake on a vertical fault (Stein and Wysession, 2003).	39
Figure 29.	An example of a well-determined focal mechanism solution. Each P- and SH- waveform data used for determination of this solution are shown in vertical traces. First motions of P- and SH- waves are marked with black and green vertical lines, respectively. Red dots indicate compressional (up) arrivals and blue dots indicate tensional (down) arrivals. Calculated SH/P ratios are given also, when clear SH picks are available.	40
Figure 30.	Fault geometry and radiation amplitude patterns of P and S waves in the $x_1 - x_3$ plane (Stein and Wysession, 2003).....	42
Figure 31.	An example of an output plot that summarizes all the possible solution mechanisms and related data.	45
Figure 32.	Comparison of our resultant focal mechanism for event 1 with solutions of Regional and Harvard Centroid Moment tensor (CMT) solutions.	48
Figure 33.	Ternary diagram of resultant 109 focal mechanisms determined in this study.	49

Figure 34. Fault plane solutions of 109 earthquakes determined in this study. The focal mechanisms are scaled to their magnitudes. For the fault plane information, see Table A. 6. White box defines the boundaries of the Çorum cluster.	50
Figure 35. Distribution of all <i>P</i> - and <i>T</i> -axes orientations calculated in this study together with their average value are shown in stereographic projection. Black diamonds show <i>T</i> - axes and white diamonds show <i>P</i> -axes. Average values are of <i>P</i> - and <i>T</i> -axes are indicated by black and white stars, respectively. See Table A. 7 for detailed information.	52
Figure 36. Focal mechanism data represented as <i>P</i> -axes orientations with colored coded faulting classes. Black lines define the earthquakes that can not be classified. NF= normal faulting, NS= predominately normal faulting with strike–slip component, SS= strike-slip faulting, TS= predominately thrust faulting with strike–slip component, TF= thrust faulting.	53
Figure 37. Focal mechanism data represented as <i>T</i> -axes orientations with colored-coded faulting classes.	54
Figure 38. Histogram showing the type of faulting.	54
Figure 39. Stress inversion (a) and histogram of Φ values versus frequency (b) results of 109 focal mechanisms determined in this study, by Micheal’ s method.	55
Figure 40. Stress inversion result of 109 focal mechanisms determined in this study, by Gephart’s method.	56
Figure 41. (a) Locations of 109 earthquakes and (b) resulting earthquake resolution over a.	57
Figure 42. Orientation of the trend of σ_1 (bars) showing, (a) faulting types (b) variance of the stress tensor at each node, for 109 focal mechanisms determined in this study. Gridding parameters are: 0.1x0.1 degree spacing and constant number of events at each node is 3. Faulting regimes are represented by different colors as shown in the legend. Gray lines define the earthquakes that can not be classified.	58
Figure 43. Orientation of the trend of σ_1 (bars) showing, (a) faulting types (b) variance of the stress tensor at each node, for 109 focal mechanisms determined in this	

study. Gridding parameters are: 0.1x0.1 degree spacing and constant number of events at each node is 5.....	59
Figure 44. Ternary diagram of all focal mechanisms located in the study area.....	60
Figure 45. Stress inversion (a) and histogram of Φ values versus frequency (b) results of all focal mechanisms located in the study area, by Micheal' s method.	61
Figure 46. (a) Locations of all focal mechanisms located in the study (Red and blue circles are locations of focal mechanisms calculated in this study and taken from available catalogs, respectively) area and (b) resulting earthquake resolution over a 0.1x0.1 degree grid spacing.	62
Figure 47. Orientation of the trend of σ_1 (bars) showing, (a) faulting types (b) variance of the stress tensor at each node, for all focal mechanisms located in the study area. Gridding parameters are: 0.1x0.1 degree spacing and constant number of events at each node is 3.....	63
Figure 48. Orientation of the trend of σ_1 (bars) showing, (a) faulting types (b) variance of the stress tensor at each node, for all focal mechanisms located in the study area. Gridding parameters are: 0.1x0.1 degree spacing and constant number of events at each node is 5.....	64
Figure 49. Close-up view showing (a) geology (MTA,2003) (b) focal mechanisms of the zoom-in area. Focal mechanism and locations shown in red color displays the Çorum cluster.....	66
Figure 50. . Distribution of all P- T- axes orientations of (a) zoom-in and (b) Çorum cluster, shown in stereographic projection. Black diamonds show T- axes and white diamonds show P- axes.....	67
Figure 51. Stress inversion (a) and histogram of Φ values versus frequency (b) results of focal mechanisms located in the zoom-in area, by Micheal' s method.	67
Figure 52. Stress inversion (a) and histogram of Φ values versus frequency (b) results of focal mechanisms located in the Çorum cluster, by Micheal' s method.	68
Figure 53. Focal mechanism data represented as SH_{max} axes. A color-coded central circle indicates the tectonic regime. Inset figures show the rose diagrams of Sh_{max} and Sh_{min} orientations.	70

Figure 54. Simplified map of our results, subdivided into 6 groups. Stereonets refer to the stress orientations of related group. Blue arrows indicate the movement directions obtained from this study (size of the arrows are not to scale). Inset figure gives the general Riedel shear pattern of the region.....71

CHAPTER 1

INTRODUCTION

1.1 Purpose and Scope

The North Anatolian Fault (NAF) is one of the world's largest active continental strike-slip faults, and forms the northern margin of the Anatolian plate. NAF generated series of disastrous earthquakes, including 1999 Kocaeli earthquake ($M = 7.4$) and is certain to have more damaging earthquakes in the future. Although NAF's geologic and geomorphologic features are well defined, crustal deformation and associated seismicity around central segment of the NAF is relatively less-known. This region has an important role in detecting the earthquake risk in Ankara and its surroundings.

Purpose of this study is to analyze the seismic activity and stress regime of the central segment of the NAF between latitudes of 39°N and 42°N and longitudes of 32°E and 38°E (Figure 1). For this purpose, earthquakes which are recorded by 39 broadband seismic stations deployed during the North Anatolian Passive Seismic Experiment (2005-2008), will be relocated and their focal mechanisms will be determined. Along with the focal mechanism determination, stress regime of the region will be analyzed and interpreted with other available geological and geophysical data. The results will lead us to a better characterization of the fault zone and thus have a broad benefit to society because of high earthquake hazard risk of the region that includes 12 cities some with large populations (Ankara, Çankırı, Karabük, Kastamonu, Çorum, Yozgat, Sinop, Samsun, Amasya, Tokat, Sivas).

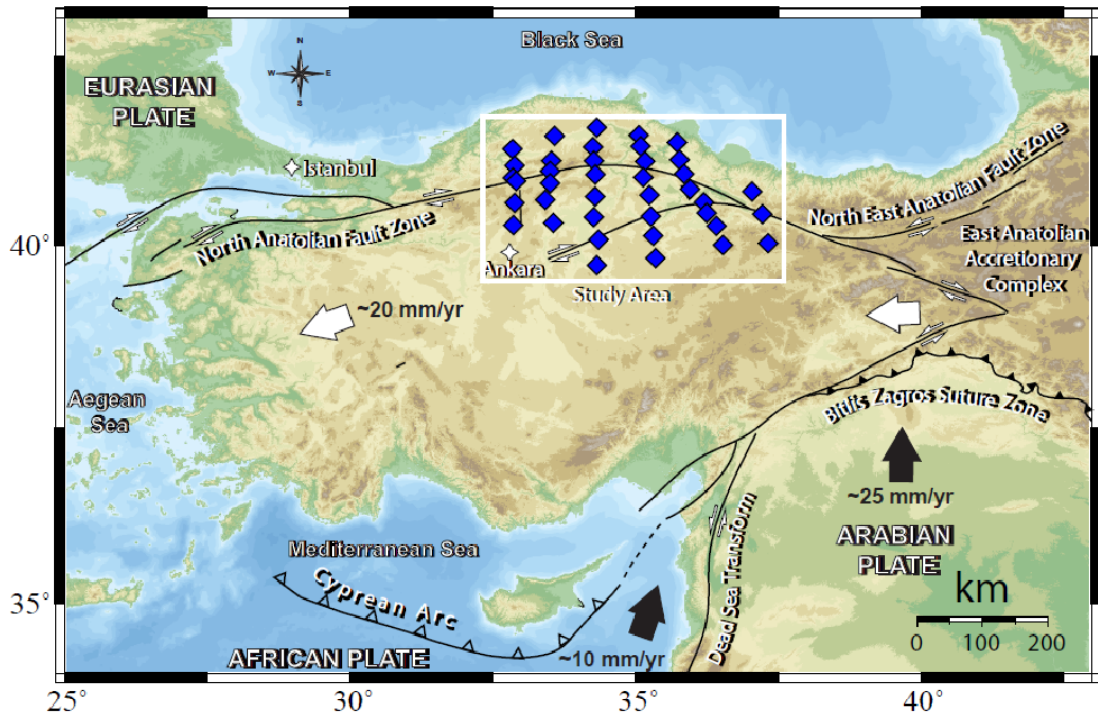


Figure 1. Simplified tectonic map of Turkey (modified from Bozkurt, 2001). The box indicates the location of the study area and blue diamonds represents broadband seismic stations of North Anatolian Passive Seismic Experiment.

1.2 Data and Methods of the Study

Earthquake data used in this study is gathered from North Anatolian Passive Seismic Experiment (2005-2008), which are recorded by 39 broadband seismic stations (Figure 1). Over 200 earthquakes having magnitudes greater than 3 are selected from monthly catalog of NEIC-USGS. At first, phase picking of P- and S-waves is achieved using the Seismic Analysis Code - SAC (Goldstein et al., 2003). Later, events having better records are input to a conventional least-squares inversion algorithm HYPOCENTER for the relocation process (Lienert, 1994). During the relocation, 1-D velocity model of the region is determined by using the program VELEST that implements a simultaneous

inversion for hypocenters and velocity model (Kissling, 1995). After defining the crustal velocity model and hypocenter locations, focal mechanism determination is performed using FOCMEC program (Snoke, 2003) which allows grid search to find all possible double couple solutions based on first motion polarities and amplitude information. Next, reliable *P*- and *T*- axes orientations of well-constrained events are calculated from possible solutions and best solutions are then used for stress tensor inversion using codes by Michael (1984) and Gephart and Forsyth's (1984) in the ZMAP software package (Wiemer, 2001).

1.3 Organization of the Thesis

This thesis constitutes 5 chapters. Chapter 2 gives an overview of tectonic setting of the area, which summarizes the geology of the study area. Afterwards, information about the NAF and recent seismicity of the region is discussed in detail. Chapter 3 deals with earthquake relocation and velocity model determination. In this chapter, information about related software, how these programs are used and inversion results are presented. Chapter 4 is related to the focal mechanism theory, its application in this study and related results. This chapter also includes the stress tensor inversion applications and results gathered in this study. In chapter 5, all the results presented in the thesis are interpreted and discussed in detail.

CHAPTER 2

TECTONIC SETTING

2.1 Geology of the Region

Central segment of the NAF is situated in between three different tectonic units: İstanbul Zone in the northwestern part, Sakarya Zone in the north and Kırşehir Massif in the south. These zones are separated from each other by two major sutures (Figure 2): İzmir-Ankara-Erzincan and Intra-Pontide sutures.

The İstanbul Zone is located in the southwestern margin of the Black Sea and characterized by Neoproterozoic crystalline basement overlain by a well-developed, continuous Paleozoic sedimentary succession of Ordovician to the Carboniferous (Okay et al., 2006). These Paleozoic rocks are unconformably overlain by Triassic continental clastic rocks with basaltic flows (Okay et al., 2006).

The Sakarya Zone is an east-west-trending continental fragment, which is about 1500 km long and 120 km wide (Okay and Tüysüz, 1999). The basement of Sakarya Zone is characterized by subduction–accretion units, called the Karakaya Complex, in its western parts (Okay and Tüysüz, 1999). The Karakaya Complex is described by Okay and Göncüoğlu (2004) as: highly-deformed and partly metamorphosed clastic and volcanic series of Permian and Triassic age. This basement is overlain by Jurassic to Tertiary clastic and carbonate cover rocks (Bozkurt and Mitwede, 2001).

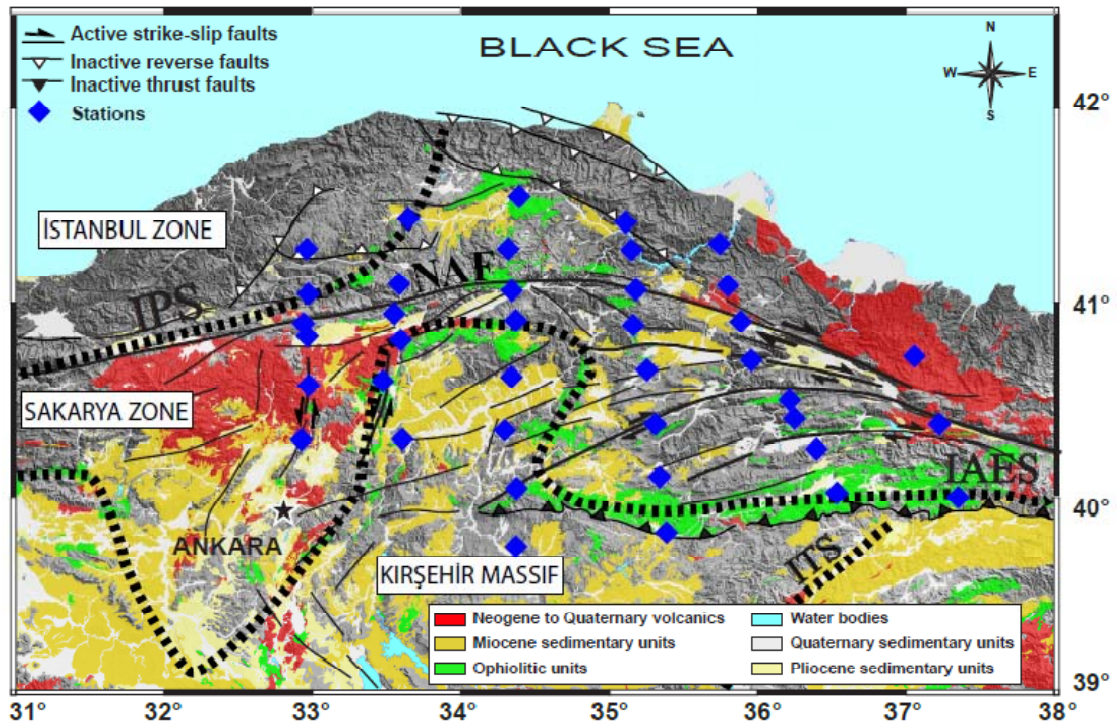


Figure 2. Simplified geological map of the study area (M.T.A. 1:500000) geological map of Turkey; sutures and faults are compiled from Bozkurt 2001 and Rojay, B., Kaymakçı, N., personal communication, 2010). IAES= İzmir-Ankara-Erzincan Suture, IPS= Inner Pontide Suture, ITS = Inner Tauride Suture.

The Kırşehir Massif is bordered by İzmir-Ankara-Erzincan Suture Zone in the north (Figure 2) and it has three main assemblages: magmatic (CAG: Central Anatolian Granitoids), metamorphic (CAM: Central Anatolian Metamorphics) and ophiolitic rock (CAO: Central Anatolian Ophiolites) and they are altogether termed as Central Anatolian Crystalline Complex (CAAC) (Göncüoğlu et al., 1994; Yılmaz and Özel, 2008). The CAM consists of the Paleozoic–Mesozoic aged medium to high-grade metamorphic rocks, which are overthrust by Upper Cretaceous partially preserved ophiolites, with a number of voluminous granitoids and associated volcanics. (Göncüoğlu and Türel, 1994; Bozkurt and Mittwede, 2001).

Between the Sakarya Zone to north and Kırşehir Massif in the south, Çankırı Basin is located. It is mostly consisted of Upper Cretaceous volcano-sedimentary rock assemblages and has a Ω -shape due the northward bending of IAES near the basin (Kaymakcı, 2000; Kaymakcı et al., 2009).

The 2000-km-long İzmir-Ankara-Erzincan suture represents the main geological boundary between Laurasia and Gondwana, during the late Paleozoic and Early Tertiary (Okay and Tüysüz, 1999), which separates the Sakarya Zone in the north from the Kırşehir Massif and the Anatolide-Tauride block in the south (Figure 2). The suture zone is composed of ophiolitic rocks associated with accretionary mélangé units, which lacks a complete ophiolitic sequence (Moix et al., 2008). Suture follows an approximately E-W trend but it makes a northward bend in the Çankırı Basin, to the east of Ankara (Kaymakcı, 2000). This geometry can be followed by ophiolite occurrences and shows the indentation of Kırşehir Block, most likely controlled by paleotectonic tear zones. In the western boundary, paleotectonic tear zone overlaps with an active N-S-trending left-lateral strike-slip fault zone and in the east cut by active NE-SW-(ENE-WSW)-trending splays of the NAF.

The Intra-Pontide suture (Şengör and Yılmaz, 1981), defines the former plate boundary between the Sakarya and the İstanbul zones (Figure 2). Closure age of the suture is still in debate, views are: Late Cretaceous (Yılmaz et al., 1995; Robertson and Ustaömer, 2004), the Paleocene–Eocene (Şengör and Yılmaz, 1981), the Early Eocene (Okay et al., 1994; Wong et al., 1995), or Early Eocene to Oligocene (Görür and Okay, 1996). The suture is a tectonic mixture of units derived from İstanbul and Sakarya Zones, with various metamorphic rocks and dismembered metaophiolitic bodies (Moix et al., 2008).

Along the NAF, volcanic activity is associated with the volcanism along the Galatia, Niksar and Erzincan areas (from west to east). In the study region, NAFZ overlaps in part with volcanism of the Galatian province (Figure 2) and in the east, middle to upper Miocene volcanics is seen with younger Niksar volcanics. The Galatean Volcanic

province (GVP) is the largest Neogene/Quaternary volcanic belt along the NAF (Adiyaman et al., 2001). In the GVP, Paleozoic metamorphics and Mesozoic to Paleogene sedimentary rocks are overlain by Miocene to Pliocene volcanic, volcanoclastic, and continental sedimentary rocks (Çinku and Orbay, 2008 and references therein). In the east, middle to upper Miocene volcanics are widely exposed north of NAF whereas Nixsar pull-apart basin has younger Plio-Quaternary volcanics along the master strand of NAF (Tatar et al., 2007).

2.2 North Anatolian Fault Zone

The 1500-km-long North Anatolian Fault Zone (NAFZ) is one of the world's best-known strike-slip faults, which forms the northern margin of the Anatolian block and extends from eastern Turkey to Greece in the west (Figure 1). The NAFZ is a broad arc-shaped dextral strike-slip fault system and joins with sinistral East Anatolian Fault Zone (EAFZ) forming a typical triple junction at Karlıova (Bozkurt, 2001). The generation of NAFZ, together with EAFZ (East Anatolian Fault Zone), caused the westward movement of Anatolian plate, allowing the Arabian plate to move northward faster than the African Plate (Reilinger et al., 1997; Oral et al., 1995; DeMets et al., 1990; Barka and Reilinger, 1997).

NAFZ has a typical strike-slip fault zone morphology, which is characterized by a narrow zone, offset, captured and dammed streams, sag ponds and other deformed morphological features (Şengör, 1979). At the surface NAFZ has a large arc-shaped trace with sub parallel splays consistent with a fishbone structure and a surface width from several 100 m to 40 km. This fault zone consists of several second order faults that splay from it into the Anatolian Plate (Bozkurt, 2001)

Age of the NAF is controversial, along the reviews Şengör et al. (2005), suggest that the NAF is active since Late Miocene. Barka and Kadinsky-Cade (1988), gives forming time of NAFZ as earliest Pliocene. The slip rate of NAFZ, estimated from the GPS data from previous studies, is approximately 20-24 mm/yr (McClusky et al., 2000, Yavaşoğlu et al., 2006).

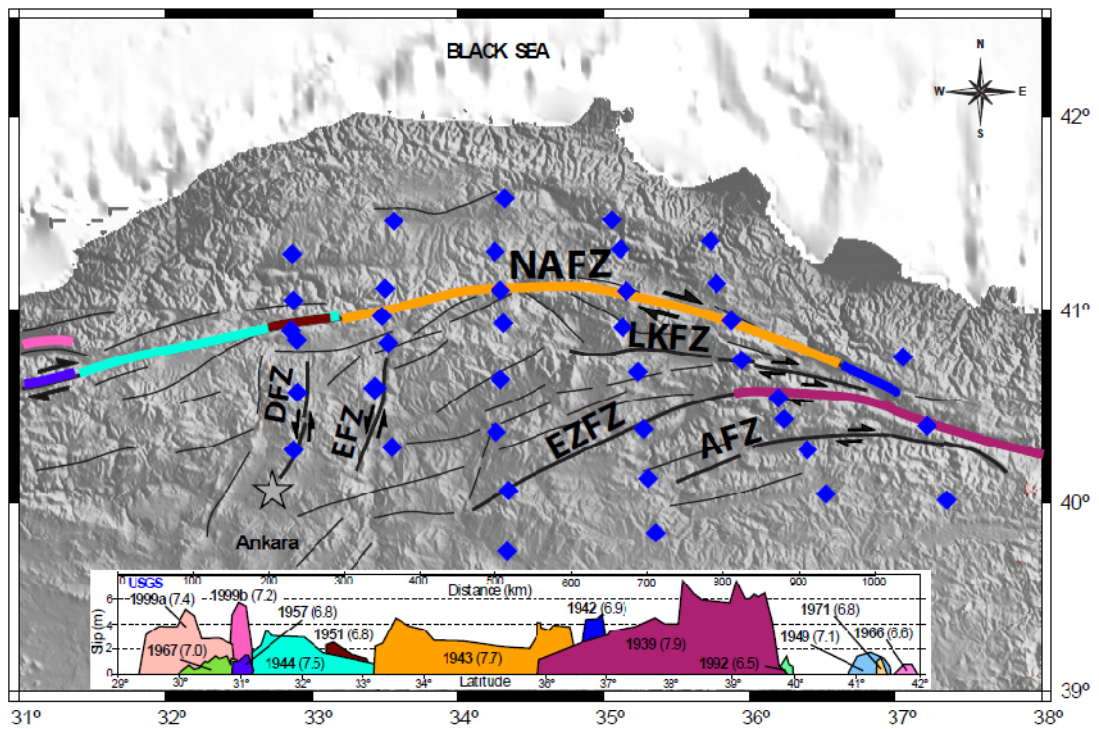


Figure 3. Topographic map showing surface ruptures along the central segment of NAF with seismic station locations. Ruptured segments of the NAF during major earthquakes of the last century are color coded and related fault displacements taken from USGS are shown in the inset figure. NAFZ= North Anatolian Fault Zone, LKFZ= Laçin-Kızılırmak Fault Zone, EZFZ= Ezinepazarı Fault Zone AFZ= Almus Fault Zone, DFZ= Dodurga Fault Zone, EFZ= Eldivan Fault Zone.

In the review paper of Şengör et al. (2005), it is suggested that NAF has shown a cyclical seismic behavior, which are century long cycles representing NAF's east and westward migrations. Lack of clear seismic recording before the twentieth century prevented the interpretation of this cyclical seismic behavior, but records show that NAF had a lively seismicity during that time period (Şengör et al., 2005). Major historical earthquakes occurred along the NAF during the twentieth century, with magnitudes greater than 7. These earthquakes, started in 1939 (M= 7.9), ruptured most of the NAF (Figure 3). The 1939 Erzincan earthquake ruptured the crust over 360 km and with a maximum right-lateral offset of 7.5 m (Provst et al., 2003). This earthquake is followed by serious disastrous earthquakes, in Niksar-Erbaa in 1942 (M= 6.9), in Ladik in 1943 (M= 7.7), and in Bolu, Gerede, Çerkeş in 1944 (M= 7.5; see Figure 3) (Şengör et al., 2005). Along the Mudurnu valley, two large earthquakes (in 1957 M= 6.8; in 1967 M= 7.0), ruptured the southern stand of NAF. More recently, highly damaging earthquakes occurred in 17 August (İzmit; M= 7.4) and 12 November 1999 (Düzce; M= 7.2). The İzmit earthquake produced more than 150 km surface rupture, with a focal mechanism solution (Dziewonski et al., 1987) consistent with the right-lateral movement along NAF. It is expected that, with an approximately %50 probability, these two earthquakes will be followed by a major, $M \leq 7.6$ event within the Marmara segment of the fault, in the next half century (Şengör et al., 2005).

The study area includes the segments that ruptured in 1944, 1943, 1942 and a part of the 1939 zone. In particular, the overlap zone between the two largest events (1939 and 1943) is within the study area and is characterized at the surface by complex splay structures (Koçyiğit, 1989; Bozkurt and Koçyiğit, 1996). Şengör et al. (2005) concludes that NAF is part of the North Anatolian Shear Zone (NASZ), which is a dextral shear zone and its weak structure, is evidenced by seismic activity. The NAF branches into different offshoots (splines) within NASZ, that extends into the interior parts of Anatolia (İşseven and Tüysüz, 2005). In the central part of NAF, there are southward splitting branches and these generally have right-lateral slip (Yavaşoğlu et al., 2006).

2.2.1 Major Splays

Central segment of NAF is controlled mainly by southward splitting splay faults, which can be compared with Riedel fractures (Figure 3). These faults from SE to NW are: (1) Almus Fault Zone (AF); (2) Ezinepazarı Fault Zone (EZFZ); (3) Laçın-Kızılırmak Fault Zone (LKF). These splays have generally right-lateral slip, creating east-west-trending wedge like blocks which rotate the Anatolian Block in a counter-clockwise sense (Taymaz et al., 2007).

The Almus Fault Zone is approximately 150 km long, active dextral strike-slip fault system which extends from Reşadiye in the east to Iğdır town, southeast of Zile, in the west (Tatar, 1995 and references therein). The fault zone has well-developed surface expression, with a width ranging from a few hundred meters along its eastern course to 12 km at its western end, where an active strike-slip depression, the Kazova basin, is located (Bozkurt and Koçyiğit, 1995).

The Ezinepazarı–Sungurlu Fault Zone is about 350 km long and extends from the Erzincan Basin to Sungurlu in the west, bounding the southern margin of the Niksar basin, where it changes the direction from NW-SE to E-W (Tatar, 1995). This fault is first recognized by Ketin (1957), after the greater Erzincan earthquake in 1939 (Tatar, 1995). Furthermore, earthquake activity continued with the 10 June 1985, 14 February 1992 and 14 August 1996 earthquakes (Taymaz et al., 2007). EZFZ leaves the main branch east of Reşadiye and ends within the inner bend of the Delice tributary of the Kızılırmak (Şengör et al., 2005). In addition, Kaymakçı et al. (2003) states that EZFZ is oriented WSW–ENE and have dextral strike-slip character.

Other important splay is Laçın-Kızılırmak Fault Zone, which are located in the area between the EZFZ and the main branch of the NAF (İşseven and Tüysüz, 2005). This fault zone is very important due to their earthquake activity (İşseven and Tüysüz, 2005),

as it is responsive for the destructive earthquakes occurred during the 1940s (Eyidogan et al., 1991).

Apart from splays, central part of NAF consists of N-S-trending faults and they play an important role in the neotectonic framework of the region. Two important fault zones are Dodurga Fault Zone (DFZ) (Koçyiğit et al., 2001) and Eldivan Fault Zone (EFZ) (Kaymakçı, 2000). DFZ is defined by Koçyiğit et al. (2001) as N-S-trending, 4 to 7-km-wide and 36-km-long, sinistral strike-slip fault zone. EFZ displays sinistral strike-slip motion, with a reverse component, and defines the western margin of Çankırı Basin (Kaymakçı, 2000)

In a Riedel geometric pattern, splays EZFZ and LKFZ, develop as y-shears whereas approximately N-S-trending fault zone EFZ is nearly parallel to the orientation, along the Çankırı Basin (Kaymakçı et al., 2009).

2.3 Seismicity of the Region

For the seismicity analysis, two different catalogs taken from Boğaziçi University, Kandilli Observatory and Earthquake Research Institute (KOERI), are used to have a complete data set. First catalog consists of earthquakes with magnitude greater than 3, which are recorded during 1990-2004 (Figure 4). Second catalog includes all detected earthquakes occurred between 2004 and 2009 (Figure 5).

First catalog has 1076 data (Figure 4), in which depths are mainly limited to first 10 km depth. This catalog reveals two main clusters in the west and in the middle of the region. Western cluster is related to the Orta Earthquake occurred on 6 June 2000 (M= 6). This major earthquake, together with its fore- and aftershocks, formed a highly concentrated N-S-trending seismicity parallel to the DFZ. Based on the available geological and

seismological data, Orta earthquake originated from the activation of Dodurga fault, which is the master strand of the DFZ (Koçyiğit et al., 2001). In the central part, another cluster is observed, along the right-lateral splay LKF. Two major earthquakes of these clusters are 14 August 1996 (M = 5.6) and 8 March 1997 (M = 6.0), occurred in Mecitözü region.

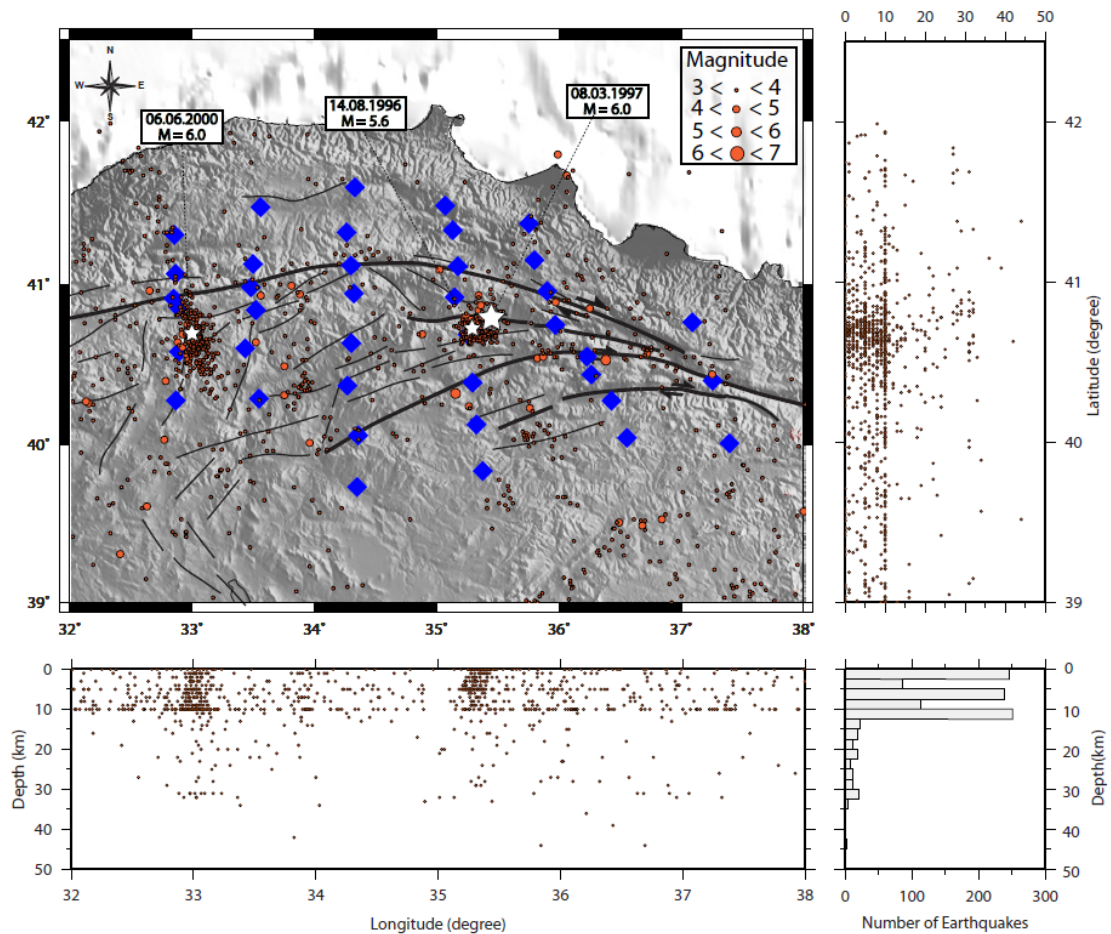


Figure 4. Distribution of local seismicity within the study area that took place during 1990-2004, with magnitude ≥ 3 (KOERI). The earthquakes are scaled to their magnitudes. White stars indicates major earthquakes of the past century. Diamonds denote seismic stations and major faults are shown by black line.

Second catalog has larger data set consisting of 4106 events (Figure 5), with depth values mostly within the first 15 km depth and points out 4 main clusters. In the western part, active seismicity related to DFZ still continues, whereas in the southwestern part two new clusters are recognized. The NE-SW-trending cluster consists of earthquakes that vary mostly between 2.0-3.0 magnitude. Southern cluster has two major earthquakes, 30 June 2005 (M= 5.6) and 20 December 2007 (M= 5.7), occurred near Bala town of Ankara. According to the recent findings of Tan et al. (2009), these two earthquakes occurred as a result of increasing stress after the 1999 earthquakes. Last cluster is observed in the middle of the region, where seismicity migrated from Mecitözü towards to west at the center of the study area near Çorum. Two major earthquakes of this cluster are shown in Figure 5. The seismicity in this region will be discussed in detail later in Chapter 4, together with the new results of this study

In order to analyze the earthquake distribution and statistics of the region, two catalogs are combined by using ZMAP (Wiemer, 2001) software which resulted in a total of 5182 earthquakes.

According to the results of the data set gathered by combining these two catalogs, this region has experienced 5 distinct periods of increased seismicity (Figure 6). First abrupt cumulative moment increase is observed with Mecitözü earthquakes in 1996 and 1997. These earthquakes have high moment releases due to their large magnitudes. They are followed by Orta Earthquake, in 2000 with magnitude of 6. Final significant moment releases occurred due to the 2005 and 2007 Bala earthquakes recently.

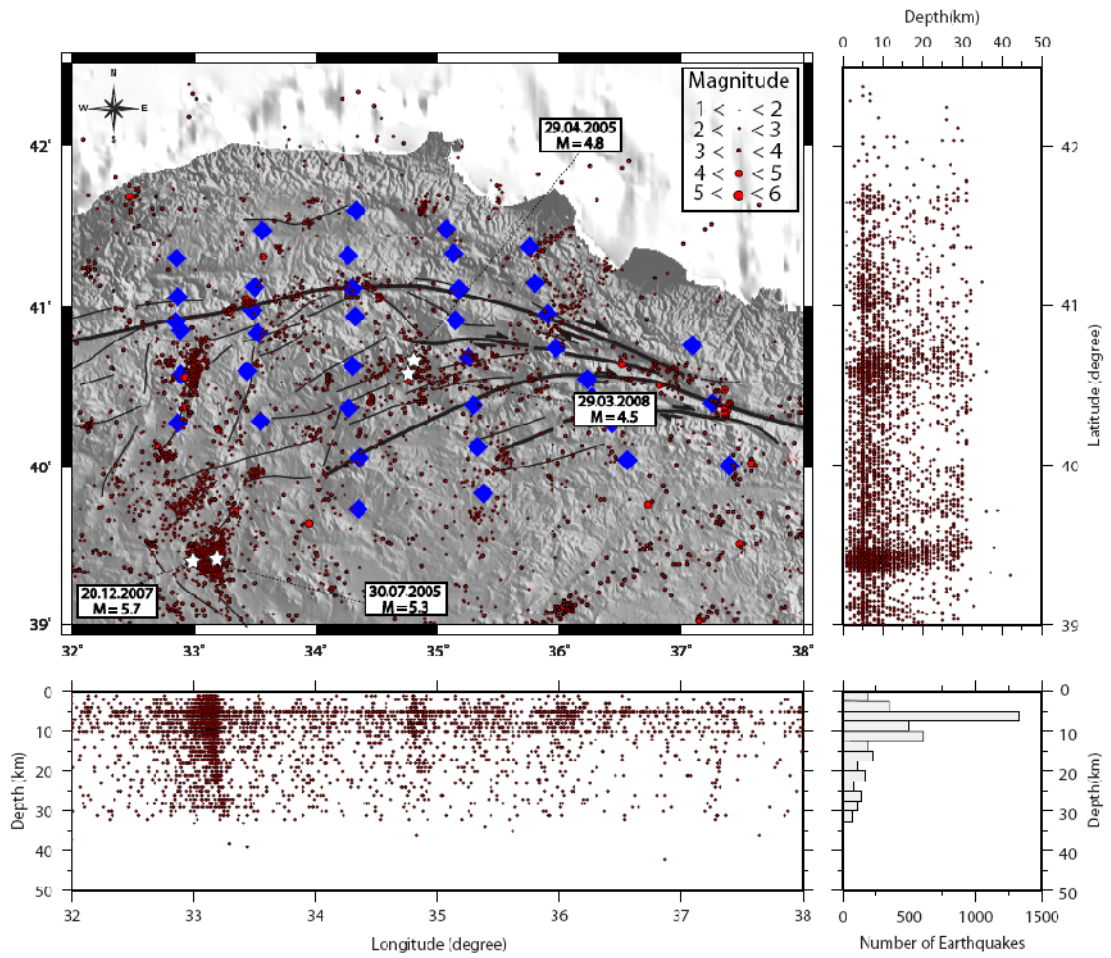


Figure 5. Distribution of local seismicity within the study area that took place during 2004-2009, with magnitude ≥ 1 (KOERI). The earthquakes are scaled to their magnitudes. White stars indicates major earthquakes of the past century.

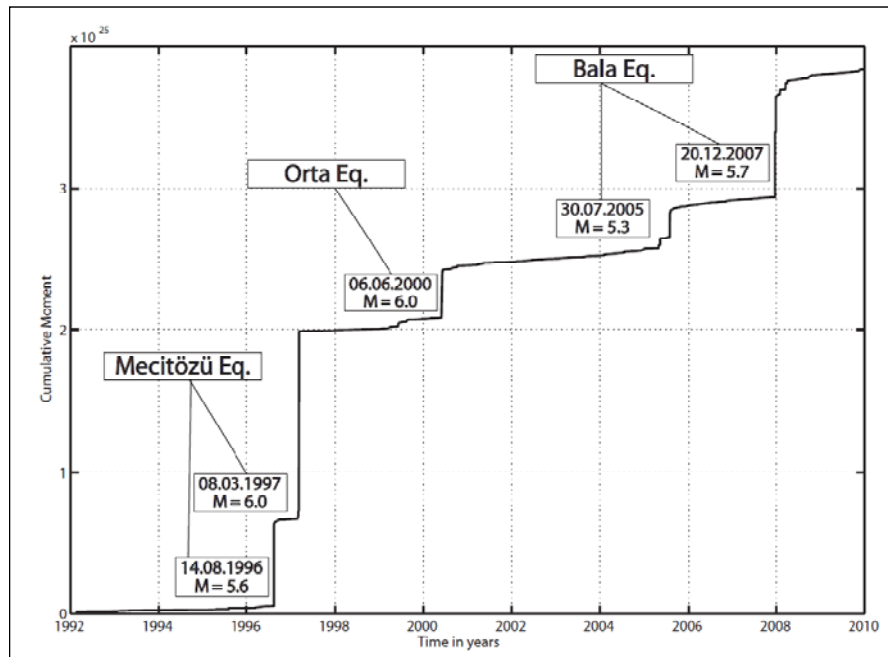


Figure 6. Cumulative moment release of the combined catalog, plotted as a function of time.

Figure 7 shows the plot of earthquake magnitudes as a function of time for the entire data set. Except for the distinct major events, magnitudes generally vary between 3 and 4, where the abrupt increase in 2004 is related to the second catalog records. Time histogram (Figure 8) points out the same major events, where number of earthquakes increased significantly. Number of events increase constantly with time, due to the increasing seismic recordings.

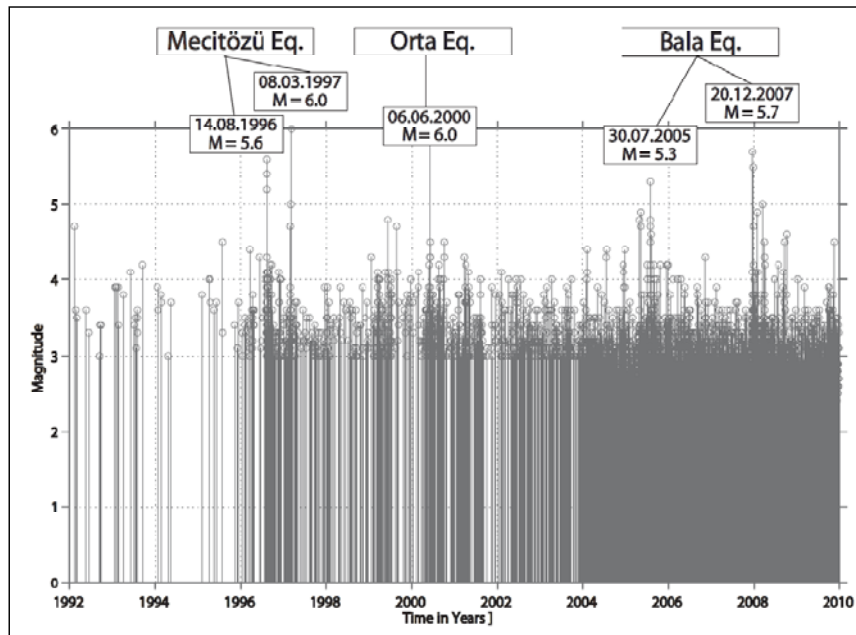


Figure 7. Temporal distribution of the earthquakes, plotted as a function of magnitude.

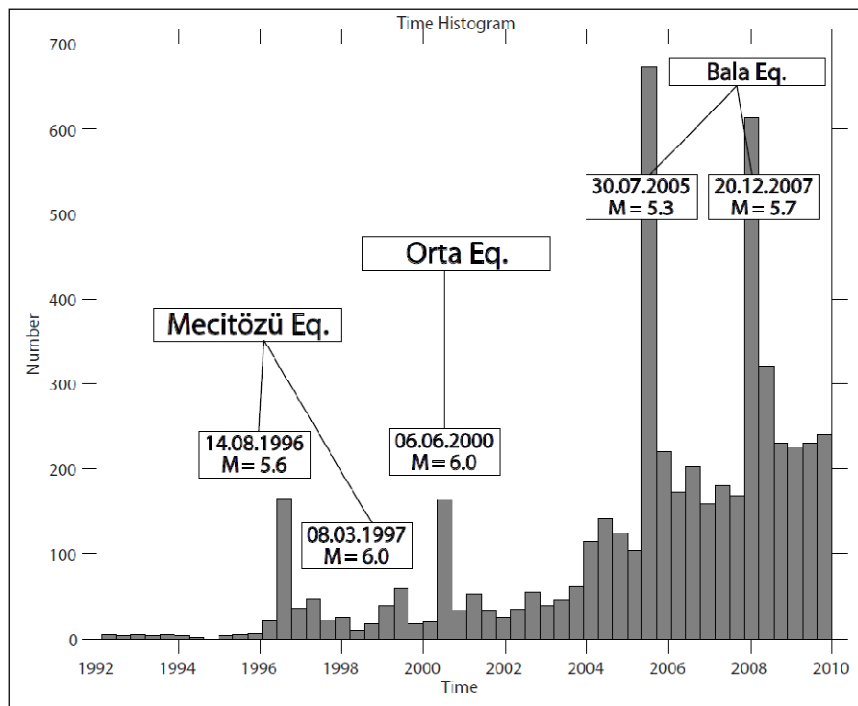


Figure 8. Time histogram of the combined catalog.

In addition to time series analysis, quarry contamination of the area is calculated (Figure 9). Quarry contamination can be measured by mapping the ratio of daytime to nighttime number of events. In general, remarkably high ratios are sign of exploration activities. For the quarry detection in the study area, 0.1x0.1 degree grid size, with 100 constant number of events are used. ZMAP program plots the histogram of the event distribution and automatically marks the bins that contain the top 40% rates per hour. The resulting map (Figure 9) displays the ratio of high day/time to nighttime. High ratios ($\sim R > 5$, gray) indicate possible quarry contamination. There is a significant ratio increase in the SW cluster, which can be related to mine contamination or mine induced earthquakes. Another noticeable increase is present in the southern part, represented with black color. Lack of seismic data in this part of the region can be the reason of high ratios.

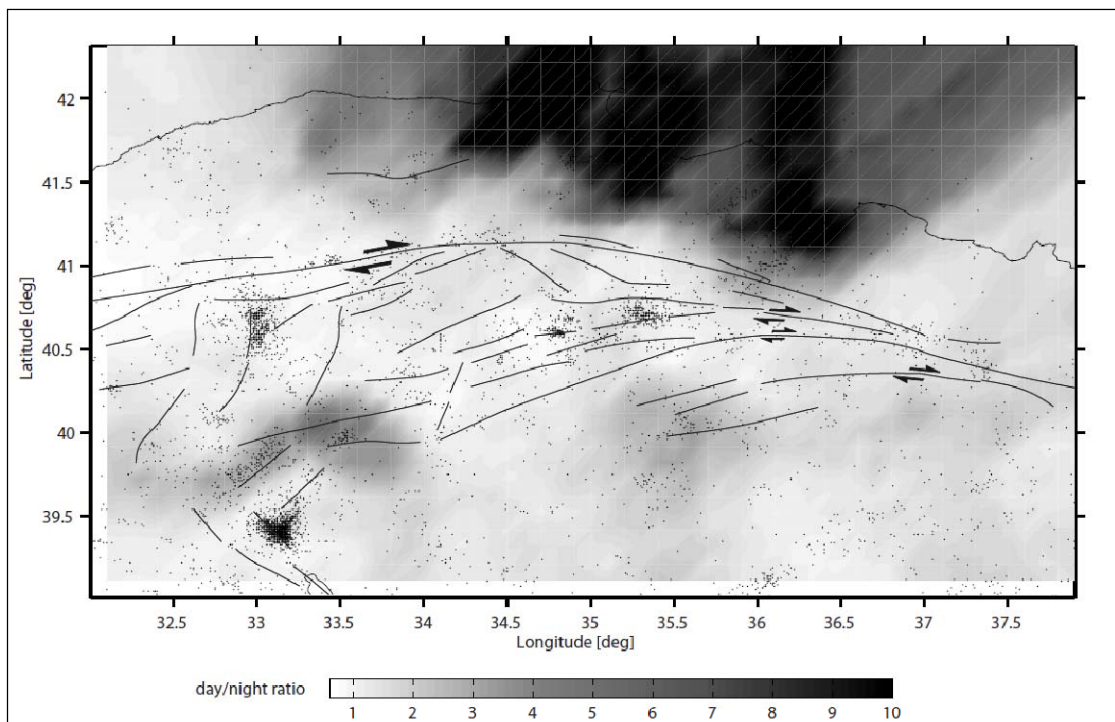


Figure 9. Quarry blast mapping of the earthquakes.

2.3.1 Earthquake Statistics

Statistical analysis of earthquakes is an important tool for seismologist to understand the seismic activity, and to predict future seismicity. Until now, many statistical models have been tried to describe source processes and make probabilistic forecast.

Gutenberg–Richter (1944) distribution (also called as Frequency-Magnitude distribution (FMD)) is the basic law that describes the size distribution of earthquakes:

$$\log_{10} N = a - bM \quad (1)$$

where N is the expected cumulative number of earthquakes, M is the magnitude, a and b are constants (Stein and Wysession, 2003). This distribution is described by a linear relation, where a -value is the intercept and it defines the seismic productivity. The b -value is equal to the slope of the equation and it describes the relative size distribution of earthquakes. Its value is generally close to 1 in the Earth's crust (Sanchez et al. 2004 and references therein). Many examples show that b -value is near unity for most seismically active regions on Earth (Bayrak et al., 2008) High b -values can be related to low stress, high heterogeneity and high thermal gradient. If b -values are higher, relatively larger proportions of earthquakes are expected and vice versa. Deviations of b -values may arise from the incomplete earthquake catalog for small earthquakes. Also deviation for large earthquakes is expected, because of the surface wave saturation. The magnitude of completeness, M_c , is defined as the magnitude above which 100% of all earthquakes can be detected (Stein and Wysession, 2003)

For the entire region, FMD is calculated using maximum likelihood method (Figure 10). The b -value is calculated as 1.33, which can be due to the incompleteness of data sets and short time span of the second catalog. In the FMD plot, data deviates from the trend-line around magnitude 4.5. Another FMD graph, which is picked manually,

displays a trend-line that fits well to magnitudes greater than 4.5 (Figure 11). According to this graph, b is equal to 1.11, which increases the expected cumulative number of earthquakes (N).

Magnitude of completeness of the region is determined as 3 (Figure 10) from the FMD plot, which is not surprising since the first catalog records the earthquakes with magnitudes greater than 3.

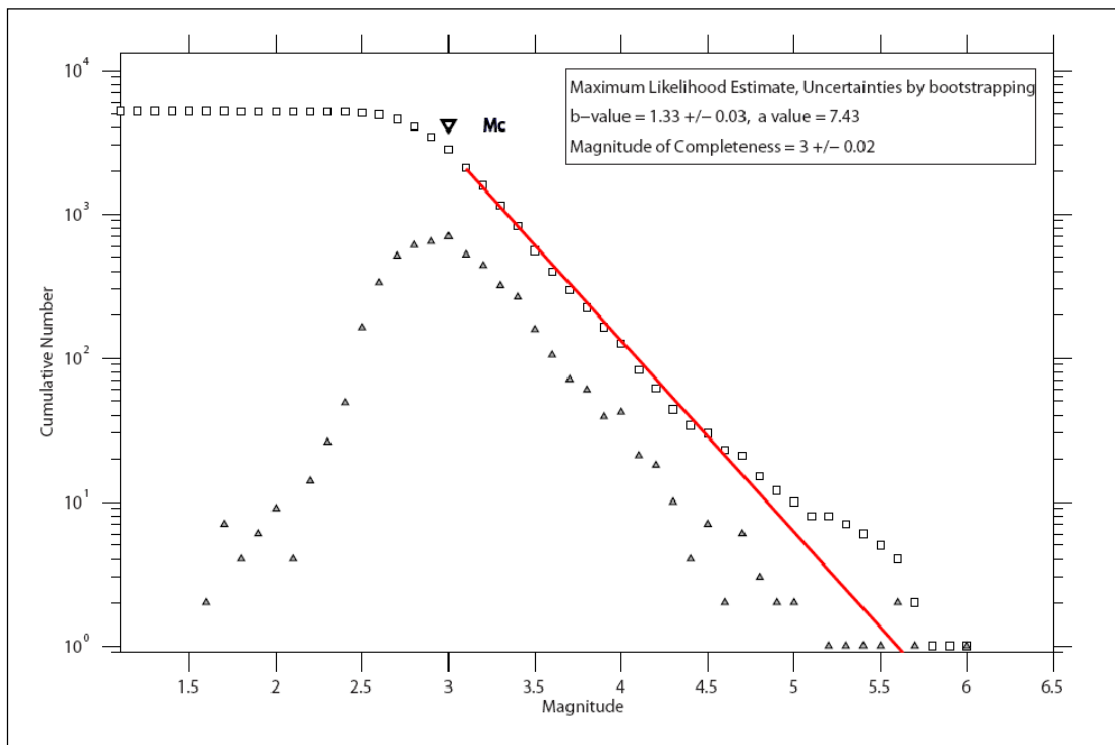


Figure 10. Frequency-magnitude distribution of the combined catalog. Both the cumulative (squares) and non-cumulative (triangles) plots are shown.

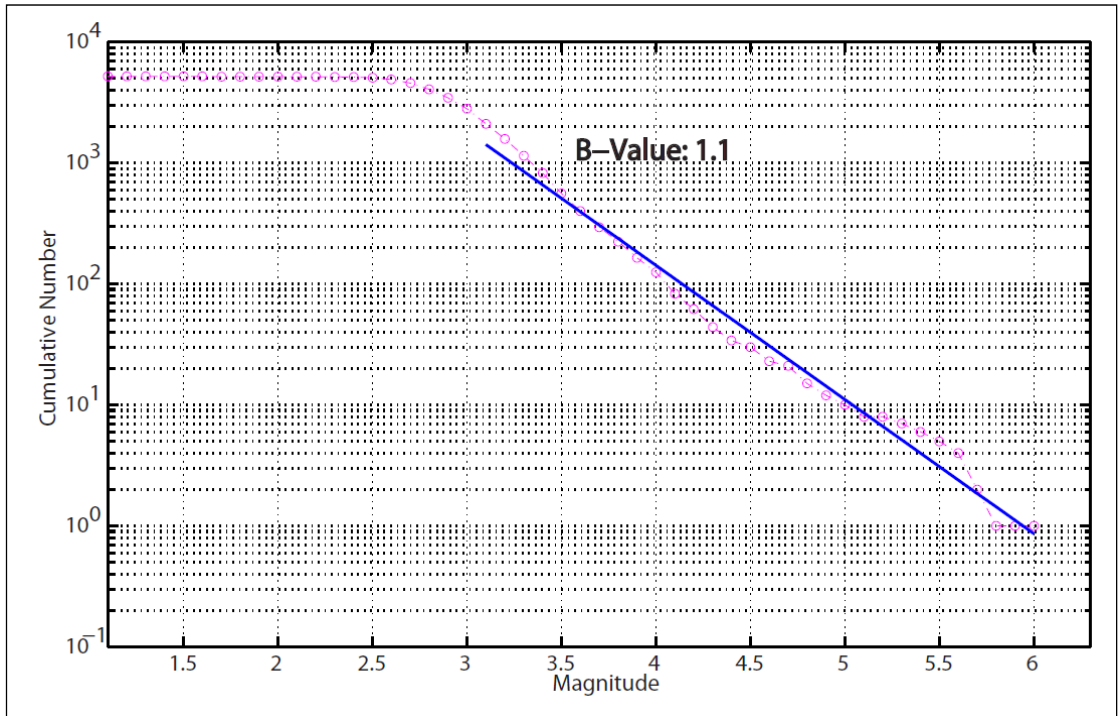


Figure 11. Manually picked frequency-magnitude distribution of the combined catalog. Circles represent cumulative plot.

2.3.2 Focal Mechanisms

Fault plane solutions of the 36 earthquakes that are located in the study area are gathered from Harvard CMT (Dziewonski et al., 1987), European Mediterranean Seismological Centre (EMSC) (Godey et al., 2009) and European-Mediterranean Regional Centroid Moment Tensor Catalog (RCMT) (Pondrelli et al., 2002, 2004, 2007) (Table A.1). These earthquakes are recorded in the time period between 1939-2008. Distribution of types of mechanisms can be seen in rake based ternary diagram (Figure 12). Most of the solutions show right-lateral strike-slip motion, which is consistent with the NAFs and its splays movement. The largest magnitude is recorded in 1942, in the Niksar-Erbaa area ($M=7.2$).

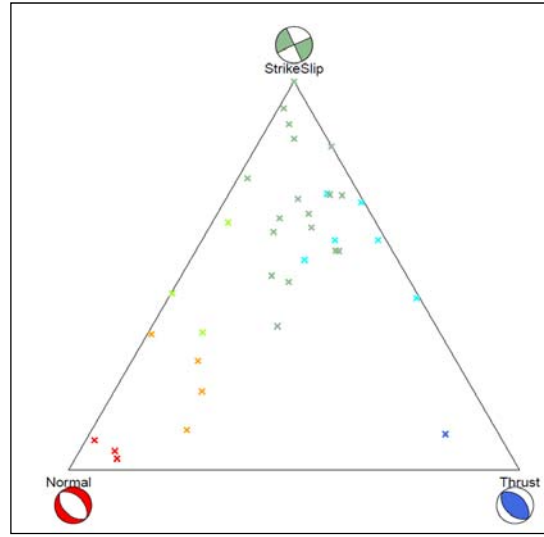


Figure 12. Rake-based ternary diagram of 36 earthquakes that occurred in the study area between 1939 and 2010.

These solutions are mainly located on the southern block of NAF, indicating that this region is seismically more active (Figure 13). Main localization (Eq. No: 16, 17, 18, 19) is observed in the western part of the region, due to the Orta earthquake (June 6, 2000; $M=6$ (Koçyiğit et al., 2001)) and its several aftershocks. Another cluster is observed in the southeast, near Bala town of Ankara (Eq. No: 15, 25, 26, 27, 28, 29, 31, 31, 33, 35), which are related to the two earthquakes sequences of maximum magnitude of 5.6 occurred in 2005 and 2007. From middle to the eastern part, E-W-trending splays generated mostly the right-lateral focal mechanisms (Eq. No: 2, 11, 12, 13, 22). According to the orientations of P - and T -axes plotted on lower hemisphere projection (Figure 14, Table A. 2), the region experiences NW-SE compression, and NE-SW tension.

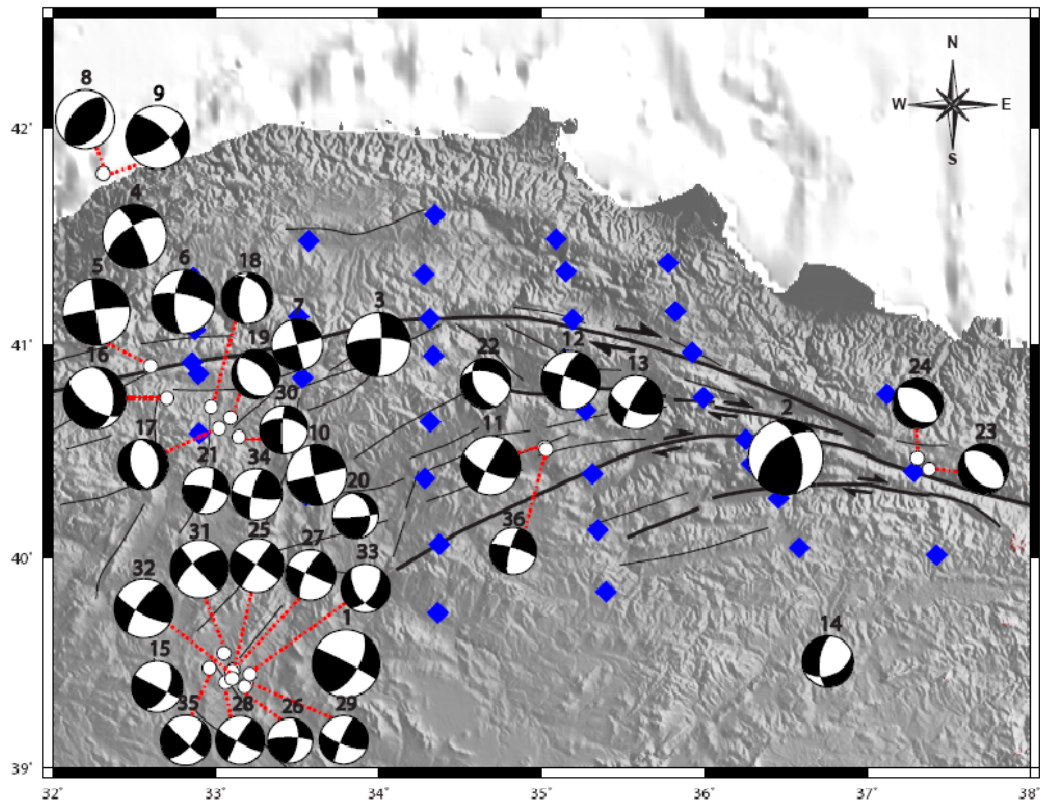


Figure 13. Fault plane solutions of 36 earthquakes that occurred in the study area between 1939 and 2010, with $M \geq 4.3$. The focal mechanisms are scaled to their magnitudes. For the sources and parameters of the solutions, see Appendices 1 and 2.

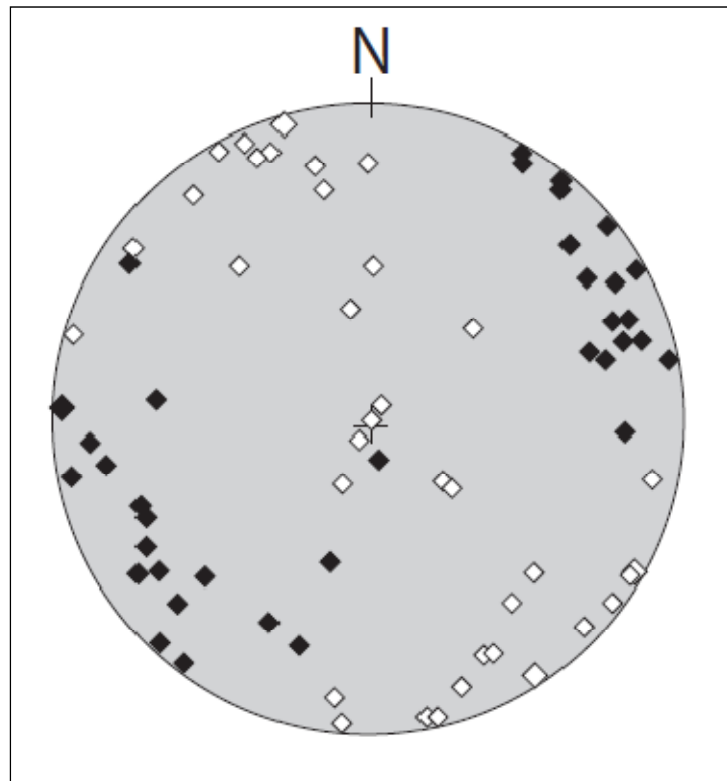


Figure 14. Distribution of all P - and T -axes orientations of 36 earthquakes that occurred in the study area between 1939 and 2010. Black diamonds show T -axes and white diamonds show P -axes.

CHAPTER 3

EARTHQUAKE RELOCATION

3.1 Data Processing

In this study, earthquakes recorded by 39 three-component broadband stations (Table A. 3) deployed by North Anatolian Passive Seismic Experiment, during 2005-2008 are analyzed. Available data set includes 190 earthquakes with magnitude ≥ 3 . Initial hypocenter and depth locations of these earthquakes are taken from monthly catalog of NEIC-USGS.

For the phase picking process, earthquake data is rotated to great circle components: N- and E-components rotated to radial and transverse, respectively. These rotated components together with the vertical (z) component are picked in SAC software (Goldstein et al., 2003). P waves are picked from the vertical sections, and SH waves are picked from transverse. Picks are classified according to their motions, impulsiveness and qualities. Motions can be up or down, for both types of picks, but in SAC convention, up motion of SH pick is typed as right and down is typed as left. Impulsiveness of picks can be impulsive or emergent as shown in the example (Figure 15). Furthermore, picks are classified as excellent, good, okay, bad and very bad according to their quality.

Phase picking process is ended up with 172 well-picked events. Wadati diagram of all these picks are given in Figure 16. This diagram shows that most of the picks are determined well according to the trend line, whereas the scattered data has low-quality picks. A clear example of a record section is shown in Figure 17, where red lines indicate P picks and green lines indicate SH picks.

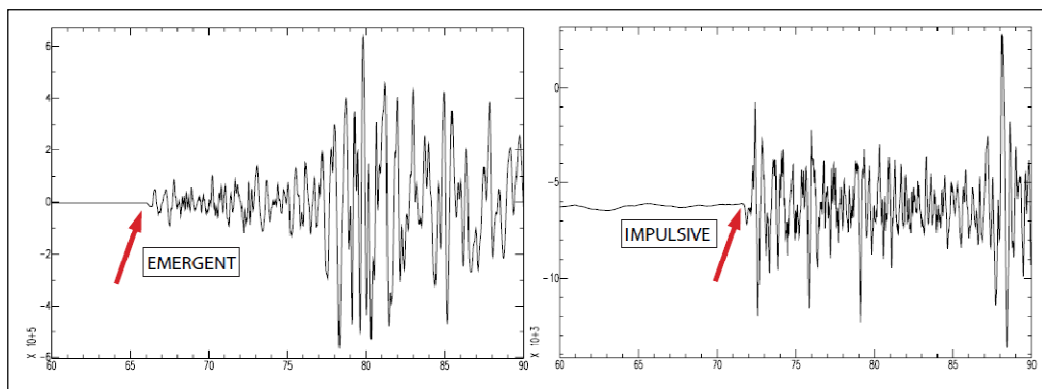


Figure 15. Example for emergent (left) and impulsive (right) arrivals of two different events, recorded by the same station.

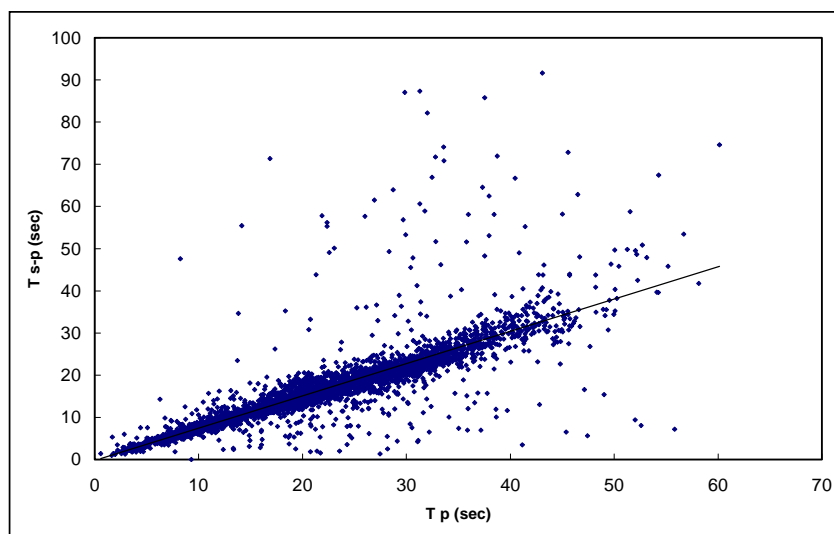


Figure 16. Wadati diagram for all events.

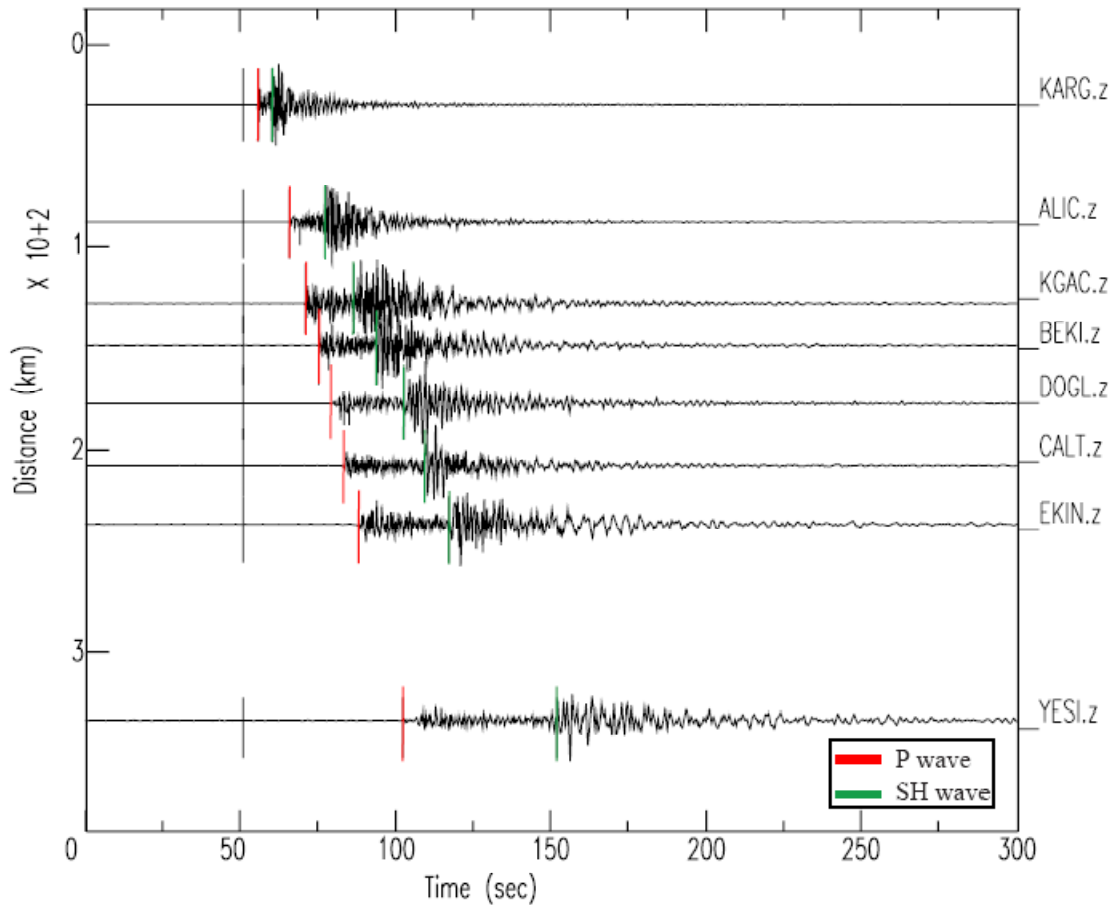


Figure 17. Example of a record section of well-picked phases.

3.2 Earthquake Relocation

Earthquake relocation is considered to be a classical inverse problem in seismology. Locating an earthquake and finding its origin time depends mostly on the velocity structure of the region since it defines raypaths; and thus the arrival times of seismic waves which are recorded at various stations (Stein and Wysession, 2003).

In this study, HYPOCENTER program is used for the relocation of the earthquakes. HYPOCENTER is a Fortran program for locating local, regional and global earthquakes that is described by [Lienert \(1994\)](#). In the HYPOCENTER program, earthquake location problem is solved by centering and scaling the observed matrix in combination with adaptive damping of the least-squares solutions, which provide an effective and simple solution (Lienert et al., 1986).

For hypocenter relocation, picks of all events are reviewed and higher quality picks, having 3745 P- and 973 S-phase arrival times, are processed in HYPOCENTER program. Wadati diagram given in Figure 18 shows the high quality data and resultant Vp/Vs ratio (Figure 18). Velocity models of Toksoz et al. (2003) CNAF and IASP were chosen as initial trial models in the relocation process (Table 1).

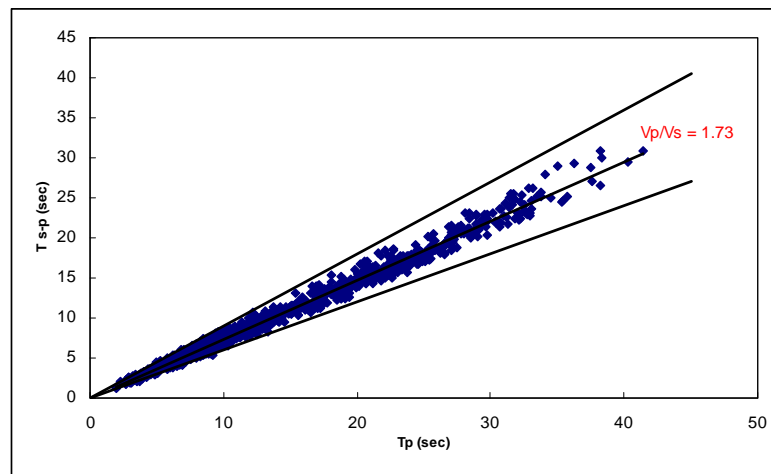


Figure 18. Wadati diagram of events after the elimination of the phases lying far of the main trend. The Vp/Vs ratio is 1.73

Table 1. Initial trial velocity models (IASP, Toksoz et al., 2003).

CNAF		IASP	
Depth (km)	Velocity (km/sec)	Depth (km)	Velocity (km/sec)
0	5	0	5.8
6	5.5	20	6.5
10	6.3	35	8
35	7.8		

3.3 Calculation of 1-D Crustal Velocity Model

As mentioned previously, velocity structure of the region is crucial in locating earthquakes. Moreover having a well-determined average velocity model is important in order to analyze seismotectonic structures more accurately. Therefore, after the earthquake location procedure, 1-D velocity of the study area is determined by VELEST (Kissling, 1995). VELEST is an iterative 1-D inversion algorithm, which solves for hypocenter locations, determines the optimum 1-D crustal velocity model, and associated station delays.

For the velocity model determination of the study area, outputs gathered from HYPOCENTER program are used. Higher-quality events with azimuthal gap ($GAP \leq 120^\circ$), number of observations ($P \geq 13$ and $RMS < 1$) are selected from initial data set. This selection criteria ended up with 98 events of which higher quality picks (1666 P-phase readings) are reselected in order to have a well-determined velocity model. Only P picks were used since VELEST accepts only one phase for the same station for each event. Low velocity zone, as suggested by Kissling (1995), is not used during the model determination. V_p/V_s ratio is selected as 1.73, which is obtained from the Wadati diagram (Figure 19).

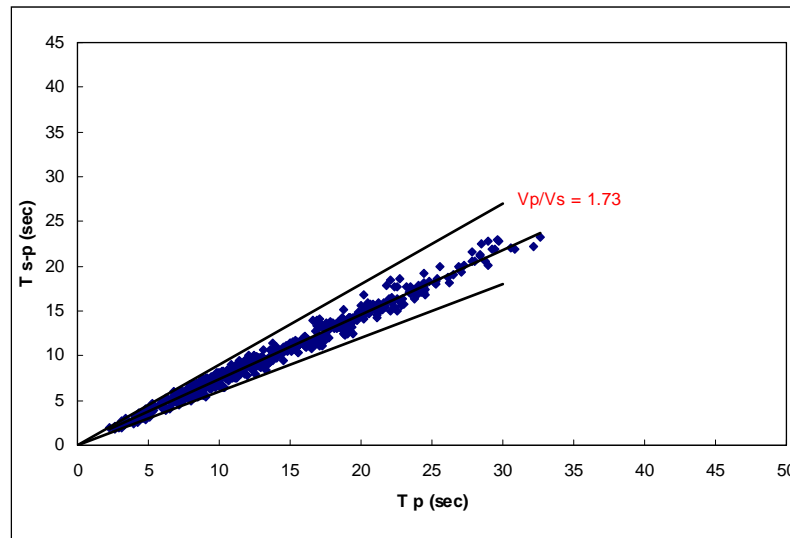


Figure 19. Wadati diagram after the selection of events for the velocity inversion. The V_p/V_s ratio is 1.73.

The inversion process is strongly dependent on the starting model. In order to solve this problem, the process is started with two different initial models (IASP and CNAF; see Figure 20 and Table 1). Various combinations of damping factors (velocity, station and hypocentral dampings) are tried in order to prove the stability of results. Over hundred inversion tests, each having nine iterations, are performed. During the inversions, it is observed that, the RMS errors for both initial velocity models reduced generally after the second or third step. Another criterion of the inversion process is the selection of damping parameters which highly affects the initial inversion step. To overcome this problem, hypocenter parameters are overdamped during the whole inversion process. Moreover, dampings of station delays are kept higher (1.0) than velocity model (0.01) in the first inversion, to constrain velocity model better (Figure 21). In the second run, dampings of station delays and models are kept equal (0.01). The aim of second run was to determine required station correction values. In order to test the stability of the final model, an average model is created from the output models of the first inversion and it is inverted using the same criteria (Figure 22).

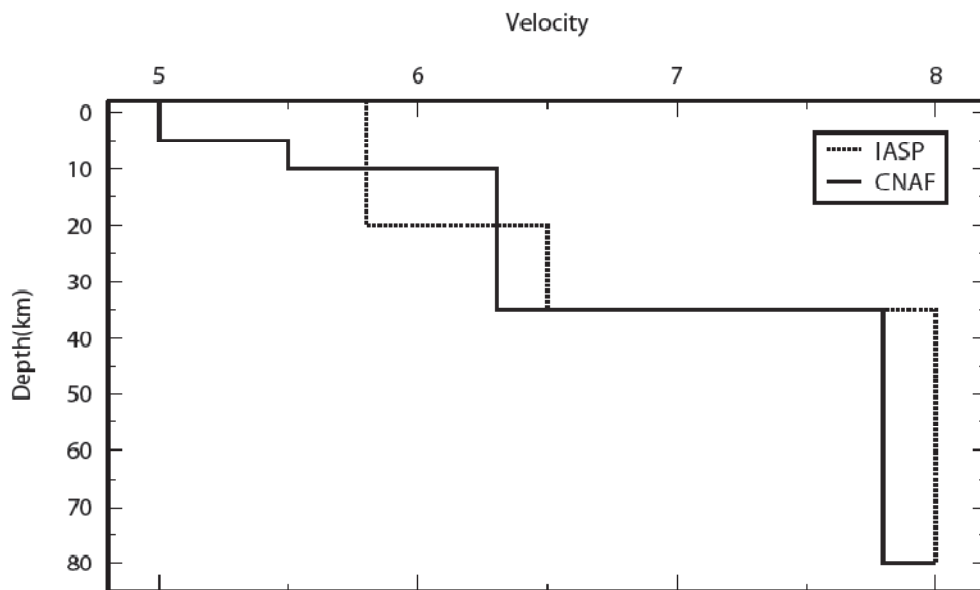


Figure 20. Initial trial velocity models (IASP, Toksoz et al., 2003).

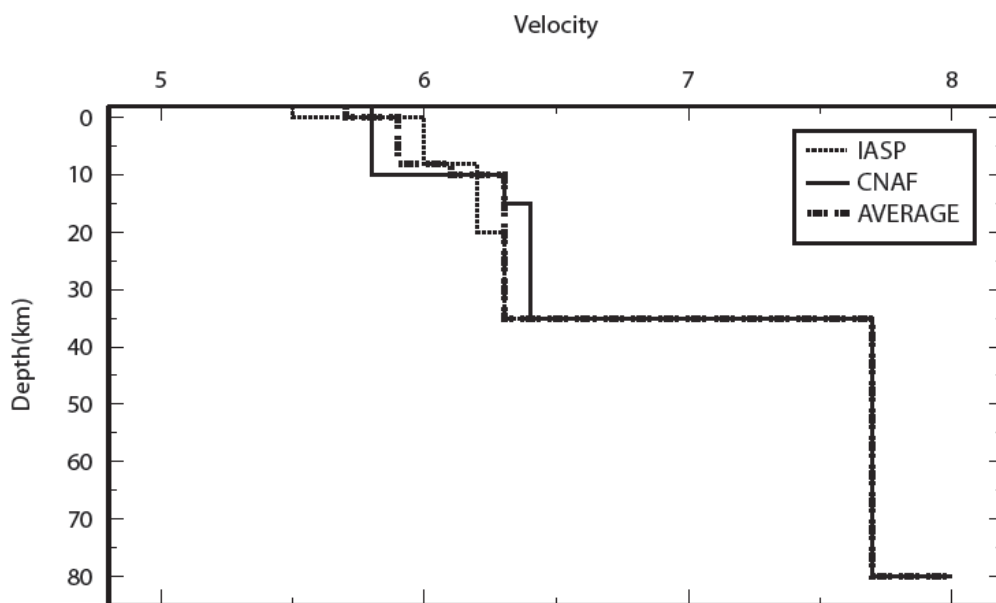


Figure 21. Velocity models showing the results of first inversion and the average model selected from this result.

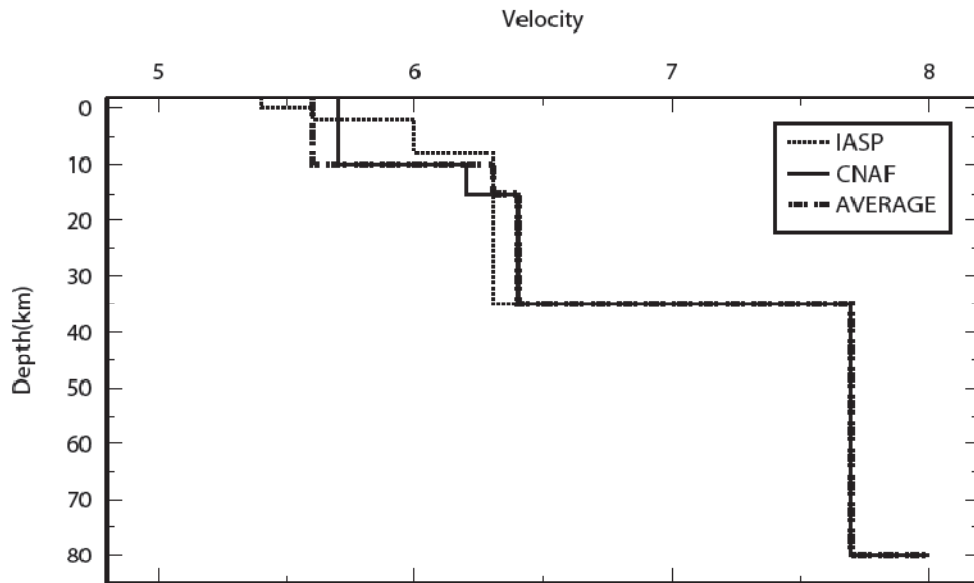


Figure 22. Velocity models resulted from the second inversion.

3.4 Results

3.4.1 Velocity Model

At the end of final inversion step, all three models showed converging trends. Results of CNAF and average showed nearly the same pattern (Figure 22). The velocity model, which resulted in the best trade-off between station delays and had the minimum RMS value, is selected as the minimum 1-D velocity model, together with the station residual values (Figure 23 and Table 2).

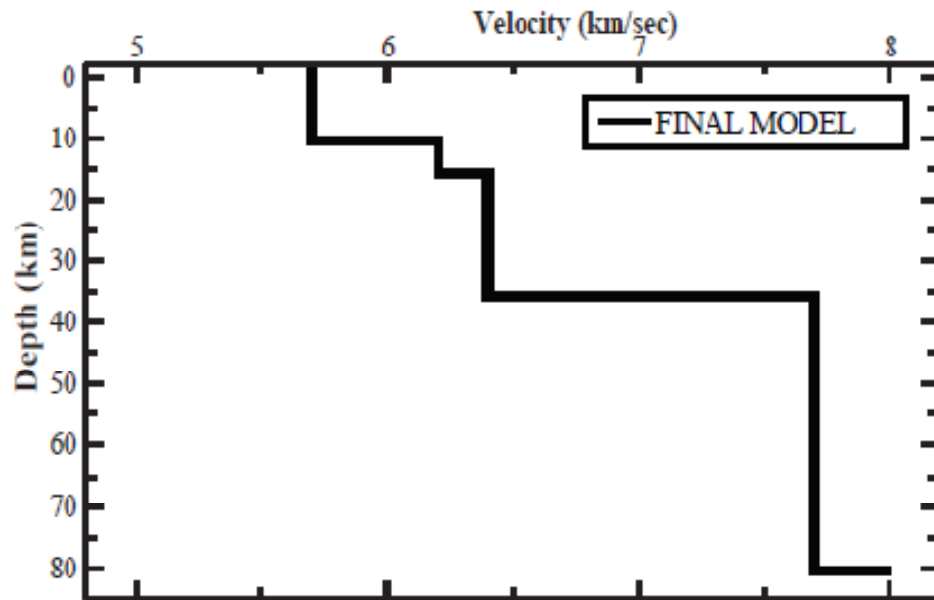


Figure 23. Selected 1-D velocity model.

Table 2. Selected 1-D velocity model.

FINAL MODEL	
Depth (km)	Velocity (km/sec)
0	5.7
10	6.2
15	6.4
35	7.7

The final 1-D velocity model (Figure 23), is in good agreement with the average crustal structure of the region. It has an average velocity of 5.7 km/s for the upper 10 km depth. In the second layer down to 35 km depth, velocity increases to 6.3-6.4km/sec. More

accurate results are obtained in this layer, due to depth distribution of the events. Below 35 km, where MOHO depth is reached, uppermost mantle is 7.7 km/sec, which is slower than global average.

3.4.2 Station Delays

Station corrections are given in Figure 24 and Table A. 4. In order to compute the station corrections, reference station should be selected at first, and all other station residuals are calculated with respect to this station. In this study, station KGAC located near the center of the network with the highest number of records is selected as the reference station and its correction value is assigned as 0.

Resultant station corrections can be mainly subdivided into three groups. First group is located in northern part of the study area and shows positive values, which corresponds to fact that true velocities should be faster than 1-D model. In the middle of the region, mostly negative values are observed, relating that true velocities are supposed to be slower than the 1-D velocity model. Most station corrections with high values are placed on the NAF and its splays. Finally, southern part of the area reflects a relatively smaller group of positive station correction values. Positive values are generally seen in areas that lie outside of the deformation zone. The largest station delays are observed in stations BAGB and INSU (0.46 and 0.53, respectively) which can be due to poor site conditions and network coverage.

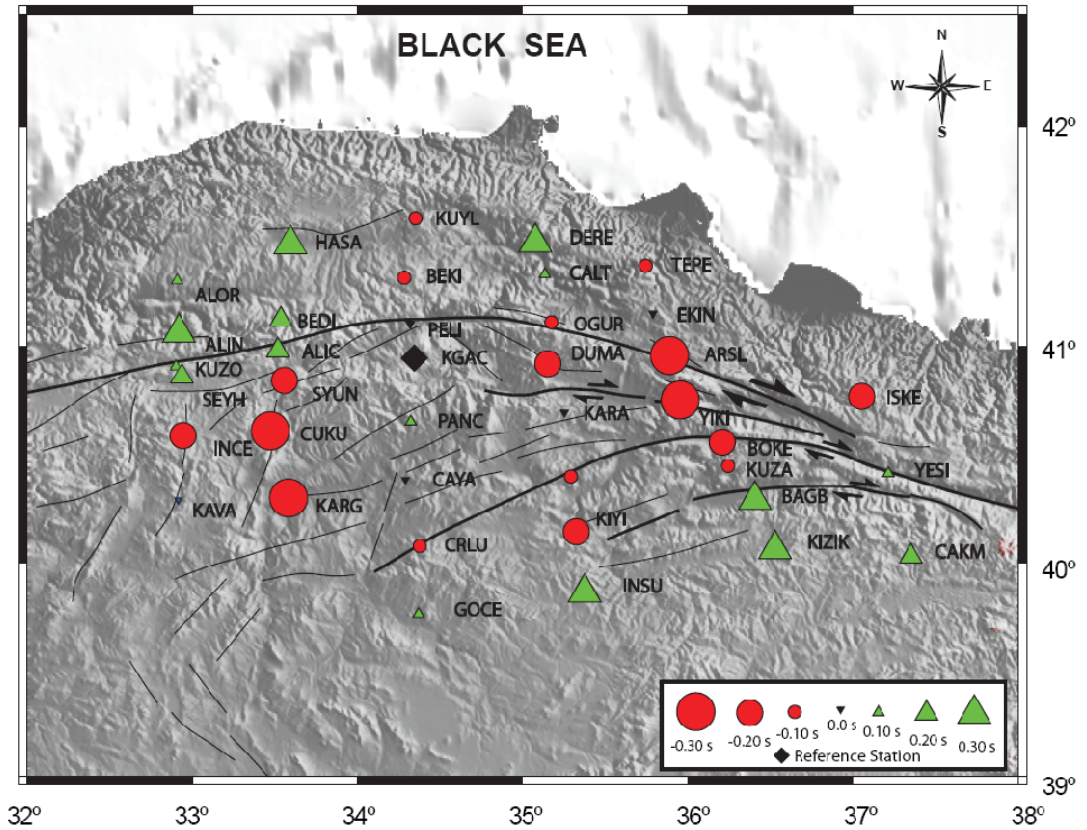


Figure 24. P-wave station corrections for the final 1-D *P*-wave velocity model. Red circles and green triangles on the map show the negative and positive station delays relative to the reference station, respectively. The reference station KGAC is marked by a black diamond. The correction values equal to 0.0 s are shown as inverse triangle. Sizes of the all symbols are scaled to correction values, except reference station. See Table A. 4 for detailed information.

3.4.3 Earthquake Locations

Relocation process is repeated using HYPOCENTER program with updated 1-D *P*-wave velocity model and resultant station correction values and it is ended up with 152 well-relocated events (Figure 25, Table A. 5). There are small variations in latitude and longitude, whereas significant changes are observed in depth values. Depths are mainly

limited to top 20 km and earthquakes are widely distributed suggesting a broad zone of deformation in the southern block. This new velocity model and station corrections reduced the RMS error of selected 98 events by %60 from 0.32 to 0.20. Overall RMS of 172 data is decreased from 0.58 to 0.54. (Figure 26).

Relocation process revealed out the existence of a major cluster located in the central part of the region. Close up view (Figure 27) of this “Çorum” cluster shows that all earthquakes in this part converged together after relocation. .

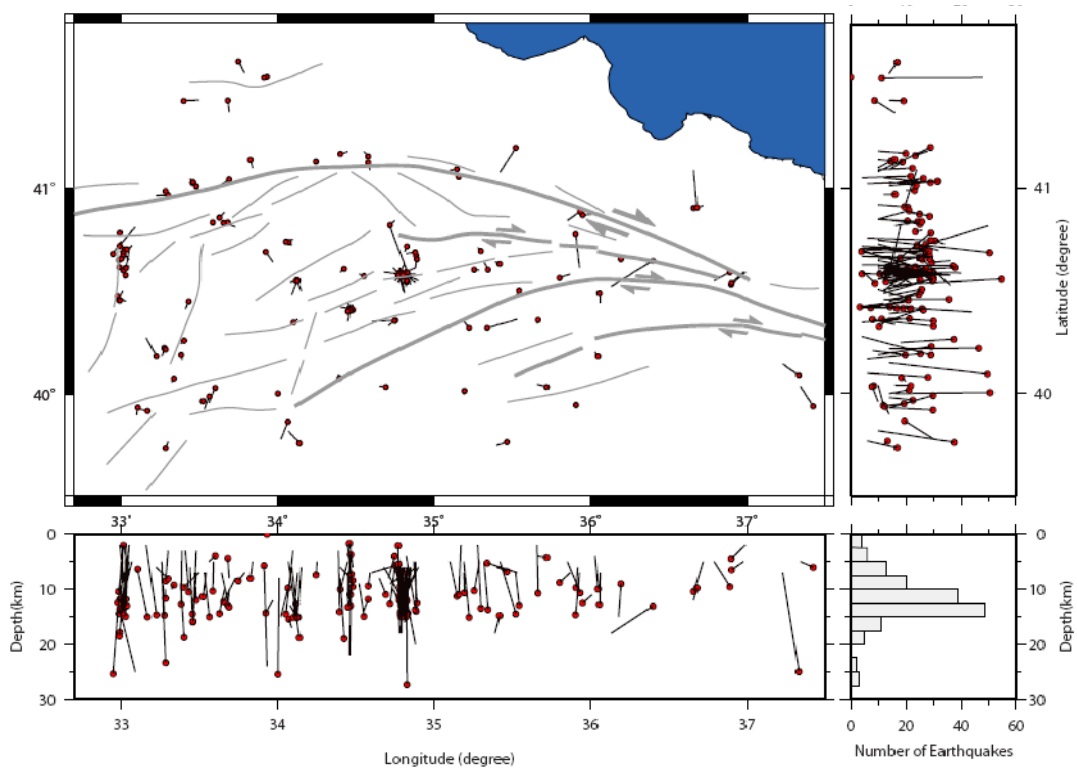


Figure 25. Epicentral and hypocentral shifts relative to the preliminary hypocenter location, after the final earthquake relocation. New epicentral locations are shown with red circles (see Table A.4). The vectors indicate epicentral shifts between initial and final locations. Major faults are shown by gray line. See table A. 5 for detailed information.

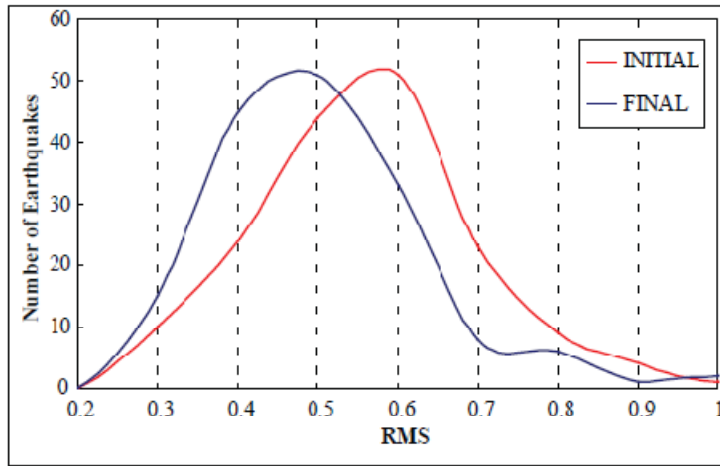


Figure 26. Comparison of RMS values between initial and final relocation results of all 172 earthquakes.

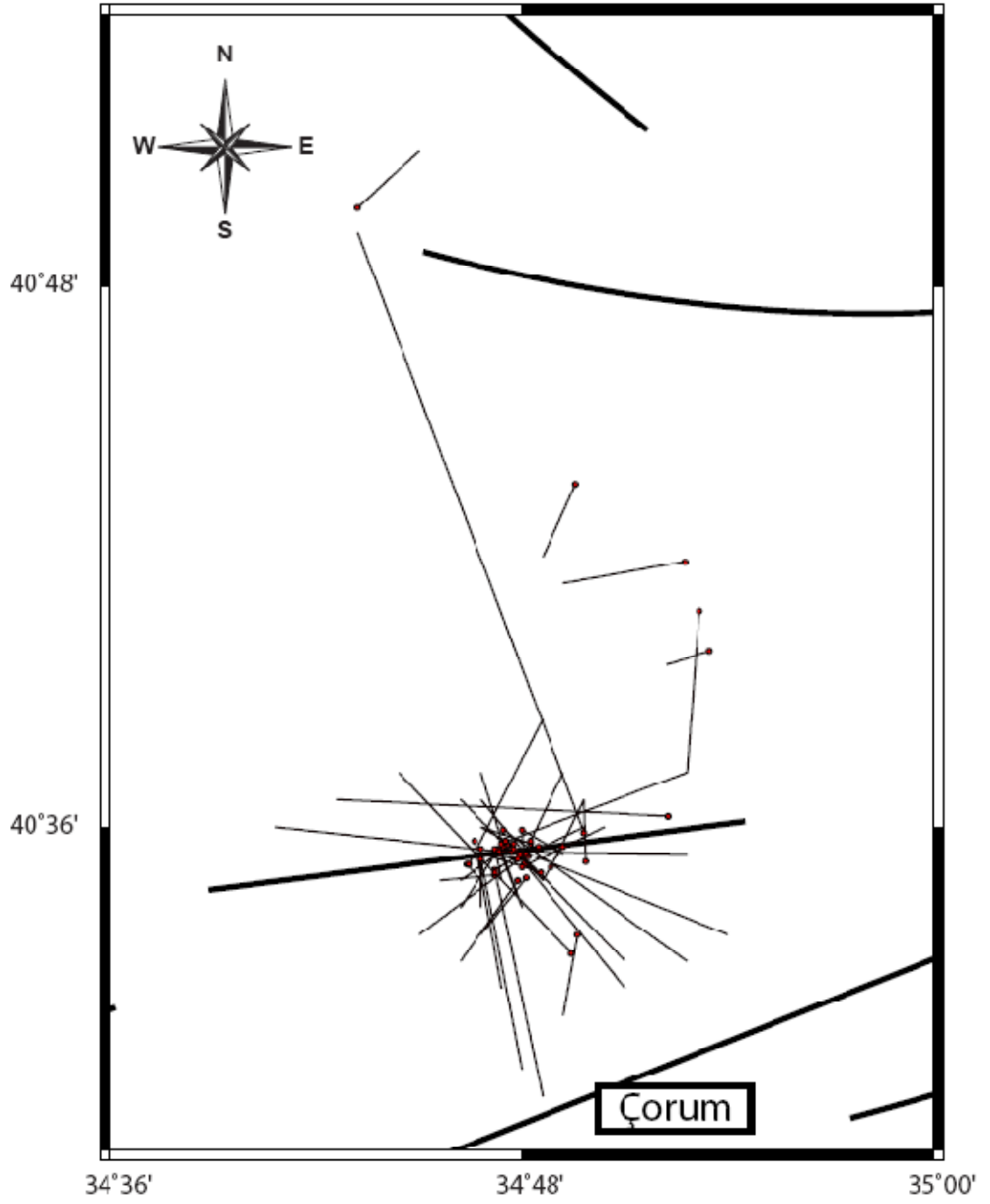


Figure 27. Epicentral and hypocentral shifts relative to the preliminary hypocenter location, after the final earthquake relocation of Çorum cluster.

CHAPTER 4

FOCAL MECHANISMS AND STRESS TENSOR ANALYSIS

4.1 Focal Mechanism Determination

A focal mechanism solution describes the geometry and mechanism of the faulting during an earthquake. It can be constructed from waveforms generated by an earthquake, recorded by a number of seismograms at various distances and azimuths. The basic idea of determining focal mechanism solutions relies on the fact that the pattern of radiated seismic waves depend on the fault geometry (Stein and Wysession, 2003).

The determination of the focal mechanism solutions can be done by various methods. In this study, a classical approach, polarities of P-wave first motions are used. P-waves are the seismic waves that are first to be recorded from the earthquake source because of their highest velocity. First-motions of P-waves, or polarities, indicate the direction of the motion recorded at the seismometer. Focal mechanisms can be determined by observing P-wave polarities recorded at a number of different stations (Walsh et al., 2008 and references therein).

The direction of first motions defines four quadrants (two compressional, two dilatational) surrounding the source (Figure 28). “Upward” motion of first waves defines compressional quadrants, where earth moves “toward” the station. “Downward” motions define dilatational quadrants, where the movement is “away from” the station. The

division of these quadrants occurs along the fault plane and a plane (auxiliary plane) perpendicular to it, which together are called the nodal planes. These planes can define the fault geometry, but actual fault plane can not be determined with first motion data alone. The first motions produced by slip on both planes would be the same, so that these two planes would have no structural significance. This ambiguity can be resolved with the additional geologic or geodetic information (Stein and Wysession, 2003).

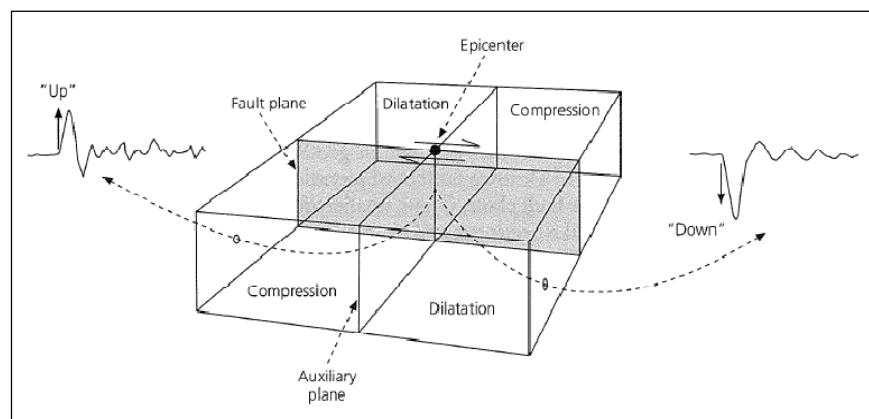


Figure 28. Schematic view illustrating the basic concept of the determination of focal mechanism from P-wave first motions, for a strike-slip earthquake on a vertical fault (Stein and Wysession, 2003).

To determine a focal mechanism, first motion polarities of P-waves are plotted on lower-hemisphere stereonet. Once all polarities are plotted on the stereonet, it results in a “beachball” appearance. It is partitioned into four quadrants and they are separated by great arcs orientated 90 degrees from each other (Stein and Wysession, 2003). The great-arc circles correspond to the nodal planes, dark and light colored quadrants define compressional and dilatational first motions, respectively (Stein and Wysession, 2003).

Here, Figure 29 shows a clear example of first motion data picking carried out in this study.

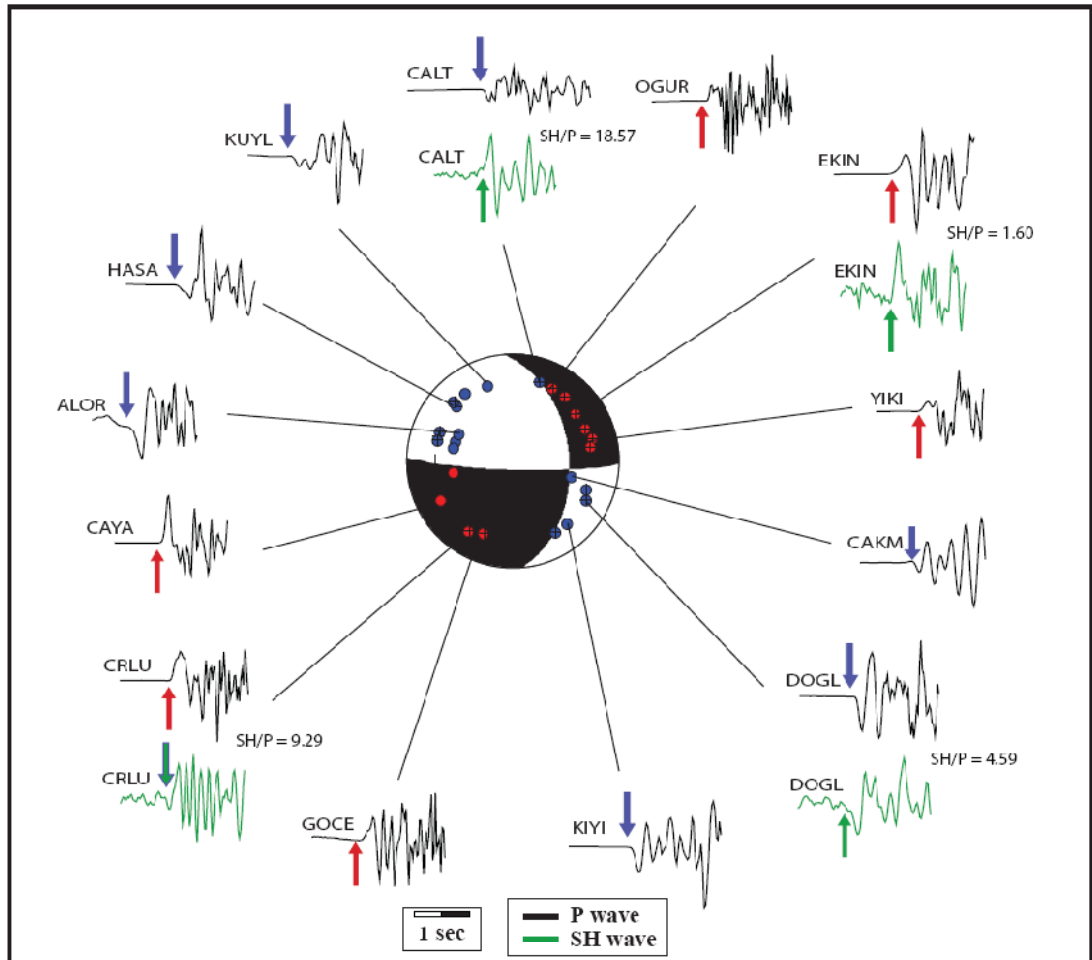


Figure 29. An example of a well-determined focal mechanism solution. Each P- and SH-waveform data used for determination of this solution are shown in vertical traces. First motions of P- and SH- waves are marked with black and green vertical lines, respectively. Red dots indicate compressional (up) arrivals and blue dots indicate tensional (down) arrivals. Calculated SH/P ratios are given also, when clear SH picks are available.

S-waves, so called secondary waves, are slower than P-waves and they are recorded as the second direct arrival on a seismogram. In determining focal mechanisms, S-wave polarization and S/P amplitude ratios can be used to have a more unique solution.

S/P amplitude ratios provide useful information, when radiation patterns of P- and S-waves are considered (Figure 30). P-wave amplitude diminishes near the nodal planes, whereas S-wave amplitude reaches to its maximum value. Therefore, large S/P ratios define a point near a nodal plane and vice versa. To check the correctness of the solution, observed S/P amplitude ratios can be compared with theoretical ratios, defining a misfit error. A major disadvantage of using amplitude ratios is that S-wave polarities are hard to pick due to noise and attenuates quickly as the wave propagates (Walsh et al., 2008 and references therein).

Orientation of *P*- and *T*-axes can also found using first motion data. When focal mechanism determination is complete, *P*- and *T*-axes can be found by bisecting the dilatational and compressional quadrants, respectively. This is done by using the great circle connecting the poles for the nodal planes and finding the half way between them. On the focal mechanism solution, *T*-axis lies at the center of compressional quadrant (dark colored), whereas *P* axis lies at the center of dilatational (light colored) quadrant (Stein and Wysession, 2003).

In this study, focal mechanisms are determined from P and SH polarity data and amplitude ratio (SH/P) using the grid scheme FOCMEC program (Snoke, 2003). Pick information, together with related SAC files put together to FOCMEC. Angle of incidence of rays at each recorded station are determined by raytracing program TauP (Crotwell et al., 1999), with the 1-D final velocity model.

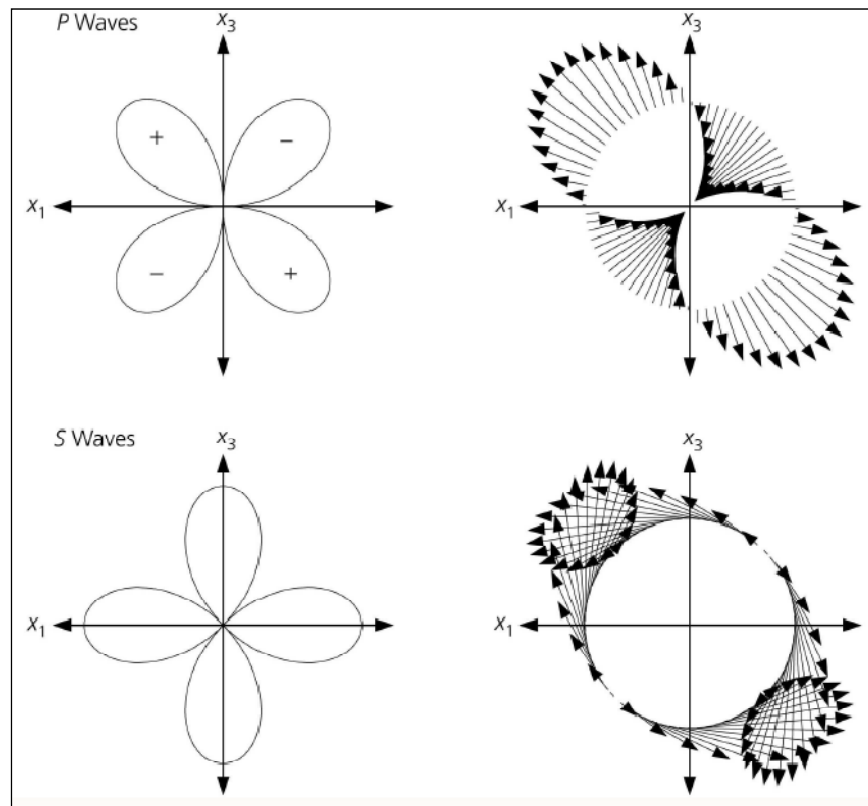


Figure 30. Fault geometry and radiation amplitude patterns of P and S waves in the $x_1 - x_3$ plane (Stein and Wyssession, 2003).

FOCMEC uses an inversion scheme that searches for the acceptable focal mechanism solutions using first motion data. In addition to first motion data, FOCMEC also uses first-motion amplitude data (SV/P, SH/P, and SV/SH) to have better determined solutions. The possible solutions are determined by a grid search approach, with minimum polarity and/or amplitude errors (Anderson et al., 2007). Users can define necessary criteria needed for focal mechanism determination. When amplitude ratio is included, corresponding amplitude ratio error is calculated according to the maximum allowed \log_{10} ratio (Anderson et al., 2007). This value is the maximum limit, up to which the difference between the theoretical amplitude ratio and related observed ratio can reach. Values greater than this limit are assigned as amplitude error.

A moving time window of 0.2 second is used to calculate the amplitude ratio (SH/P). Maximum allowed \log_{10} ratio is selected as 0.6 and for the grid search 5° increment is used. FOCMEC is constructed to allow increasing number of data errors, such that it will constantly violate polarity data until it finds a solution. If it finds too many solutions (>25) it will increase the search increment. Events with less than 4 arrival data points are not included to the program.

As mentioned earlier, once the nodal planes of an event are defined, it is possible to determine the orientations of P - T -axes. For a single event, FOCMEC automatically determines trend and plunge of P - T -axes, for each potential solution. Furthermore, mean value of these axes are found by applying Fisher statistics. Main problem of calculating mean of P - and T -axes is handling a dataset whose basic information is a direction (Watson, 1966). Fisher statistics, in a very basic definition, is the statistical analysis of the directional data, in which a mean direction from observed directional data is calculated (Tauxe et al., 1991). Accuracy of the results depends on the value of precision parameter, κ , where high values of κ (greater than 20) represent less scattered data. Precision parameter is important because less scattered data indicates less dispersed potential solutions (Anderson et al., 2007).

At the end of the FOCMEC run, all these information are plotted in a one page summary, as an output for each event. This plot summaries all the possible solutions and their related data. An example of this plot is given in Figure 31, which shows the location of the event in a map view and gives out the potential solutions in two separate columns. Solutions in the first column are calculated using only polarity data. Just beneath each solution, P and SH polarity error can be seen. In this example 4 potential solutions are calculated using only polarity data. At the bottom of the page, all the data, orientations of picks and nodal planes are summarized in “Data” steronet. P - and T -axes for each solution and their mean value is plotted in “P/T axes” steronet. After these steronets, numerical data, including precision parameter, confidence level of mean P and T axes, polarity data, total polarity errors and search increment is given. Second column

of the page shows the solutions obtained by using polarity and amplitude ratio data. Same parameters included in the first column are also given here, with additional amplitude data records and related errors. Note that RMS log ratio error for each solution is given, together with the P and SH polarity errors.

Once potential solutions are determined, representative solution for each event needs to be selected. This selection is done by reviewing all the events according to their polarity, amplitude, RMS errors, precision parameter and confidence level values. Usually solutions with polarity and amplitude data are selected, since using amplitude data results in more unique focal mechanisms. At the end optimum solutions with lowest polarity, amplitude and RMS error are chosen as best mechanisms. It should be noted here that, events showing different types of mechanisms among its potential solutions are not included for further analysis.

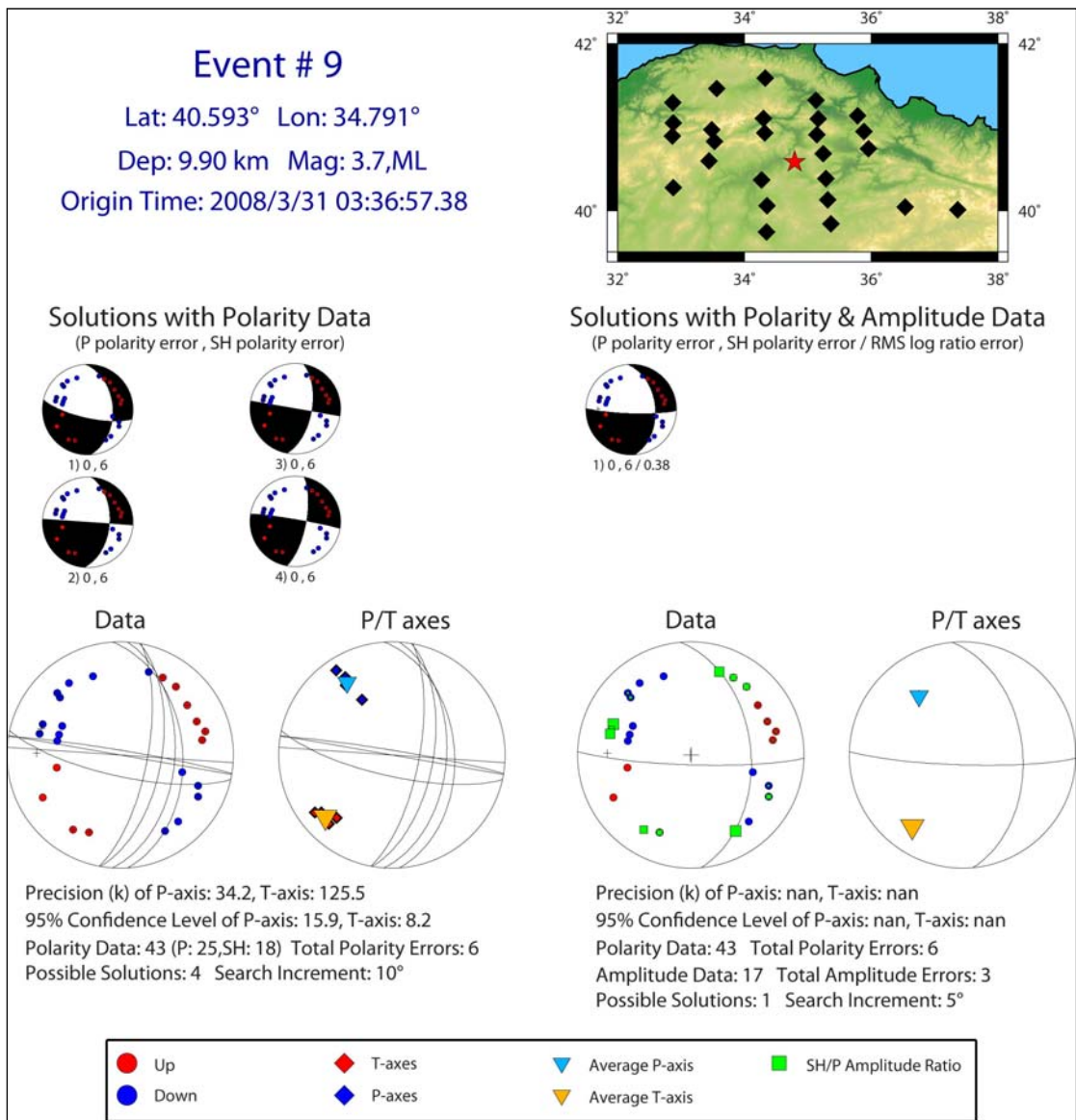


Figure 31. An example of an output plot that summarizes all the possible solution mechanisms and related data.

4.2 Stress Tensor Inversion

Many stress inversion techniques have been proposed for the determination of stress field orientation from focal mechanism solutions. Best known methods are Gephart and Forsyth (1984) and Michael (1984). The aim of both methods is to determine the stress which minimizes the discrepancy between the resolved shear stress direction and the slip direction for all data set. These algorithms solve for the orientations of three principle stress axes and the relative magnitudes of the stress axes $R = (\sigma_2 - \sigma_3) / (\sigma_1 - \sigma_3)$. Here σ_1 , σ_2 , σ_3 indicates maximum, intermediate and minimum principal compressive stresses, respectively (where $\sigma_1 \geq \sigma_2 \geq \sigma_3$).

Gephart's method uses a grid search approach to obtain the stress tensor which minimizes the misfit between model and data (Hardebeck and Hauksson, 2001 and references therein). The best-fitting stress model is obtained when the angular misfit between the predicted and the observed fault planes slip direction is minimum (Tselentis et al., 2006).

Michael's method determines the orientation of three principle axes and stress magnitude by the statistical method of bootstrap resampling (Görgün et al., 2010). Basic aim of this technique is to find the best fitting stress tensor to the observed focal mechanisms (Görgün et al., 2010). Heterogeneity of a stress field can be quantified with variance, defined as the squared and summed solution misfit, which is the angle between the individual focal mechanism and the assumed tensor (Wiemer et al., 2002). For a spatially uniform stress field determined by focal mechanisms data, variance should be less than 0.2. High variance indicates poor fitting stress orientation and hence stress field remains heterogeneous within the analyzed volume (Wiemer et al., 2002).

Hardebeck and Hauksson (2001) compared these two methods in detail, applying them on synthetic focal mechanism data sets. According to this comparison, both models can

determine stress parameters accurately and increasing data set can improve the accuracy of results. Basic difference between two methods is that, the method of Gephart and Forsyth (1984) results in more reliable stress orientations with high-quality data sets, whereas the method of Michael (1984) provides more accurate estimates with very noisy data sets. Both models assume that (1) the stress in the study is uniform and invariant in space and time, and (2) earthquake slip occurs in the direction of maximum shear stress (Delvaux and Barth, 2010).

In this study, stress inversion is done by using Michael's method and processing is carried out with ZMAP software (Wiemer, 2001). In addition, Gephart's method is applied to compare the results. For the inversion three different data sets are used. First, inversion is done using resultant 109 well-constrained focal mechanisms, and then all data is combined together with the previous focal mechanism data of Turkey (Figure 13, Table A. 1). Finally Çorum cluster is examined separately. Applying these methods to all data sets gave the general trend of stress orientations. In order to examine the stress changes and to assess the quality of the results throughout the region, several plots are obtained showing the orientation of the trend of σ_1 bars, using different kinds of gridding with Michael's method.

4.3 Results

For the assessment of our focal mechanism results, regional and Harvard centroid moment tensor (CMT) solutions are used for comparison. Regional CMT is available for earthquakes with magnitudes ≥ 4.0 (Pondrelli et al., 2002, 2004, 2007) and Harvard CMT is available for earthquakes ≥ 4.8 (Dziewonski et al., 1987), therefore only one of our solution (Eq. 1, $M=4.9$) can be used for this comparison (Figure 32).

Our solution fits well with right-lateral strike-slip mechanism of Harvard CMT with minor difference in the orientation of nodal planes. It is also consistent with geology and

stress regime of the area. Although same nodal plane orientations exist in regional CMT, it gives out totally different slip direction. The difference between two catalogs is surprising and points out the question of uniqueness of these mechanisms. This ambiguity shows that, our study is necessary to have well-determined mechanisms for this region.

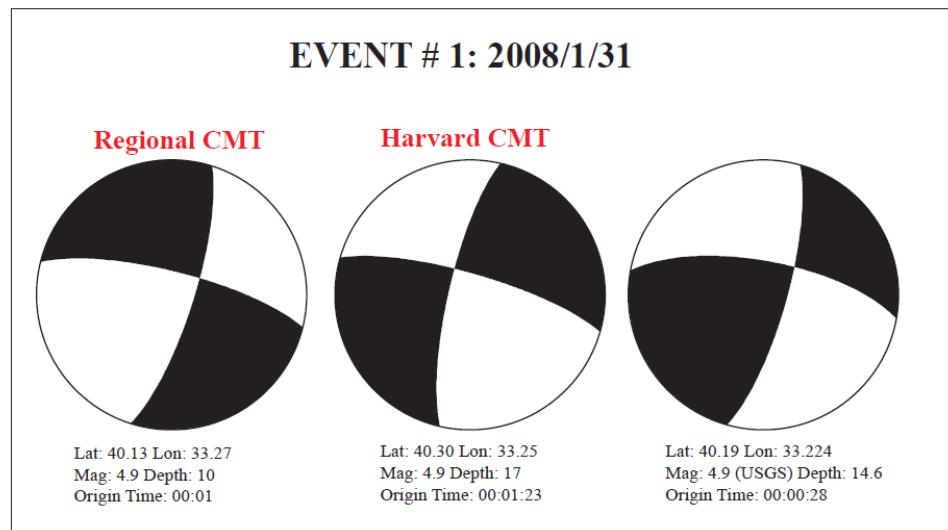


Figure 32. Comparison of our resultant focal mechanism for event 1 with solutions of Regional and Harvard Centroid Moment tensor (CMT) solutions.

Focal mechanism determination is ended up with 109 well-determined solutions (see Table A. 6, Appendix B). The distribution of the different mechanisms vary between strike-slip, normal to reverse but are mostly strike-slip. Rake-based Ternary diagram of resultant focal mechanisms (Figure 33) shows that apart from some normal and thrust faulting, strike-slip motion which corresponds well with the slip character of NAF and its splays is dominant in the region.

All mechanisms are localized in the southern block and mainly controlled by splays of the NAF. Most striking feature of the resultant mechanisms is the clustering of 36 events in the central part of the region, near Çorum. This region is analyzed separately in the section 4.3.1.

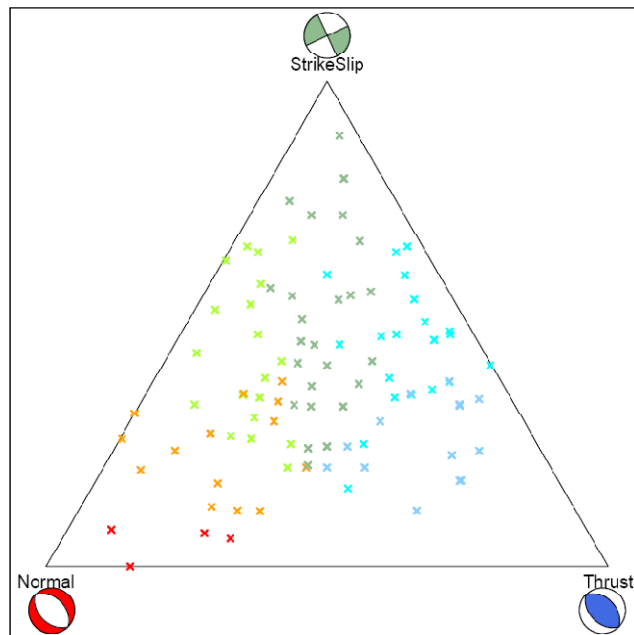


Figure 33. Ternary diagram of resultant 109 focal mechanisms determined in this study.

Most of the earthquakes along the NAF have right-lateral strike-slip mechanisms, consistent with the sense of slip of the fault (Figure 34). In the western part of the NAF, right-lateral strike-slip mechanisms are observed, some with thrust components (Eq. No: 10, 40, 82, 102). Central part of the NAF shows same type of mechanisms, which are discussed together with the Çorum cluster. When the eastern part of the NAF is considered, it is observed that fault plane orientations change with respect to the NAFs

arc-shape geometry. Mechanisms in this part are mainly localized at the right-lateral splays of NAF. Earthquakes 53, 80, are located in between NAF and LKF, shows the same slip motion, whereas a normal mechanism is observed with earthquake 58. Moving southward to the EZFZ, it is seen that earthquake activity is mainly present in northeast, with right-lateral mechanisms (Eq. No: 38). Same type of mechanisms (Eq. No: 37) exist in the southernmost splay AF.

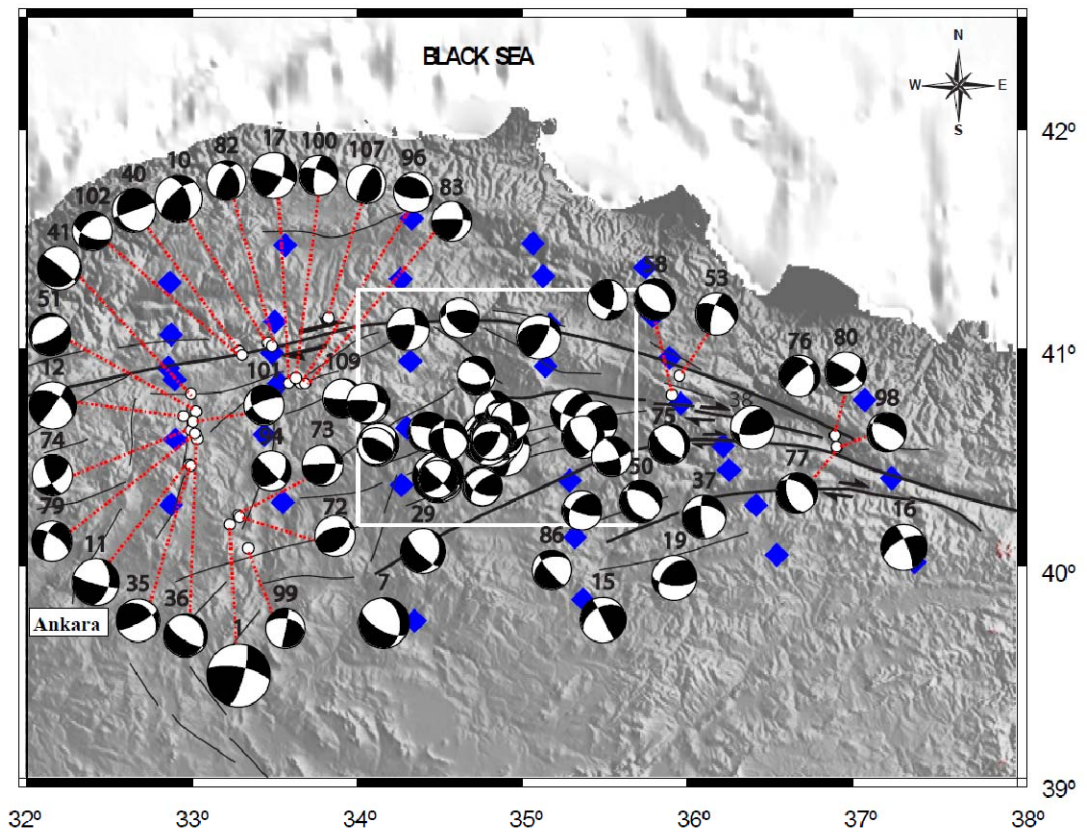


Figure 34. Fault plane solutions of 109 earthquakes determined in this study. The focal mechanisms are scaled to their magnitudes. For the fault plane information, see Table A. 6. White box defines the boundaries of the Çorlum cluster.

Western part of the study area has various types of focal mechanisms which are related to the N-S-trending parallel faults. Relatively a small cluster (Eq. No: 11, 12, 35, 41, 74, 79) located in the western part can be related to the left-lateral Dodurga Fault, trending approximately N-S. Parallel to this cluster, again a N-S-trending earthquake localization is observed including Eq. 1 (M= 4.9). These earthquakes occur along the N-S trending Eldivan Fault.

P- and *T*-axes orientations of all data is selected from the calculated mean of each event. Instead of selecting the representative solutions' *P*- and *T*-orientation, mean value is preferred. Because, mean value is calculated from all the possible solutions, and therefore it is more reliable. As a result, *P*-axes of overall 109 events have an average κ value of 366.5, with a 95% confidence level (α_{95}) 11°. Likewise, average κ value of *T*-axes is 1591 and α_{95} is 9.5° (Table A. 7).

In order to determine a general *P*- and *T*-axes orientation for the entire region, overall average of *P*- and *T*-axes orientation for all data (109 events) is calculated by applying Fisher statistics. Resultant *P*- and *T*-axes orientations (Figure 35) for the entire region suggest NW-SE compression, and NE-SW dilatation, which is also consistent with the tectonic regime of NAF's right-lateral strike-slip motion.

Furthermore, *P*- and *T*-axes orientations are classified according to the tectonic regime assignment proposed by Zoback (Table 3), using the plunges of these axes (1992). Figures 36 and 37 show these faulting types in color-code, with associated horizontal projection of *P*- and *T*-axes trends, respectively. Resultant histogram (Figure 38) shows that dominant faulting type is found out to be strike-slip, with minor normal and thrust components. Along the main strand of NAF, changing trends of *P*- and *T*-axes are consistent with the arc-shape geometry. Different kinds of faulting types are observed especially in the central and western clusters. However, about 30% of earthquakes can not be classified (shown in black color).

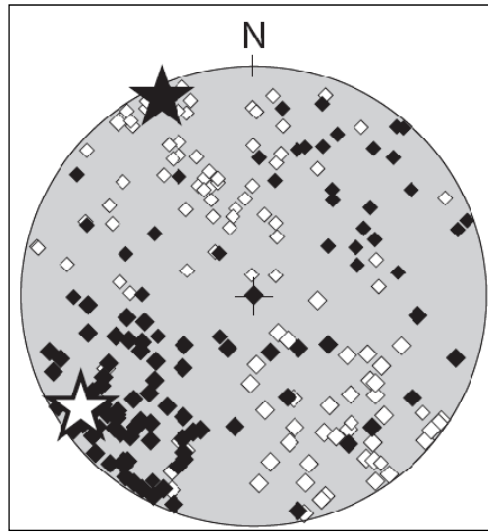


Figure 35. Distribution of all *P*- and *T*-axes orientations calculated in this study together with their average value are shown in stereographic projection. Black diamonds show *T*- axes and white diamonds show *P*-axes. Average values are of *P*- and *T*-axes are indicated by black and white stars, respectively. See Table A. 7 for detailed information.

Table 3. Tectonic regime assignment (Zoback, 1992; taken from World Stress Map Project,).

P/S1-axis	B/S2-axis	T/S3-axis	Regime	S_H -azimuth
$p1 > 52$		$p1 < 35$	NF	azim. of B-axis
$40 < p1 < 52$		$p1 < 20$	NS	azim. of T-axis + 90°
$p1 < 40$	$p1 > 45$	$p1 < 20$	SS	azim. of T-axis + 90°
$p1 < 20$	$p1 > 45$	$p1 < 40$	SS	azim. of P-axis
$p1 < 20$		$40 < p1 < 52$	TS	azim. of P-axis
$p1 < 35$		$p1 > 52$	TF	azim. of P-axis

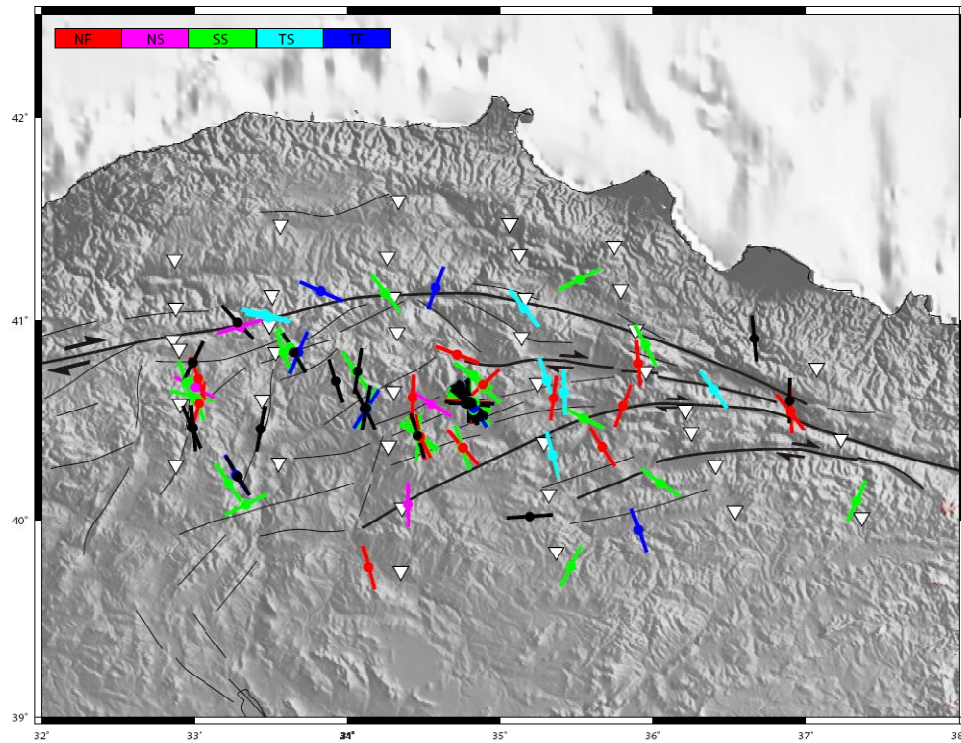


Figure 36. Focal mechanism data represented as *P*-axes orientations with colored coded faulting classes. Black lines define the earthquakes that can not be classified. NF= normal faulting, NS= predominately normal faulting with strike-slip component, SS= strike-slip faulting, TS= predominately thrust faulting with strike-slip component, TF= thrust faulting.

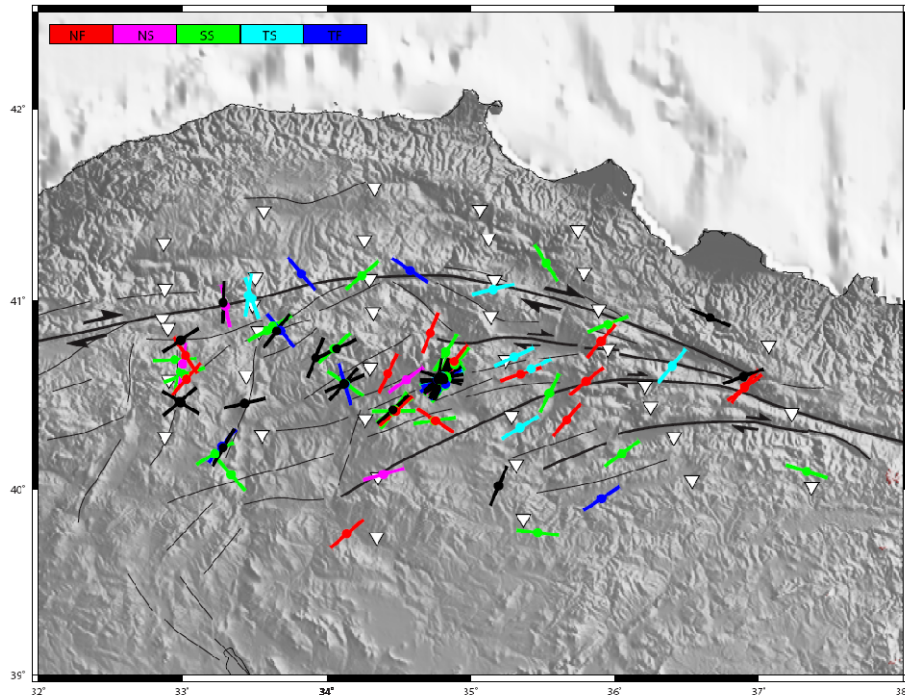


Figure 37. Focal mechanism data represented as *T*-axes orientations with colored-coded faulting classes.

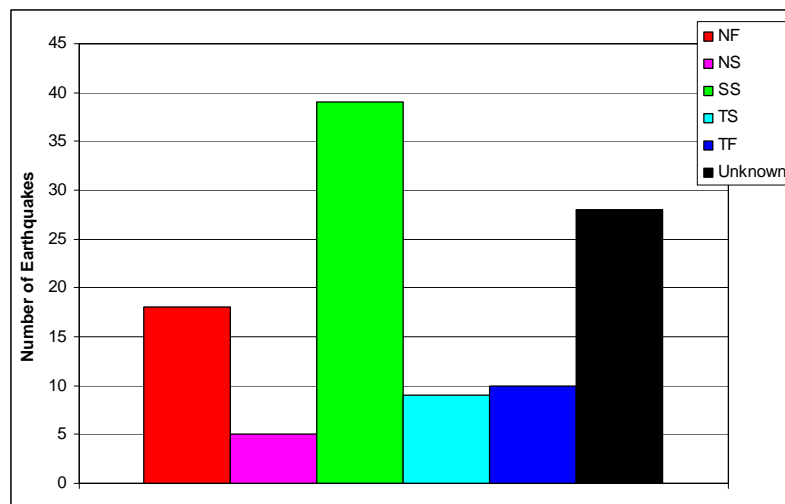


Figure 38. Histogram showing the type of faulting.

Initial stress inversion is done by using all focal mechanisms obtained in this study (Figures 39 and 40) and resulted in similar stress directions for both Micheal's and Gephart's methods. Maximum principal stress (39a), σ_1 , is found to be subhorizontal striking NW-SE, the intermediate principle stress, σ_2 , is vertically orientated and the minimum principal stress, σ_3 , is found to be NE –SW. Variance of the solution is 0.19 which is rather low suggesting relatively coherent stress directions across the region. Phi value which characterizes the style of faulting is 0.59 and suggests a strike-slip motion (Figure 39b).

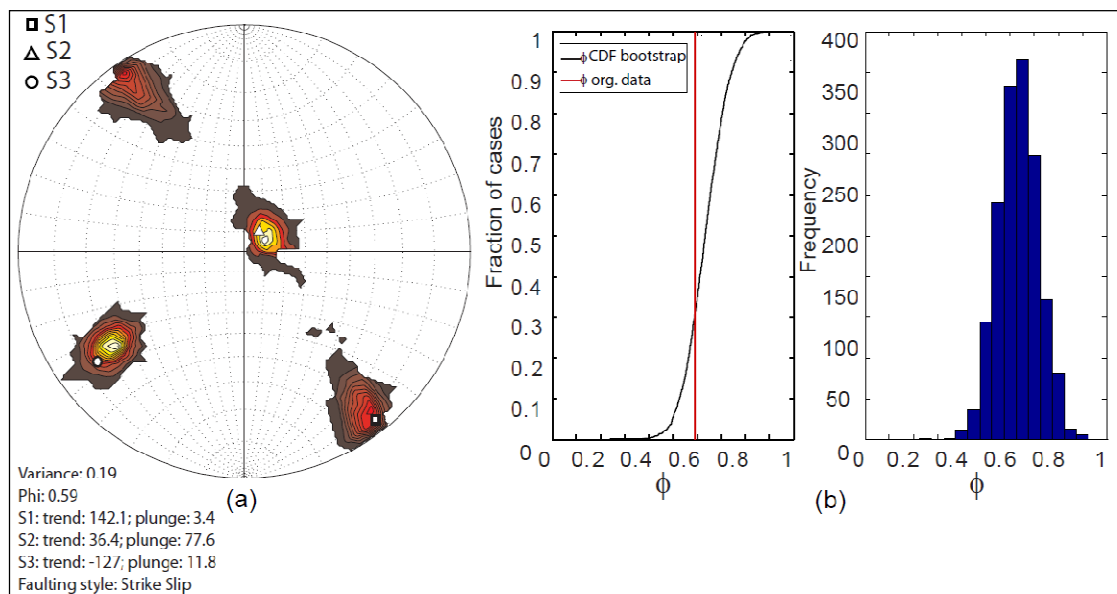


Figure 39. Stress inversion (a) and histogram of Φ values versus frequency (b) results of 109 focal mechanisms determined in this study, by Micheal's method.

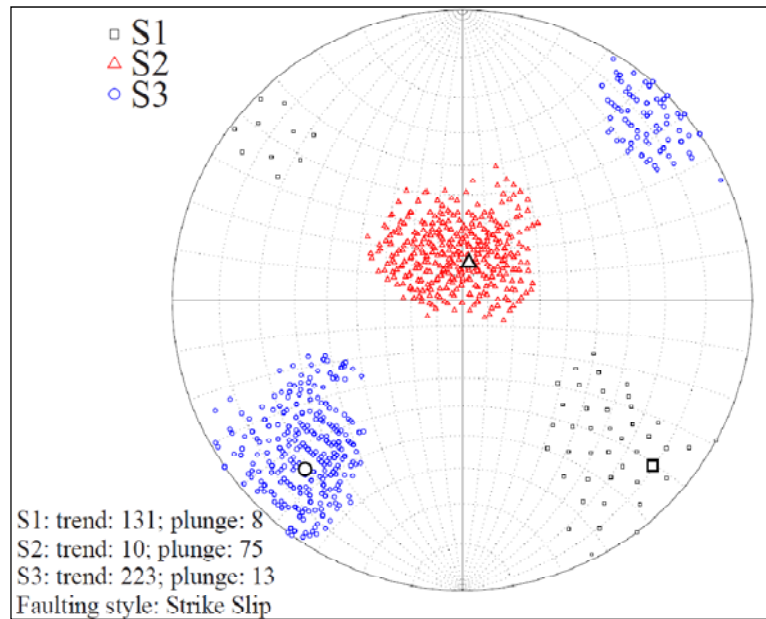


Figure 40. Stress inversion result of 109 focal mechanisms determined in this study, by Gephart's method.

When earthquake distribution along the region is considered (Figure 41), it is clear that our data has sufficient resolution to detect the changes in stress directions along the southern part of the NAF. Figure 42(a) shows the map views of fault classes in terms of trends of σ_1 orientations. This figure is produced by applying 0.1x0.1 degree spacing and 3 number of events for gridding. In the entire region, dominant faulting type is strike-slip faults, and their σ_1 orientations are consistent with the general trend. Thrust mechanisms are observed along the NAF, which is due to the change of σ_1 directions along with the arc-shape geometry of NAF. Distribution of the variance of the stress tensor at each node as plotted in Figure 42(b). Michael (1987) suggests that variances higher than 0.2 indicates a strong heterogeneity of the stress field. But it is normal when the scale of our study area is considered. Moreover, variance of the area including NAF and its splays is very low, indicating that σ_1 orientations are reliable.

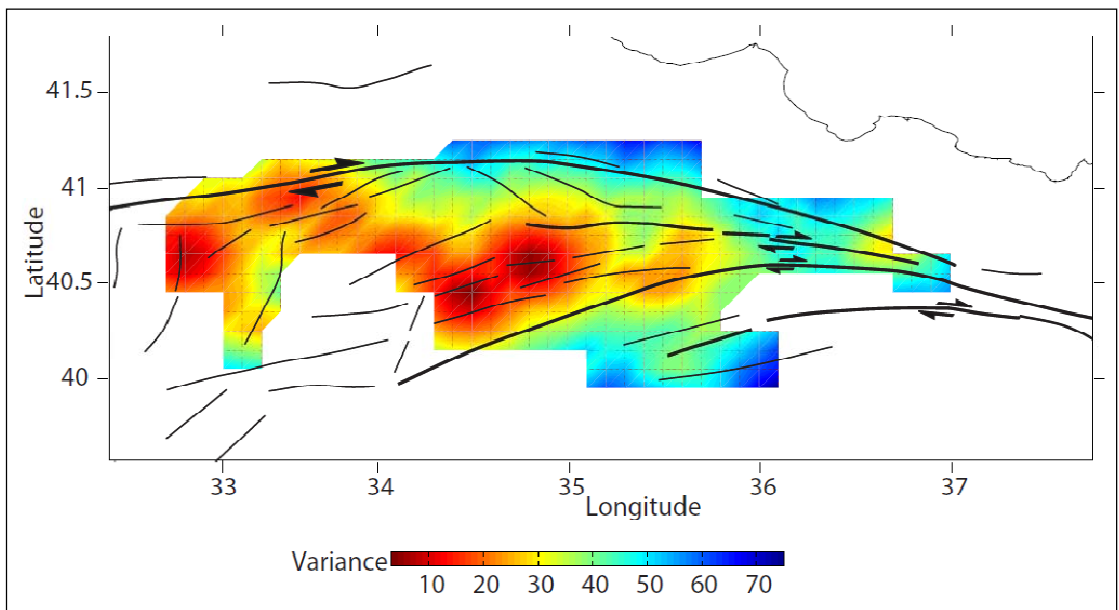
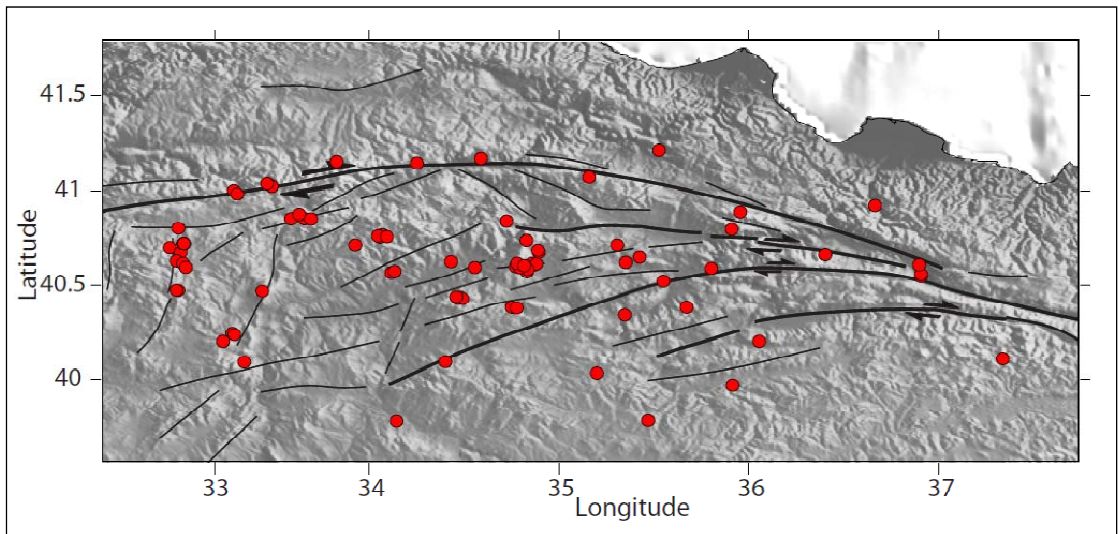


Figure 41. (a) Locations of 109 earthquakes and (b) resulting earthquake resolution over a 0.1x0.1 degree grid spacing.

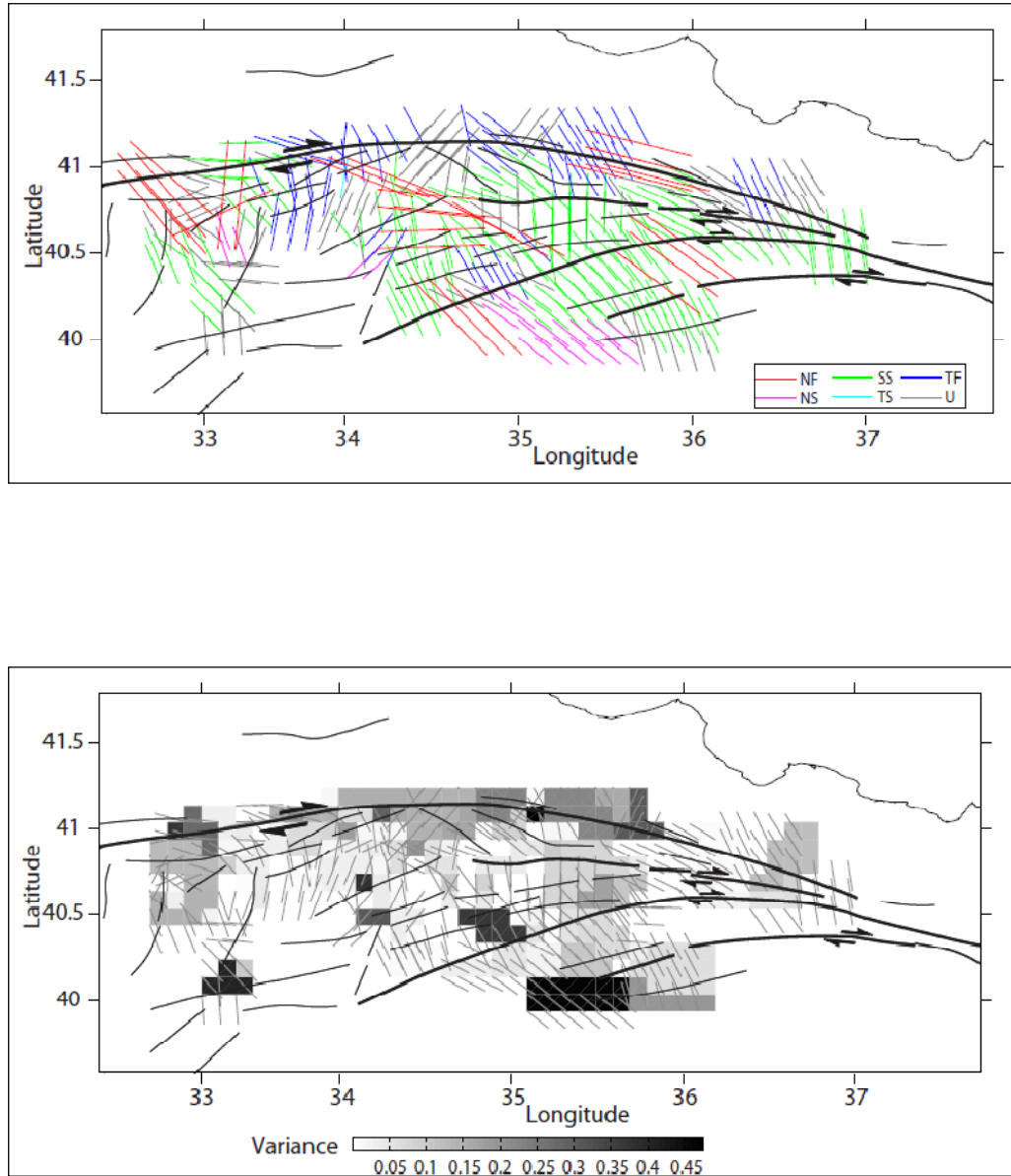


Figure 42. Orientation of the trend of σ_1 (bars) showing, (a) faulting types (b) variance of the stress tensor at each node, for 109 focal mechanisms determined in this study. Gridding parameters are: 0.1x0.1 degree spacing and constant number of events at each node is 3. Faulting regimes are represented by different colors as shown in the legend. Gray lines define the earthquakes that can not be classified.

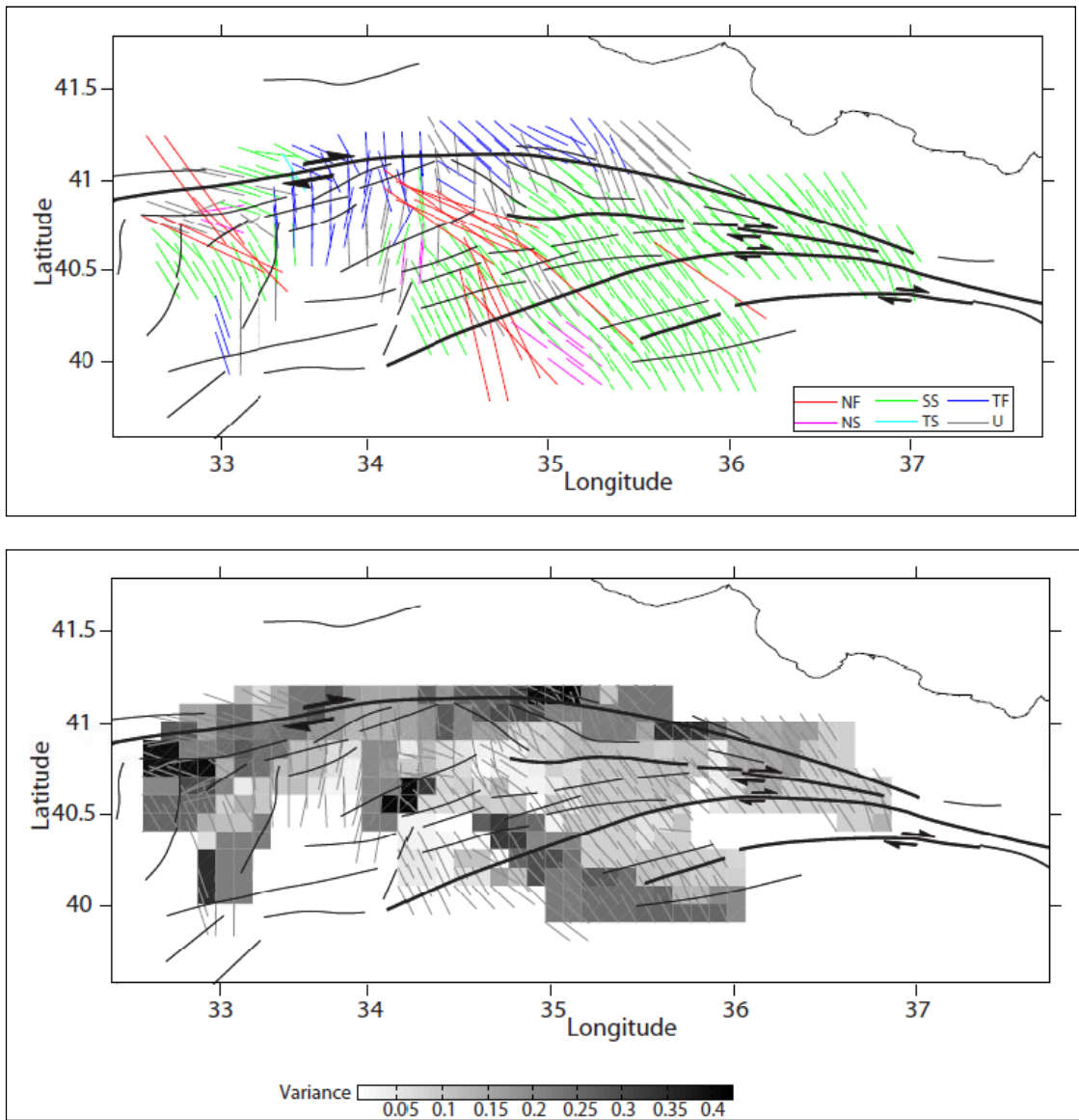


Figure 43. Orientation of the trend of σ_1 (bars) showing, (a) faulting types (b) variance of the stress tensor at each node, for 109 focal mechanisms determined in this study. Gridding parameters are: 0.1x0.1 degree spacing and constant number of events at each node is 5.

In Figure 43(a), fault classes of same grid spacing with 5 number of events, clearly shows the change of faulting types throughout the region. In the western and Çorum clusters, diversity of faulting types is not surprising, since same differences are also observed in the focal mechanisms solutions. Eastern part is controlled by splay of the NAF, shows consistent faulting types. Note the thrust faulting in the northern part of the main strand of NAF.

In order to understand the stress regime of the entire region better, our data set is improved with the available focal mechanism solutions determined for the study area (Table A. 1). Ternary plot of all these mechanisms are shown in Figure 44, with dominant strike-slip mechanisms. Nearly same stress orientations are obtained with the improved data set (Figure 45), with relatively more homogenous variance (0.17).

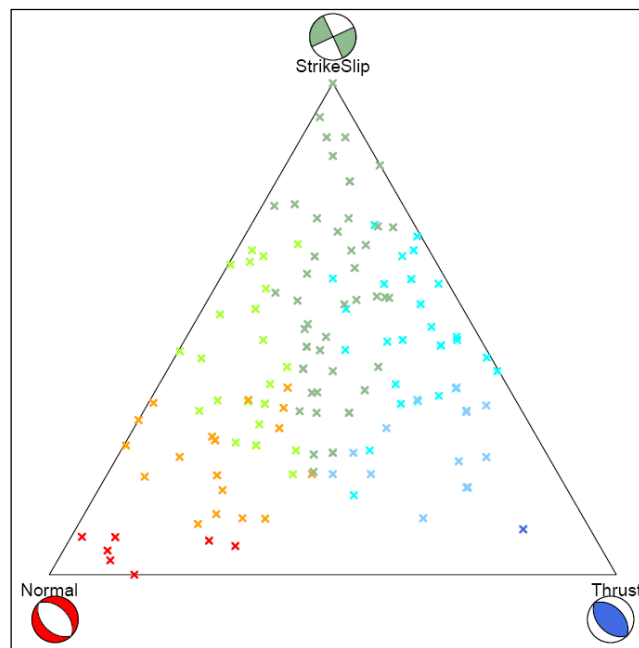


Figure 44. Ternary diagram of all focal mechanisms located in the study area.

Additional data improved the resolution of earthquake distribution (Figure 46) and increased the boundaries to NW and SW. Faulting types and variance calculated by using 0.1 km spacing and 3 number of events, reflects diversity in faulting types (Figure 47). Especially in the southern block, normal faulting is observed along with strike-slips. However, in the western part of the main strand of the NAF, presence of thrust faults can be visualized more clearly. Although stress orientations change across the region, general trend is consistent with the right-lateral slip of NAF and its splays. Higher variances (black color) mostly occur in the areas where earthquake resolution is lesser. Likewise, plots obtained by grid spacing 0.1 km and 5 number of event, express strike-slip mechanism is dominant in the area, with NW-SE σ_1 orientations (Figure 48). Southern block is more complex when different fault classes and σ_1 orientations are considered. Undefined fault types exist generally in the areas where variance is high and/or earthquake resolution is low.

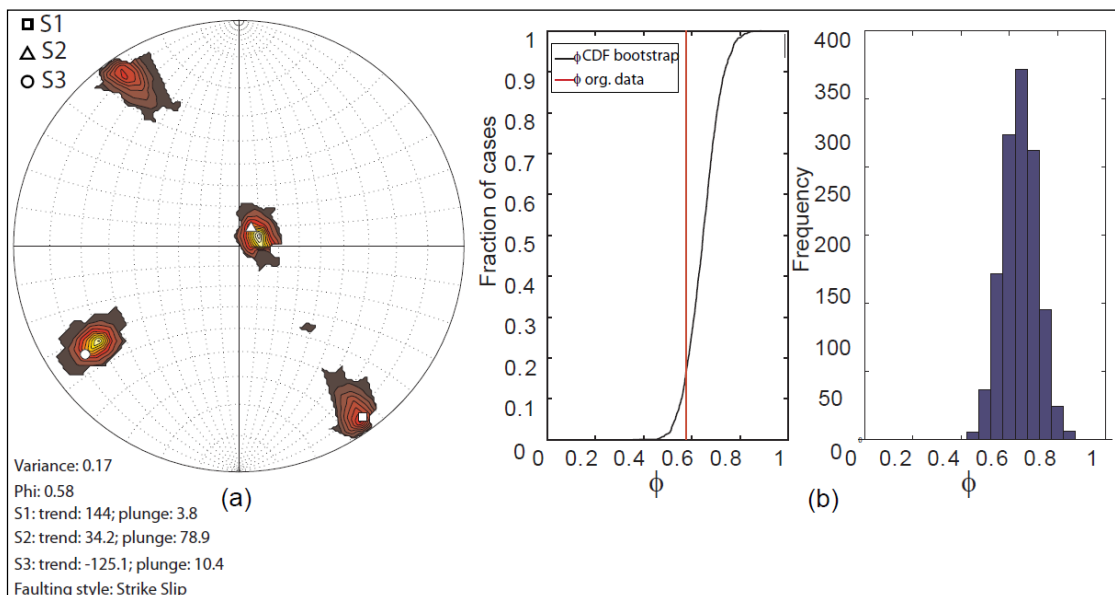


Figure 45. Stress inversion (a) and histogram of Φ values versus frequency (b) results of all focal mechanisms located in the study area, by Micheal's method.

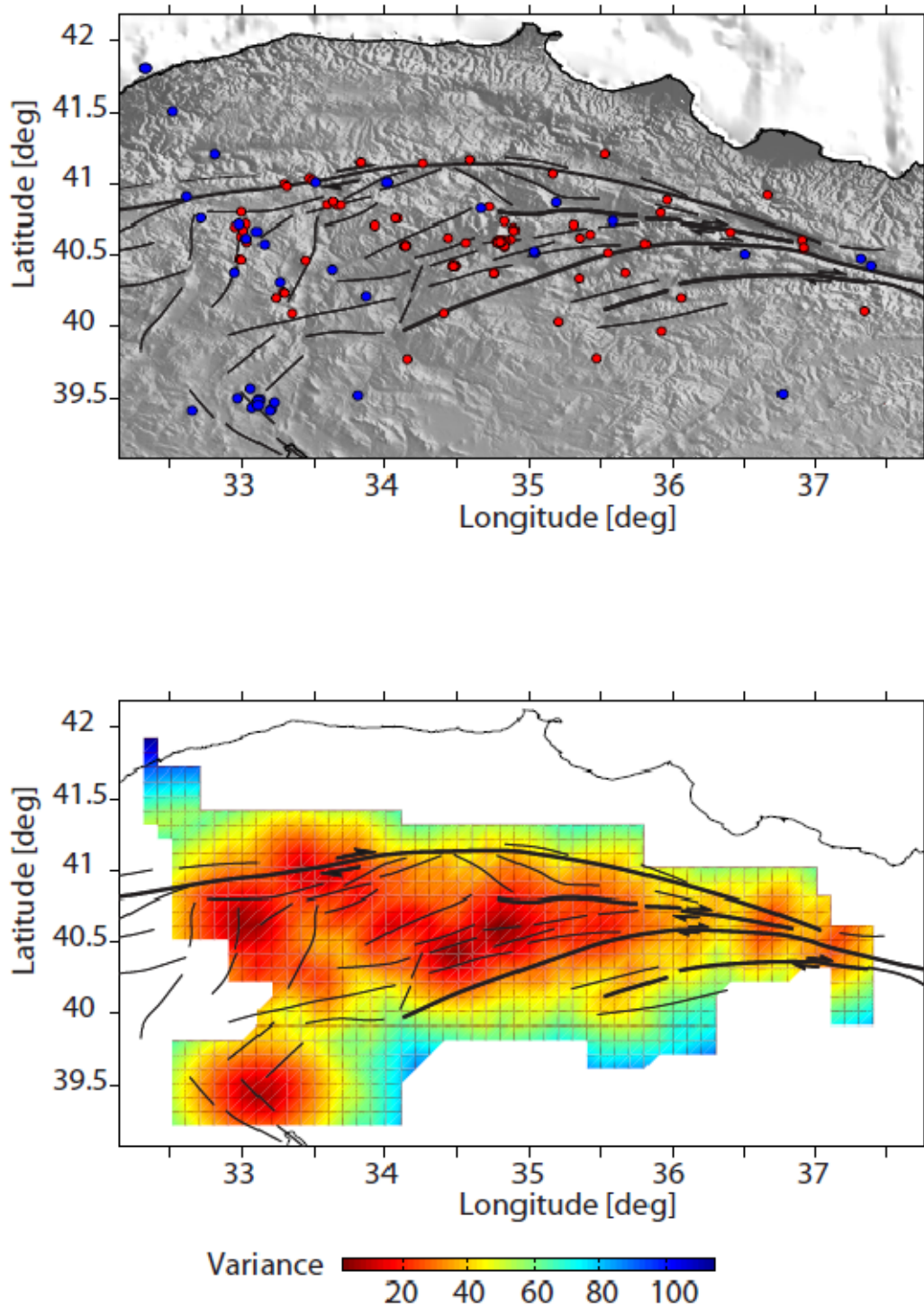


Figure 46. (a) Locations of all focal mechanisms located in the study (Red and blue circles are locations of focal mechanisms calculated in this study and taken from available catalogs, respectively) area and (b) resulting earthquake resolution over a 0.1x0.1 degree grid spacing.

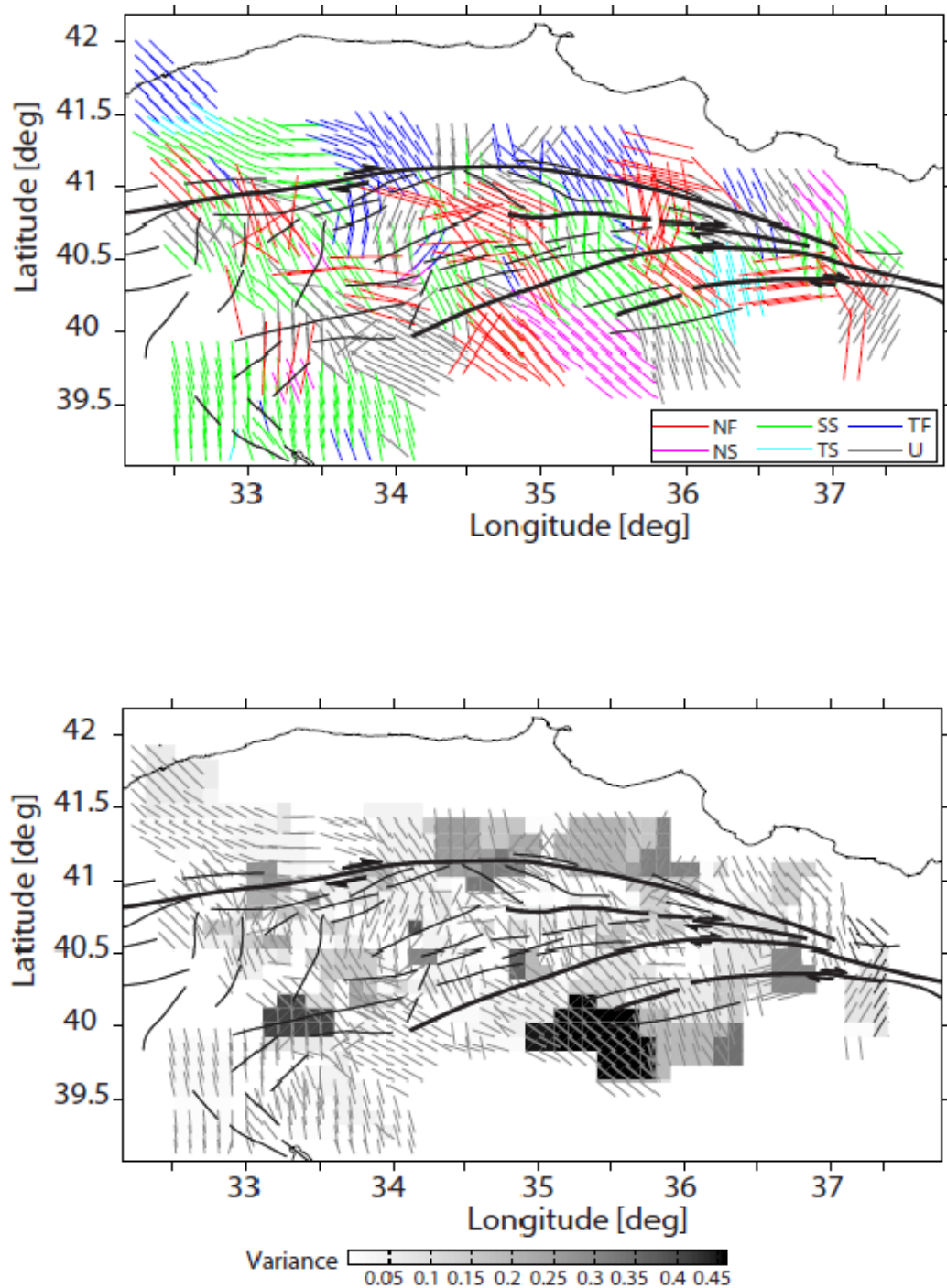


Figure 47. Orientation of the trend of σ_1 (bars) showing, (a) faulting types (b) variance of the stress tensor at each node, for all focal mechanisms located in the study area. Gridding parameters are: 0.1x0.1 degree spacing and constant number of events at each node is 3.

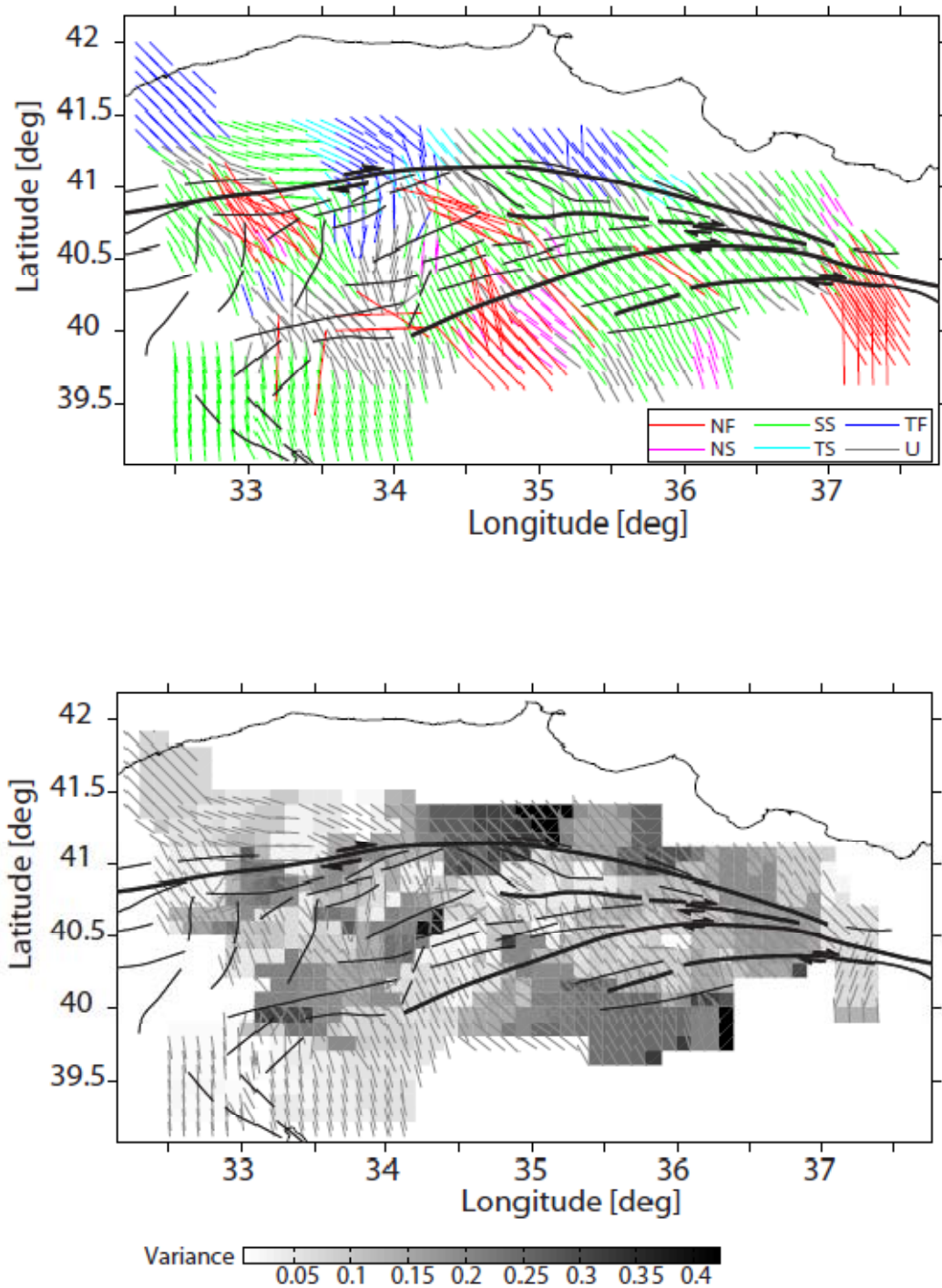


Figure 48. Orientation of the trend of σ_1 (bars) showing, (a) faulting types (b) variance of the stress tensor at each node, for all focal mechanisms located in the study area. Gridding parameters are: 0.1x0.1 degree spacing and constant number of events at each node is 5.

4.3.1. Çorum Cluster

Figure 49 shows the major cluster occurred along the central part of the region, located nearby Çorum. This cluster includes the second big event present in our data set (Eq. No: 2, M= 4.5). This earthquake is followed by many aftershocks and our recordings provided a good seismic record to solve these earthquake mechanisms. In Figure 49a important geological features together with earthquake epicenters are shown and in Figure 49b focal mechanisms are given. Red mechanisms are related to the main cluster trending nearly ENE-WSW. Fault responsible for this cluster displays approximately parallel trend to the splays of NAF. Although, this cluster reflects various types of mechanisms, dominant mechanism is noticed as approximately E-W-trending right-lateral strike-slip. All solutions with high magnitude (Eq. No: 2, 3, 5 6, 8, 9) show same type of mechanisms. Normal and thrust mechanisms are also developed as secondary mechanisms, which is normal in a strike-slip environment. Apart from the cluster, there are relatively smaller groups of earthquake localizations, displaying mostly strike-slip and normal mechanisms.

The corresponding *P*- and *T*- plots on lower hemisphere projections for the zoom-in area (69 events) and Çorum cluster (32 events) is shown in Figure 50. Zoom-in orientations show a more scattered orientation, with tectonic alignment of NW-SE compression and NE-SW dilation (Figure 50a). *P*- *T*- orientations of Çorum cluster display same direction (Figure 50b).

Same consistent results are obtained from stress inversion of both for zoom-in and Çorum cluster. Orientations of principal axes are nearly same. One important change is the variance value, which decreased significantly from zoom-in to Çorum cluster. This decrease states that although Çorum cluster has these diversities in faulting types, relatively homogenous stress field is observed (Figures 51 and 52).

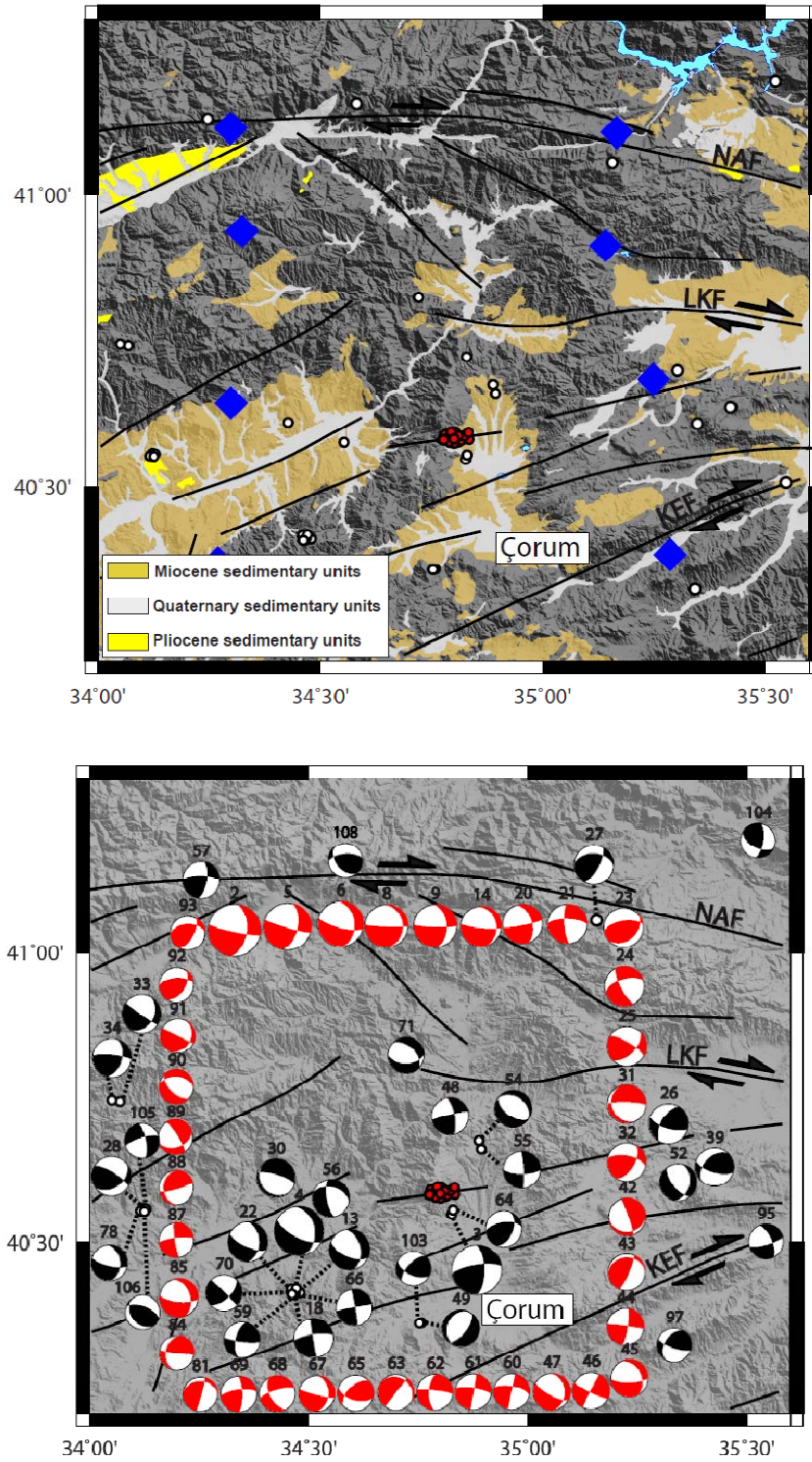


Figure 49. Close-up view showing (a) geology (MTA,2003) (b) focal mechanisms of the zoom-in area. Focal mechanism and locations shown in red color displays the Çorum cluster.

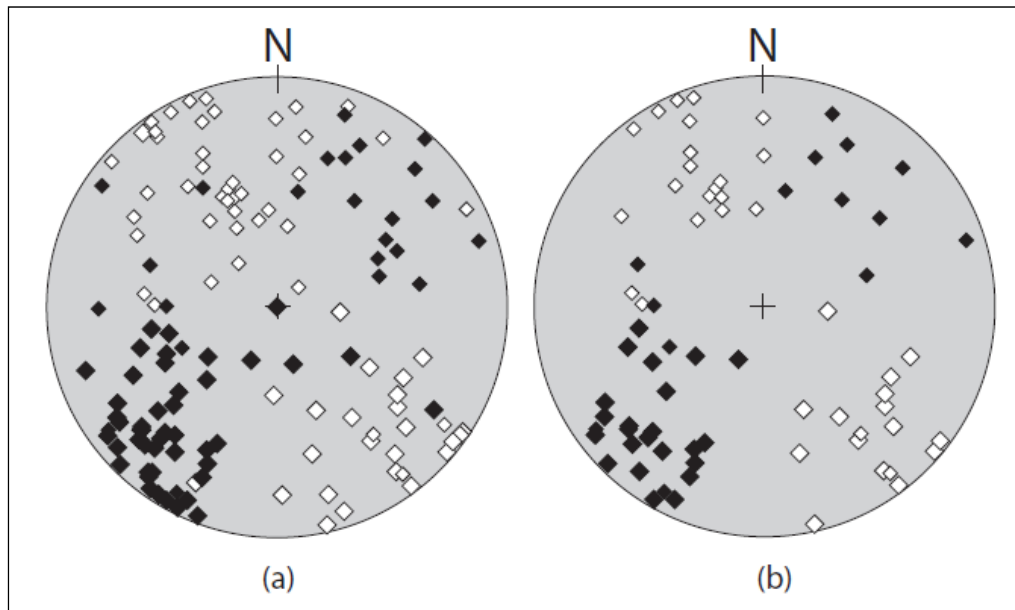


Figure 50. . Distribution of all P- T- axes orientations of (a) zoom-in and (b) Çorum cluster, shown in stereographic projection. Black diamonds show T- axes and white diamonds show P-axes.

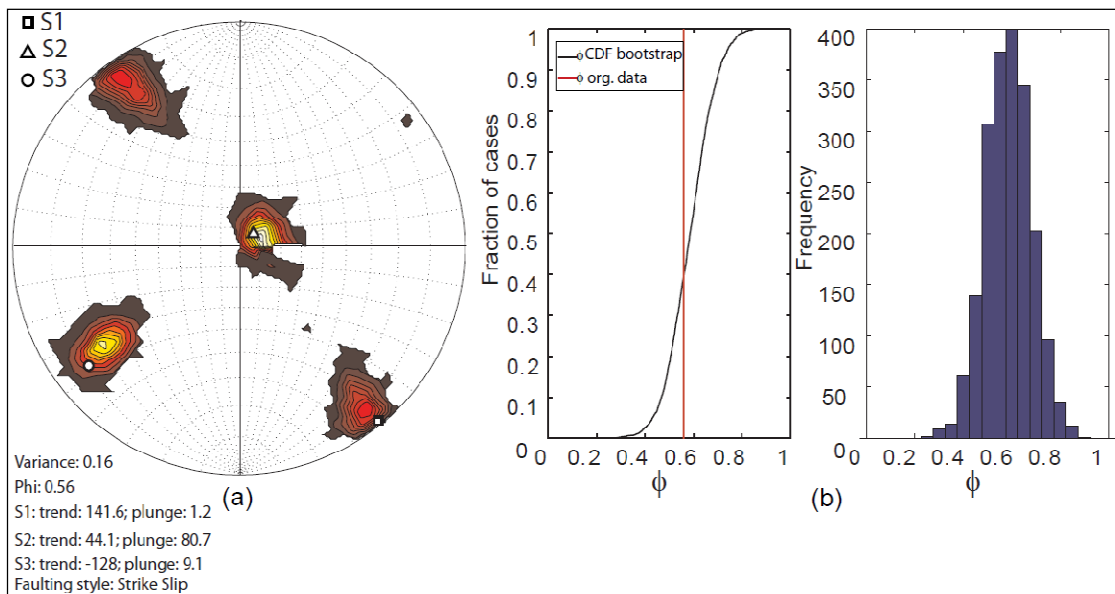


Figure 51. Stress inversion (a) and histogram of Φ values versus frequency (b) results of focal mechanisms located in the zoom-in area, by Micheal' s method.

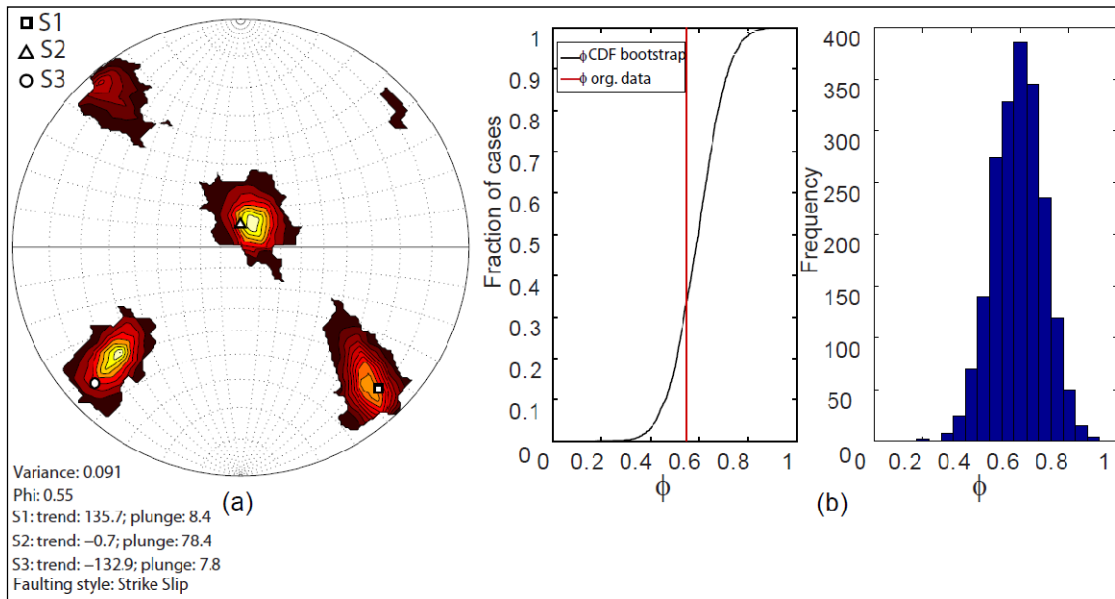


Figure 52. Stress inversion (a) and histogram of Φ values versus frequency (b) results of focal mechanisms located in the Çorum cluster, by Micheal's method.

CHAPTER 5

RESULTS AND DISCUSSION

Finally, horizontal stress orientations (SH) of all focal mechanisms present in the area are calculated; in Wintensor program (Delavux and Sperner, 2003). SH's usually expressed as SH_{max} in the World stress map (Bart et al., 2008), therefore orientations of SH_{max} data are plotted (Figure 53) using same color codes for faulting types. These results display similar faulting types, and general trends of SH_{max} and SH_{min} , showed in rose diagrams are NW-SE and NE-SW, respectively. All of our results are consistent with the tectonic regime and geology of the area when overall region is considered. Mainly strike-slip motions are observed, and principle stress orientations support the movement directions of these mechanisms.

In order to analyze the stress variations throughout the region, stress tensor calculation are obtained for 6 subgroups divided based on locality. Moreover, probable Riedel shear pattern of the area is given in inset of Figure 54.

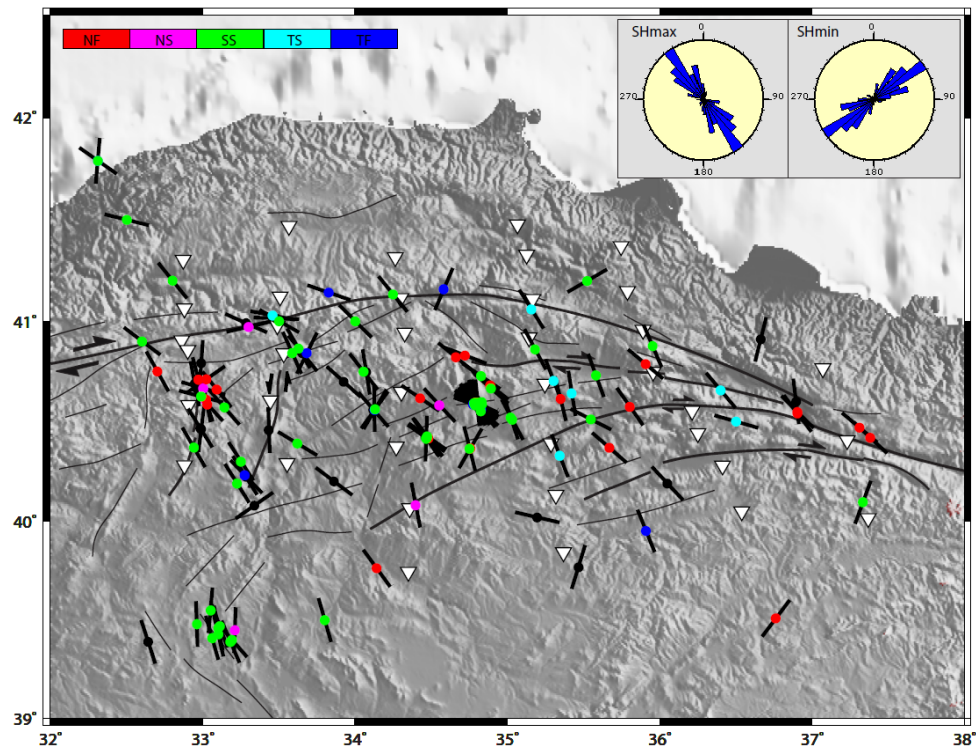


Figure 53. Focal mechanism data represented as SH_{max} axes. A color-coded central circle indicates the tectonic regime. Inset figures show the rose diagrams of SH_{max} and SH_{min} orientations.

First box includes the western part of the NAF's main strand. Here, right-lateral strike-slip mechanisms are observed along with major thrust faults. Thrusting in the area is a result of the σ_1 orientations, due to the change in the shape of NAF's geometry. One of the important feature seen here is an active branch of NAF (shown with blue arrow) which displays mainly right-lateral strike-slip motion.

Second box is located on the western part, where N-S trending faults exist (DFZ and EFZ). Our results suggest that, this area is seismically active and displays left-lateral movement. σ_1 orientations are approximately NNW-SSE trending and these zones can be referred as r' in the Riedel shear pattern.

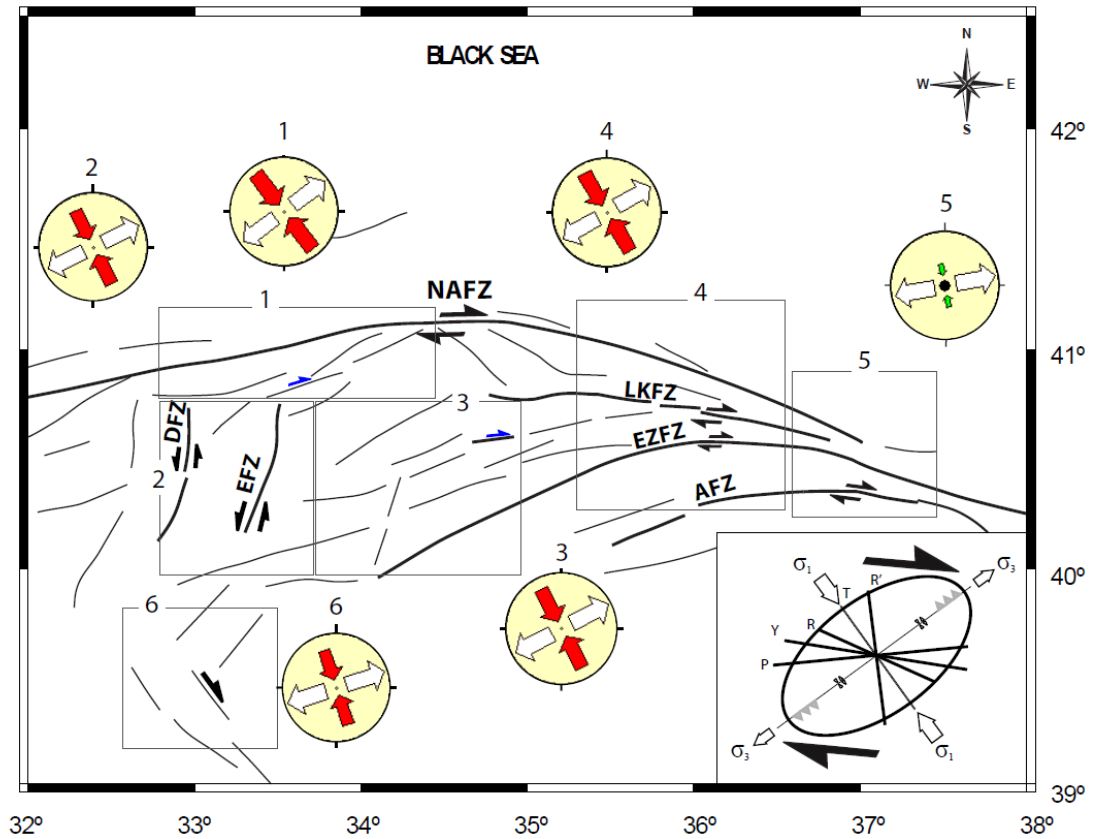


Figure 54. Simplified map of our results, subdivided into 6 groups. Stereonets refer to the stress orientations of related group. Blue arrows indicate the movement directions obtained from this study (size of the arrows are not to scale). Inset figure gives the general Riedel shear pattern of the region.

Third box has the most number of earthquakes, including the Çorum cluster. Focal mechanism data available from catalogs (RCMT, Harvard CMT, EMSC) solve only for two earthquakes in this area, and shows right-lateral strike-slip solutions. High station coverage of our study provided a good earthquake resolution. According to the results, diversity in faulting types exists, but mostly right-lateral strike-slip mechanisms are observed. Mechanisms related to Çorum cluster occur along approximately E-W-trending fault (shown in blue) and this fault is parallel to the main splays of NAF, displaying same type of motion. In a Riedel shear pattern, this fault can be constituted to

P-shears. Our results, apart from the Çorum cluster, indicate that, in this area faults should be oriented either E-W showing right lateral motion or N-S showing left-lateral motion. Normal mechanisms also present in the area that is usual in a strike-slip regime. σ_1 orientations are nearly NW-ES trending, however minor rotations occur due to northward bending of NAF. When previous seismicity is compared with our data, it is seen that seismic activity moved from east to this region.

Main splays of the NAF is included in forth box. This region is the most homogenous one when faulting types are considered. They show right-lateral strike-slips and stress orientation is consistent with the NAF's NW-SE trend. Regarding to the fault orientations, these splays can be referred to the p shears in the Riedel shear pattern.

Fifth box is located in the eastern part of the region where NAF and its main splays converge. In this region, due to the step-over structures, pull-apart basins are formed. Pull-aparts are mainly characterized by significant component of normal slip. Our solutions and stress orientation in this region are consistent with these extensional features.

Finally, sixth box covers the region of recent Bala earthquake. Although our station coverage does not cover this region, available focal mechanism data obtained from catalogs enabled us to perform provided a good earthquake resolution. Stress inversion of these data gives NNW-SSE orientation, which results in both strike-slip and normal mechanisms. This region plays an important role in order to understand the behavior of the stress changes, since it is located toward to Ankara region.

REFERENCES

- Adiyaman, Ö., Chorowicz, J., Arnaud, O., Gündogdu, M. and Gourgaud, A., 2001. Late Cenozoic tectonics and volcanism along the North Anatolian Fault: new structural and geochemical data. *Tectonophysics*, 338(2): 135-165.
- Anderson, M., Alvarado, P., Zandt, G. and Beck, S., 2007. Geometry and brittle deformation of the subducting Nazca Plate, Central Chile and Argentina. *Geophysical Journal International*, 171(1): 419-434.
- Barka, A.A. and Kadinsky-Cade, K., 1988. Strike-slip fault geometry in Turkey and its influence on earthquake activity. *Tectonics*, 7(3): 663-684.
- Barka, A.A. and Reilinger, R., 1997. Active tectonics of the Eastern Mediterranean region: deduced from GPS, neotectonic and seismicity data. *Annals of Geophysics*, 40(3): 587-610.
- Bayrak, Y., Öztürk, S., Koravos, G., Leventakis, G. and Tsapanos, T., 2008. Seismicity assessment for the different regions in and around Turkey based on instrumental data: Gumbel first asymptotic distribution and Gutenberg-Richter cumulative frequency law. *Natural Hazards and Earth System Science* 8: 109-122.
- Bozkurt, E., 1996. The Kazova basin: An active negative flower structure on the Almus fault zone, a splay fault system of the North Anatolian Fault Zone, Turkey. *Tectonophysics*, 265(3-4): 239-254.
- Bozkurt, E., 2001. Neotectonics of Turkey-a synthesis. *Geodinamica Acta*, 14(1-3): 3-

- Bozkurt, E. and Koçyiğit, A., 1995, Almus Fault Zone: its age, total offset and relation to the North Anatolian Fault Zone. *Turkish Journal of Earth Sciences*, 4: 93-104.
- Bozkurt, E. and Mittwede, S., 2001. Introduction to the geology of Turkey - a synthesis. *International Geology Review*, 43(7): 578-594.
- Çinku, M. C., Orbay, N., 2008. The Origin of Neogene Tectonic Rotations in the Galatean Volcanic Massif, Central Anatolia. *International Journal of Earth Sciences*, 99: 413-426.
- Delvaux, D. and Barth, A., 2010. African stress pattern from formal inversion of focal mechanism data. *Tectonophysics*, 482(1-4): 105-128.
- DeMets, C., Gordon, R., Argus, D. and Stein, S., 1990. Current plate motions. *Geophysical journal international*, 101(2): 425-478.
- Dziewonski, A., Ekström, G., Franzen, J. and Woodhouse, J., 1987a. Global seismicity of 1977: centroid-moment tensor solutions for 471 earthquakes. *Physics of the Earth and Planetary Interiors*, 45(1): 11-36.
- Dziewonski, A., Ekström, G., Franzen, J. and Woodhouse, J., 1987b. Global seismicity of 1978: centroid-moment tensor solutions for 512 earthquakes. *Physics of the Earth and Planetary Interiors*, 46(4): 316-342.
- Eyidoğan, H., Utku, Z., Güçlü, U., Değirmenci, E., 1991, A Macro-seismic Catalogue of the Main Earthquakes of Turkey (1900–1988), İstanbul Technical University, İstanbul, 199 pp. (in Turkish).
- Gephart, J. and Forsyth, D., 1984. An improved method for determining the regional

stress tensor using earthquake focal mechanism data: application to the San Fernando earthquake sequence. *Journal of Geophysical Research*, 89(B11): 9305-9320.

Goldstein, P., Dodge, D., Firpo, M. and Minner, L., 2003. SAC2000: signal processing and analysis tools for seismologists and engineers, in *The IASPEI International Handbook of Earthquake and Engineering Seismology*, edited by W. H. K. Lee et al., London: Academic Press.

Godey, S., Mazet-Roux, G., Bossu, R., Merrer S. and Guilbert, J., 2009, Ten Years of Seismicity in the Euro-Mediterranean Region: Panorama of the EMSC Bulletin 1998-2007.

Göncüoğlu, M. and Türeli, T., 1994. Alpine collisional-type granitoids from western Central Anatolian Crystalline Complex, Turkey. *Journal of Kocaeli University Earth Science*, 1: 39-46.

Görgün, E., Bohnhoff, M., Bulut, F. and Dresen, G., 2009. Seismotectonic setting of the Karadere-Düzce branch of the North Anatolian Fault Zone between the 1999 Izmit and Düzce ruptures from analysis of Izmit aftershock focal mechanisms. *Tectonophysics* 482(1-4), 170-181.

Görür, N. and Okay, A. İ., 1996. A fore-arc origin for the Thrace Basin, NW Turkey. *Geologische Rundschau*, 85(4): 662-668.

Gutenberg, B. and Richter, C., 1944. Frequency of earthquakes in California. *Bulletin of the Seismological Society of America*, 34(4): 185-188.

Hardebeck, J. and Hauksson, E., 2001. Stress orientations obtained from earthquake focal mechanisms: what are appropriate uncertainty estimates? *Bulletin of the*

Seismological Society of America, 91(2): 250-262.

Isseven, T. and Tüysüz, O., 2006. Palaeomagnetically defined rotations of fault-bounded continental blocks in the North Anatolian Shear Zone, North Central Anatolia. *Journal of Asian Earth Sciences*, 28(4-6): 469-479.

Kaymakci, N., 2000. Tectono-stratigraphical evolution of the Cankiri basin (Central Anatolia, Turkey). Phd. Thesis.

Kaymakci, N. Duermeijer, C. E., Langereis, C., White, S. H. and Vandijk, P. M., 2003. Palaeomagnetic evolution of the Cankiri Basin (central Anatolia, Turkey): implications for oroclinal bending due to indentation. *Geological Magazine*, 140(3): 343.

Kaymakci, N., Özmutlu, Vandijk, P. M., and Özçelik, Y., 2010. Surface and Subsurface Characteristics of the Çankırı Basin (Central Anatolia, Turkey): Integration of Remote Sensing, Seismic Interpretation and Gravity. *Turkish Journal of Earth Sciences*, 19: 79-100.

Ketin, I., 1957. Kuzey Anadolu deprem fayı. *ITU Dergisi*, 15: 49-52.

Kissling, E., Kradolfer, U. and Maurer, H., 1995. VELEST Version 3.1 User's guide-short introduction. Institute of Geophysics and Swiss Seismological Service, ETH, Zurich, 25 pp.

Koçyiğit, A., 1989. Susehri basin: an active fault-wedge basin on the North Anatolian Fault Zone, Turkey. *Tectonophysics*, 167(1): 13-29.

Koçyiğit, A., Rojay, B., Cihan, M. and Ozacar, A., 2001. The June 6, 2000, Orta (Çankır , Turkey) Earthquake: Sourced from a New Antithetic Sinistral Strike-slip

- Structure of the North Anatolian Fault System, the Dodurga Fault Zone. *Turkish Journal of Earth Sciences*, 10: 69-82.
- Lienert, B., Berg, E. and Frazer, L., 1986. Hypocenter: an earthquake location method using centered, scaled, and adaptively damped least squares. *Bulletin of the Seismological Society of America*, 76(3): 771-783.
- Lienert, B. and Havskov, J., 1994. HYPOCENTER 3.2-A computer program for locating earthquakes locally, regionally and globally. Hawaii Institute of Geophysics & Planetology, 70 pp.
- Michael, A., 1984. Determination of stress from slip data: faults and folds. *Journal of Geophysical Research*, 89(B13): 11517-11526.
- McClusky, S. et al., 2000. Global Positioning System constraints on plate kinematics and dynamics in the eastern Mediterranean and Caucasus, *Journal of Geophysical Research*, 105: 5695–5719.
- Moix, P. Beccaletto, L., Kozur, H. W., Hochard, C., Rosselet, F. and Stampfli, G. M., 2008. A new classification of the Turkish terranes and sutures and its implication for the paleotectonic history of the region. *Tectonophysics*, 451(1-4): 7-39.
- Okay, A. İ., Şengör, A.M.C. and Gorur, N., 1994. Kinematic history of the opening of the Black Sea and its effect on the surrounding regions. *Geology*, 22(3): 267-270.
- Okay, A. İ. and Tuysuz, O., 1999. Tethyan sutures of northern Turkey. *Geological Society London Special Publications*, 156(1): 475-515.
- Okay, A.İ. and Göncüoğlu, M., 2004. The Karakaya Complex: a review of data and concepts. *Turkish Journal of Earth Sciences*, 13(2): 77-95.

- Okay, A. İ., Satir, M. and Siebel, W., 2006. Pre-Alpide Palaeozoic and Mesozoic orogenic events in the Eastern Mediterranean region. In: D.G. Gee and R.A. Stephenson, Editors, *European Lithosphere Dynamics*, Geological Society, London, *Memoirs*, 32: 389–405.
- Oral, M., Reilinger R.E., Toksöz M.N., King R.W., Barka A.A., Kınık I. and Lenk O., 1995. Global positioning system offers evidence of plate motions in eastern Mediterranean. *Eos Trans*, AGU 76(2): 9-11.
- Pondrelli, S. et al., 2002. European-Mediterranean regional centroid-moment tensors: 1997-2000. *Physics of the Earth and Planetary Interiors*, 130(1-2): 71-101.
- Pondrelli, S., Morelli, A. and Ekström, G., 2004. European-Mediterranean regional centroid-moment tensor catalog: solutions for years 2001 and 2002. *Physics of the Earth and Planetary Interiors*, 145(1-4): 127-147.
- Pondrelli, S., Salimbeni, S., Morelli, A., Ekström, G. and Boschi, E., 2007. European-Mediterranean Regional Centroid Moment Tensor catalog: Solutions for years 2003 and 2004. *Physics of the Earth and Planetary Interiors*, 164(1-2): 90-112.
- Provost, A., Chéry, J. and Hassani, R., 2003. 3D mechanical modeling of the GPS velocity field along the North Anatolian fault. *Earth and Planetary Science Letters*, 209(3-4): 361-377.
- Reilinger, R. et al., 1997. Global Positioning System measurements of present-day crustal movements in the Arabia-Africa-Eurasia plate collision zone. *Journal of Geophysical Research*, 102(B5): 9983-9999.
- Robertson, A. and Ustaömer, T., 2004. Tectonic evolution of the Intra-Pontide suture

- zone in the Armutlu Peninsula, NW Turkey. *Tectonophysics*, 381(1-4): 175-209.
- Sanchez, J., McNutt, S., Power, J. and Wyss, M., 2004. Spatial variations in the frequency-magnitude distribution of earthquakes at Mount Pinatubo volcano. *Bulletin of the Seismological Society of America*, 94(2): 430-438.
- Snoke, J.A., 2003. FOCMEC : FOCal MECHANism Determinations in *International Handbook of Earthquake and Engineering Seismology*, edited by W. H. K. Lee et al., chap. 85.12, Academic, San Diego, Calif.
- Stein, S. and Wysession, M., 2003. *An introduction to seismology, earthquakes, and earth structure*. Oxford: Blackwell.
- Şengör, A. M. C., 1979. The North Anatolian transform fault: its age, offset and tectonic significance. *Journal of Geological Society*, 136(3): 269-282.
- Şengör, A. M. C. and Yilmaz, Y., 1981. Tethyan evolution of Turkey: a plate tectonic approach. *Tectonophysics*, 75(3-4): 181-190.
- Şengör, A. M. C., Tüysüz, O., İmren, C., Sakıncı, M., Eyidoğan, H., Görür, N., Pichon, X. L. and Rangin, C., 2005. The North Anatolian fault: a new look. *Annu. Rev. Earth Planet. Sci*, 33: 37-112.
- Tan, O., Tapırdamaz, M. C., Ergintav, S., İnan, S., İravul, Y., Saatçılar, R., Tüzel, B., Tarancıoğlu, A., Karakısa, S., Kartal, R. F., Zünbül, S., Yanık, K., Kaplan, M., Şaroğlu, F., Koçyiğit, A., Altunel, E. and Özel, N. M., 2009. Bala (Ankara) Earthquakes: Implications for Shallow Crustal Deformation in Central Anatolian Section of the Anatolian Platelet (Turkey). *Turkish Journal of Earth Sciences*, 19: 1-23.

- Tatar, O., Piper, J., Park, R. and Gürsoy, H., 1995. Palaeomagnetic study of block rotations in the Niksar overlap region of the North Anatolian Fault Zone, central Turkey. *Tectonophysics*, 244(4): 251-266.
- Tatar, O., Yurtmen, S., Temiz, H., Gürsoy, H., Kocbulut, F., Mescil, B., and Guezou, J., 2007. Intracontinental Quaternary Volcanism in the Niksar Pull-Apart Basin, North Anatolian Fault Zone, Turkey. *Turkish Journal of Earth Sciences*, 16: 417-440.
- Tauxe, L., Kylastra, N. and Constable, C., 1991. Bootstrap statistics for paleomagnetic data. *Journal of Geophysical Research*, 96(B7): 11,723-11,740.
- Taymaz, T., Wright, T., Yolsal, S., Tan, O., Fiedling, E., and Seyitoglu, G., 2007. Source characteristics of the 6 June 2000 Orta Cankiri (central Turkey) earthquake: a synthesis of seismological, geological and geodetic (InSAR) observations, and internal deformation of the Anatolian plate. *Geological Society London Special Publications*, 291(1): 259-290.
- Tselentis, G., 2006. Seismicity and seismotectonics in Epirus, Western Greece: Results from a microearthquake survey. *Bulletin of the Seismological Society of America*, 96(5): 1706-1717.
- Walsh, D., Arnold, R. and Townend, J., 2008. A Bayesian approach to determining and parameterising earthquake focal mechanisms. *Geophysical Journal International*, 176(1): 235-255.
- Watson, G., 1966. The statistics of orientation data. *The Journal of Geology*, 74(5): 786-797.

- Wiemer, S., Gerstenberger, M. and Hauksson, E., 2002. Properties of the aftershock sequence of the 1999 Mw 7.1 Hector Mine earthquake: Implications for aftershock hazard. *Bulletin of the Seismological Society of America*, 92(4): 1227-1240.
- Wong, H., Lüdmann, T., Ulug, A. and Görür, N., 1995. The Sea of Marmara: a plate boundary sea in an escape tectonic regime. *Tectonophysics*, 244(4): 231-250.
- Wiemer, S., 2001. A software package to analyze seismicity: ZMAP. *Seismol. Res. Lett.*, 72 (2), 374–383.
- Yavasoglu, H, Tari, E., Karaman, H., Şahin, M., Baykal, O., Erden, T., Bilgi, S., Rüzgar, G., İnce, C. D. and Ergintav, S., 2006. GPS Measurements along the North Anatolian Fault Zone on the Mid-Anatolia Segment. *Geodetic Deformation Monitoring: From Geophysical to Engineering Roles*: 131: 166-171.
- Yilmaz, Y., 1995. Geological evolution of the late Mesozoic continental margin of Northwestern Anatolia. *Tectonophysics*, 243(1-2): 155-171.
- Yilmaz, H., Özel, S. and Sivas, T., 2008. Crustal Structure of the Eastern Part of Central Anatolia (Turkey). *Turkish Journal of Earth Sciences*, 17: 169-185.
- Zoback, M., 1992. First-and second-order patterns of stress in the lithosphere: the world stress map project. *Journal of Geophysical Research*, 97(B8): 11703-11728.

APPENDIX A

Table A. 1 Parameters and sources for fault plane solutions of earthquakes that occurred in the study area.

No	Date	Time	Lon. E (°)	Lat. N (°)	Mag.	Dep. (km)	Strike (°)	Dip (°)	Rake (°)	Ref.
1	19.04.1938	10:59	33.8	39.5	6.5	0	298	87	149	EMSC
2	20.12.1942	14:03	36.5	40.5	7.2	0	344	56	41	EMSC
3	26.11.1943	22:20	34	41	6.2	0	1	82	16	EMSC
4	01.02.1944	03:22	32.5	41.5	6.2	0	332	79	26	EMSC
5	13.08.1951	18:33	32.6	40.9	6.4	0	262	85	-179	EMSC
6	27.09.1953	03:58	32.8	41.2	6.1	0	183	69	-18	EMSC
7	10.12.1966	17:08	33.5	41	4.9	13	165	90	0	EMSC
8	03.09.1968	08:18	32.31	41.79	5.7	5	28	37	79	EMSC
9	03.09.1968	08:19	32.31	41.79	6.1	5	315	66	156	EMSC
10	05.10.1977	05:34	33.62	40.39	5.8	16.1	166	83	0	Harvard
11	14.08.1996	01:55	35.02	40.52	5.7	15	116	70	176	Harvard
12	14.08.1996	02:59	35.18	40.86	5.6	15	197	69	-4	Harvard
13	28.02.1997	00:03	35.58	40.73	5.2	10	112	62	167	RCMT
14	11.06.1999	05:24	36.76	39.51	4.9	19	67	45	-39	RCMT
15	24.08.1999	17:33	32.64	39.39	4.9	10	27	53	-2	RCMT
16	06.06.2000	02:41	32.7	40.75	6	15	356	39	-47	Harvard
17	08.06.2000	21:27	33.02	40.61	4.8	22	353	40	-85	RCMT
18	09.06.2000	03:14	32.97	40.71	4.9	10	325	32	-125	RCMT
19	22.03.2001	14:02	33.09	40.66	4.7	33	151	29	-73	RCMT
20	12.08.2001	18:31	33.86	40.2	4.4	10	349	40	-8	RCMT
21	29.12.2004	22:22	32.94	40.37	4.5	5	17	74	12	RCMT
22	29.04.2005	22:28	34.66	40.82	4.8	18.7	155	51	-52	Harvard
23	12.05.2005	09:00	37.38	40.42	4.8	10	308	44	-97	RCMT
24	12.05.2005	09:25	37.31	40.47	4.8	15.8	132	39	-87	Harvard
25	30.07.2005	21:45	33.1	39.46	5.2	14.4	214	87	-2	Harvard
26	31.07.2005	00:45	33.19	39.4	4.3	10	8	62	14	RCMT
27	31.07.2005	23:41	33.11	39.47	4.8	10	205	73	1	RCMT
28	01.08.2005	00:45	33.06	39.41	4.7	7	119	82	172	RCMT
29	06.08.2005	09:09	33.18	39.39	4.7	10	111	74	171	RCMT
30	09.08.2005	01:28	33.14	40.57	4.7	15	276	55	-172	RCMT
31	20.12.2007	09:48	33.1	39.43	5.7	12	214	73	17	Harvard
32	26.12.2007	23:47	33.05	39.55	5.6	15	231	67	5	Harvard
33	27.12.2007	13:48	33.21	39.45	4.7	13	150	57	-140	RCMT
34	31.01.2008	00:01	33.25	40.3	4.9	17.1	193	77	13	Harvard
35	15.03.2008	10:15	32.96	39.48	4.8	10	41	66	-6	RCMT
36	02.04.2010	07:37	35.03	40.51	4.5	2	195	77	-11	RCMT

Table A. 2. P- T-, SHmax, SHmin axes and stress regimes of the focal mechanism data given in table A.1. NF = normal faulting, NS = predominately normal faulting with strike-slip component, SS = strike-slip faulting, TS = predominately thrust faulting with strike-slip component, TF = thrust faulting, UF = undefined.

No	Date	Time	Lon. E (°)	Lat. N (°)	P plu.	P azim.	T plu.	T azim.	SH max Azim.	Sh min Azim.	Regime Code
1	19.04.1938	10:59	33.8	39.5	19	348	24	249	164	74	SS
2	20.12.1942	14:03	36.5	40.5	1	286	51	195	106	16	TS
3	26.11.1943	22:20	34	41	6	134	17	226	135	45	SS
4	01.02.1944	03:22	32.5	41.5	9	102	26	197	104	14	SS
5	13.08.1951	18:33	32.6	40.9	4	127	3	217	127	37	SS
6	27.09.1953	03:58	32.8	41.2	27	142	3	51	141	51	SS
7	10.12.1966	17:08	33.5	41	0	300	1	30	120	30	SS
8	03.09.1968	08:18	32.31	41.79	9	306	79	165	125	35	TF
9	03.09.1968	08:19	32.31	41.79	1	185	33	275	5	95	SS
10	05.10.1977	05:34	33.62	40.39	4	121	6	31	121	31	SS
11	14.08.1996	01:55	35.02	40.52	11	340	17	73	162	72	SS
12	14.08.1996	02:59	35.18	40.86	18	154	12	61	152	62	SS
13	28.02.1997	00:03	35.58	40.73	11	337	28	73	160	70	SS
14	11.06.1999	05:24	36.76	39.51	54	49	11	303	37	127	NF
15	24.08.1999	17:33	32.64	39.39	27	349	24	246	162	72	UF
16	06.06.2000	02:41	32.7	40.75	61	351	13	236	151	61	NF
17	08.06.2000	21:27	33.02	40.61	85	45	5	259	169	79	NF
18	09.06.2000	03:14	32.97	40.71	65	130	17	260	165	75	NF
19	22.03.2001	14:02	33.09	40.66	72	202	17	49	141	51	NF
20	12.08.2001	18:31	33.86	40.2	37	320	29	206	127	37	UF
21	29.12.2004	22:22	32.94	40.37	3	331	20	240	150	60	SS
22	29.04.2005	22:28	34.66	40.82	62	130	1	39	129	39	NF
23	12.05.2005	09:00	37.38	40.42	89	122	1	223	133	43	NF
24	12.05.2005	09:25	37.31	40.47	84	202	6	40	130	40	NF
25	30.07.2005	21:45	33.1	39.46	4	169	1	79	169	79	SS
26	31.07.2005	00:45	33.19	39.4	11	322	29	226	139	49	SS
27	31.07.2005	23:41	33.11	39.47	11	161	13	69	160	70	SS
28	01.08.2005	00:45	33.06	39.41	0	164	11	74	164	74	SS
29	06.08.2005	09:09	33.18	39.39	5	336	18	68	157	67	SS
30	09.08.2005	01:28	33.14	40.57	29	133	19	234	139	49	SS
31	20.12.2007	09:48	33.1	39.43	1	167	24	76	167	77	SS
32	26.12.2007	23:47	33.05	39.55	12	187	20	93	5	95	SS
33	27.12.2007	13:48	33.21	39.45	50	2	0	92	2	92	NS
34	31.01.2008	00:01	33.25	40.3	0	327	19	57	147	57	SS
35	15.03.2008	10:15	32.96	39.48	20	360	13	265	178	88	SS
36	02.04.2010	07:37	35.03	40.51	17	152	1	61	152	62	SS

Table A. 3. Station information.

NAME	LATITUDE N (°)	LONGITUDE E (°)	ELEVATION (m)
ALIC	40.978	33.487	1471
ALIN	41.061	32.879	1133
ALOR	41.301	32.87	1045
ARSL	40.955	35.887	1015
BAGB	40.278	36.41	977
BEDI	41.121	33.506	1606
BEKI	41.315	34.263	1415
BOKE	40.552	36.211	1210
CAKM	40.015	37.367	1515
CALT	41.328	35.125	315
CAYA	40.373	34.269	754
CRLU	40.064	34.357	950
CUKU	40.604	33.441	1147
DERE	41.477	35.064	500
DOGL	40.391	35.284	722
DUMA	40.918	35.14	997
EKIN	41.147	35.787	835
GOCE	39.743	34.348	792
HASA	41.469	33.565	905
INCE	40.581	32.906	1100
INSU	39.842	35.366	1257
ISKE	40.764	37.067	1289
KARA	40.688	35.245	1162
KARG	40.291	33.552	863
KAVA	40.28	32.878	1154
KGAC	40.941	34.323	1512
KIYI	40.131	35.316	912
KIZIK	40.048	36.536	1185
KUYL	41.59	34.332	557
KUZA	40.441	36.248	1312
KUZO	40.904	32.861	1017
OGUR	41.109	35.165	655
PANC	40.647	34.301	872
PELI	41.113	34.299	1021
SEYH	40.856	32.9	1128
SYUN	40.838	33.529	1442
TEPE	41.369	35.743	162
YESI	40.405	37.229	629
YIKI	40.748	35.954	804

Table A. 4. Station correction values.

NAME	STATION DELAYS (sec)
ALIC	0.11
ALIN	0.34
ALOR	0.04
ARSL	-0.28
BAGB	0.46
BEDI	0.15
BEKI	-0.03
BOKE	-0.17
CAKM	0.19
CALT	0.07
CAYA	-0.02
CRLU	-0.12
CUKU	-0.3
DERE	0.24
DOGL	-0.09
DUMA	-0.15
EKIN	0
GOCE	-0.04
HASA	0.29
INCE	-0.19
INSU	0.53
ISKE	-0.21
KARA	0
KARG	-0.31
KAVA	0
KGAC	0
KIYI	-0.17
KIZIK	0.27
KUYL	-0.02
KUZA	-0.05
KUZO	0.09
OGUR	-0.07
PANC	0.07
PELI	0.01
SEYH	0.26
SYUN	-0.15
TEPE	-0.03
YESI	0.07
YIKI	-0.26

Table A. 5. Initial and final hypocenter locations.

DATE	INITIAL LOCATIONS				FINAL LOCATIONS			
	TIME	LAT. N (°)	LONG. E (°)	DEPTH (km)	TIME	LAT. N (°)	LONG. E (°)	DEP. (km)
31.01.2008	00:00:29.700	40.28	33.16	2	00:00:28.38	40.19	33.224	14.6
29.03.2008	03:11:40.415	40.6	34.68	6	03:11:38.94	40.59	34.802	11.9
14.01.2008	02:05:35.700	40.62	34.74	10	02:05:36.64	40.553	34.824	14.9
01.04.2008	00:40:49.215	40.43	34.4	6	00:40:48.01	40.418	34.479	8.4
02.04.2008	10:13:18.115	40.59	34.78	6	10:13:16.99	40.583	34.809	14.2
29.03.2008	03:26:54.815	40.61	34.77	6	03:26:53.67	40.591	34.795	14.3
14.02.2007	11:58:21.820	39.82	34.07	5	11:58:23.90	39.763	34.141	18.8
13.04.2008	02:48:17.615	40.57	34.77	12	02:48:17.60	40.592	34.789	14.1
31.03.2008	03:36:58.615	40.62	34.78	6	03:36:57.38	40.593	34.791	9.9
03.08.2007	09:03:11.315	41.09	35.1	5	09:03:10.80	41.097	35.146	11.2
17.06.2007	23:00:35.615	41.05	33.44	6	23:00:36.21	41.028	33.457	14.5
28.02.2007	16:04:18.520	40.51	33.01	5	16:04:19.45	40.467	32.981	10.4
04.10.2006	18:09:01.715	41.18	34.45	5	18:09:1.58	41.17	34.404	10
07.07.2006	01:20:19.515	40.75	33	5	01:20:18.33	40.689	32.946	25.3
05.04.2008	09:48:41.615	40.42	34.45	2	09:48:41.33	40.417	34.48	9.5
01.04.2008	14:01:28.515	40.6	34.83	6	14:01:28.45	40.588	34.797	12
24.09.2007	23:21:00.115	39.75	35.4	6	23:20:59.98	39.769	35.465	6.8
16.06.2007	17:35:36.205	40.15	37.23	7	17:35:34.11	40.096	37.332	24.9
17.11.2006	07:24:07.715	40.85	33.59	5	07:24:7.68	40.842	33.585	10.3
17.04.2008	17:35:24.015	40.43	34.47	10	17:35:24.62	40.416	34.466	10.9
14.04.2008	15:16:01.215	39.94	35.92	6	15:16:0.53	39.951	35.909	9.7
05.04.2008	02:11:36.015	40.6	34.78	8	02:11:35.35	40.594	34.804	12.5
02.04.2008	10:42:19.715	40.58	34.76	8	10:42:19.82	40.582	34.787	9.4
01.04.2008	05:52:14.715	40.44	34.48	6	05:52:14.34	40.424	34.461	1.7
31.03.2008	20:12:33.015	40.59	34.8	14	20:12:34.47	40.584	34.787	14.6
31.03.2008	18:39:29.315	40.6	34.8	6	18:39:28.09	40.586	34.801	12.1
29.03.2008	08:31:03.815	40.62	34.82	6	08:31:2.15	40.595	34.804	14.8
22.03.2008	03:45:02.815	40.72	35.28	2	03:45:1.50	40.703	35.302	13.5
26.11.2007	00:57:57.315	41.05	35.17	2	00:57:56.81	41.059	35.156	10.9
22.04.2007	01:58:13.220	40.55	34.08	13	01:58:14.29	40.563	34.124	15.1
17.01.2007	16:37:50.720	40.1	34.39	3	16:37:52.94	40.081	34.397	14.1
11.04.2008	15:09:17.115	40.6	34.4	8	15:09:18.09	40.616	34.427	18.9
08.04.2008	22:59:50.015	40	34.01	8	22:59:50.06	40.006	34.002	25.4
31.03.2008	05:26:55.815	40.6	34.84	6	05:26:55.87	40.585	34.8	10.3
31.03.2008	03:08:41.215	40.61	34.78	6	03:08:40.50	40.589	34.803	10
18.03.2008	18:23:40.115	40.73	34.09	17	18:23:42.04	40.747	34.072	15.4
15.03.2008	23:48:08.315	40.76	34.1	3	23:48:8.79	40.749	34.054	14.5
07.03.2008	10:34:22.515	40.46	33.03	6	10:34:23.02	40.462	32.989	17.8
22.02.2008	01:04:09.115	40.57	33.02	7	01:04:9.91	40.586	33.028	14.9
20.12.2007	16:14:52.615	40.21	36.03	4	16:14:51.60	40.19	36.049	9.9
22.11.2007	15:34:05.515	40.61	35.29	5	15:34:5.67	40.613	35.256	10.2
04.11.2007	15:46:13.115	40.04	37.34	5	15:46:8.27	39.943	37.423	6

continues →

07.10.2007	01:14:35.915	40.53	36.13	18	01:14:24.42	40.656	36.398	13.1
11.03.2007	06:41:51.920	40.25	33.38	9	06:41:52.20	40.266	33.403	18.7
10.03.2007	06:09:20.220	40.36	35.19	5	06:09:22.13	40.33	35.224	15.1
10.12.2006	20:10:39.615	40.65	35.39	18	20:10:40.45	40.641	35.421	14.8
05.12.2006	20:28:36.415	40.99	33.28	10	20:28:35.93	40.99	33.283	11.6
03.10.2006	01:56:40.915	40.73	33.07	5	01:56:39.99	40.661	32.986	14.4
19.07.2006	12:53:48.115	40.8	33.01	13	12:53:48.10	40.792	32.989	11.8
22.04.2008	11:32:43.915	40.61	34.83	6	11:32:43.37	40.585	34.814	14.1
11.04.2008	18:07:11.915	40.56	34.78	9	18:07:11.76	40.581	34.802	12.1
03.04.2008	07:16:24.515	40.55	34.77	7	07:16:24.31	40.58	34.798	14.9
01.04.2008	15:57:13.315	40.57	34.78	12	15:57:14.58	40.592	34.78	11.4
31.03.2008	15:10:23.215	40.57	34.8	14	15:10:23.44	40.591	34.79	11.2
31.03.2008	03:59:14.615	40.62	34.88	6	03:59:16.27	40.594	34.79	8.4
29.03.2008	21:58:57.715	40.59	34.88	20	21:58:59.59	40.591	34.789	6.6
29.03.2008	04:56:36.515	40.58	34.77	6	04:56:35.60	40.594	34.796	12
24.03.2008	19:18:24.015	40.05	35.66	4	19:18:26.42	40.038	35.722	4.2
14.02.2008	11:38:58.500	40.7	34.81	16	11:38:58.97	40.727	34.826	12.1
02.10.2007	11:11:10.115	40.36	34.6	7	11:11:6.51	40.366	34.756	5.7
29.09.2007	22:15:41.415	40.35	35.66	2	22:15:42.54	40.369	35.667	10.7
25.09.2007	08:16:01.615	41.09	34.59	7	08:16:0.88	41.129	34.578	9.4
17.08.2007	06:53:35.815	39.93	33.11	7	06:53:36.55	39.921	33.169	15
25.07.2007	16:45:07.315	40.71	33.03	2	16:45:8.86	40.711	33.021	13.3
24.06.2007	20:50:07.315	40.65	35.32	5	20:50:9.11	40.613	35.347	13.7
23.04.2007	17:00:57.720	40.88	36.01	11	17:00:57.03	40.876	35.951	12.5
11.02.2007	00:03:03.420	40.62	34.88	5	00:03:5.81	40.68	34.886	14
24.09.2006	21:09:35.215	40.66	34.87	5	21:09:35.72	40.665	34.891	12.5
13.08.2006	13:37:26.515	40.59	34.52	9	13:37:27.46	40.582	34.552	14.9
04.08.2006	11:15:28.315	41.14	34.25	5	11:15:29.38	41.133	34.247	7.4
19.04.2008	20:38:24.415	40.62	35.93	7	20:38:24.16	40.787	35.905	14.6
17.04.2008	18:11:46.115	40.45	34.45	10	18:11:45.96	40.419	34.469	3.7
11.04.2008	12:21:19.115	40.61	34.83	8	12:21:18.93	40.587	34.831	14.3
09.04.2008	20:30:43.515	40.58	34.81	11	20:30:43.56	40.593	34.82	11.7
09.04.2008	19:29:18.715	40.82	34.72	9	19:29:24.48	40.598	34.83	7.1
05.04.2008	18:01:24.815	40.56	34.9	6	18:01:26.46	40.592	34.796	11.2
03.04.2008	21:29:38.415	40.53	34.82	7	21:29:38.93	40.56	34.827	27.3
03.04.2008	15:19:23.615	40.59	34.82	12	15:19:24.65	40.599	34.8	12.8
02.04.2008	23:51:15.115	40.4	34.46	22	23:51:15.01	40.425	34.472	7.2
02.04.2008	00:02:43.815	40.54	34.79	11	00:02:43.79	40.595	34.777	6.8
01.04.2008	21:01:03.615	40.58	34.79	18	21:01:5.29	40.592	34.787	10.9
01.04.2008	18:58:02.215	40.58	34.81	10	18:58:2.86	40.594	34.793	10.6
01.04.2008	01:48:33.815	40.36	34.45	7	01:48:35.16	40.415	34.465	13
03.03.2008	23:43:50.615	40.85	34.75	6	23:43:51.19	40.829	34.72	12.6
05.02.2008	07:01:24.800	40.19	33.26	5	07:01:26.40	40.231	33.275	14.7
31.01.2008	02:47:46.300	40.22	33.26	7	02:47:46.71	40.224	33.284	23.3
22.01.2008	08:58:24.925	40.63	33.05	2	08:58:26.98	40.625	32.987	18.5
24.12.2007	07:56:50.615	40.7	32.99	2	07:56:52.67	40.712	33.037	13

continues →

23.11.2007	12:03:08.915	39.96	33.56	5	12:03:7.13	40.034	33.599	3.9
14.11.2007	12:52:33.915	40.59	35.87	7	12:52:36.53	40.574	35.803	8.8
23.10.2007	10:54:33.715	40.92	36.72	5	10:54:35.02	40.91	36.661	10.4
10.10.2007	22:06:29.715	40.6	36.99	2	22:06:30.61	40.541	36.902	4.5
15.09.2007	00:41:23.915	40.46	33.02	7	00:41:23.71	40.485	32.977	12.4
22.04.2007	04:38:09.920	40.55	34.14	12	04:38:11.71	40.559	34.118	12.6
12.01.2007	03:21:49.020	40.63	33.05	5	03:21:49.42	40.609	33.014	11.3
11.01.2007	02:38:22.820	40.85	35.85	5	02:38:25.78	40.893	35.936	10.6
15.12.2006	04:09:49.315	40.56	36.79	5	04:09:47.37	40.6	36.893	9.5
21.11.2006	12:22:37.715	41.37	33.69	8	12:22:37.25	41.429	33.681	4.4
22.04.2008	01:35:19.615	40.66	33.05	7	01:35:19.36	40.696	33.015	2
13.04.2008	01:16:35.915	40.55	34.85	6	01:16:37.29	40.59	34.799	14.5
10.04.2008	16:22:17.915	41.03	33.47	7	16:22:17.21	41.013	33.482	11.9
10.04.2008	07:01:18.615	40.7	33.05	2	07:01:19.25	40.62	33.03	11.8
07.04.2008	19:39:41.415	40.82	33.73	8	19:39:41.48	40.84	33.654	12.2
07.04.2008	17:43:15.815	40.56	34.75	5	17:43:18.98	40.593	34.808	14.4
05.04.2008	01:34:19.015	40.6	34.78	8	01:34:19.30	40.595	34.792	15
03.04.2008	01:05:22.615	40	35.19	7	01:05:22.71	40.019	35.194	10.6
02.04.2008	04:55:18.615	40.39	34.45	7	04:55:18.08	40.409	34.453	13.2
02.04.2008	00:05:58.015	40.57	34.8	13	00:05:58.80	40.591	34.789	10.3
01.04.2008	22:38:05.915	40.51	34.8	7	22:38:7.45	40.588	34.78	12
01.04.2008	22:04:49.515	40.58	34.78	18	22:04:52.43	40.586	34.773	2.1
01.04.2008	20:56:45.615	40.5	34.81	6	20:56:44.99	40.583	34.787	9.5
01.04.2008	00:57:30.115	40.54	34.85	7	00:57:31.96	40.595	34.792	14.4
31.03.2008	19:40:26.015	40.55	34.88	7	19:40:28.03	40.599	34.791	12.9
30.03.2008	12:16:50.715	40.64	34.81	10	12:16:52.50	40.586	34.774	5.4
29.03.2008	05:50:32.015	40.59	34.78	6	05:50:31.49	40.588	34.798	10.4
06.03.2008	10:18:09.715	40.45	36.06	7	10:18:7.72	40.5	36.058	12.8
14.02.2008	11:59:33.800	40.42	33.41	3	11:59:34.39	40.458	33.433	10.5
10.02.2008	15:21:09.200	40.48	35.52	7	15:21:8.86	40.511	35.546	12.9
16.01.2008	11:20:03.600	39.9	33.1	7	11:20:5.38	39.937	33.106	6.3
16.01.2008	03:30:18.100	39.78	34.02	15	03:30:20.57	39.867	34.067	9.8
13.12.2007	06:34:57.715	41.01	33.48	7	06:34:57.22	41.034	33.46	15.9
13.12.2007	06:30:28.415	41.02	33.48	3	06:30:27.93	41.034	33.458	15.8
12.12.2007	08:40:34.715	39.77	33.3	3	08:40:34.18	39.737	33.282	8.5
02.12.2007	23:09:22.615	40.69	34.82	4	23:09:20.30	40.698	34.879	13.7
21.11.2007	01:14:37.115	40.84	33.69	10	01:14:37.76	40.841	33.683	12.9
08.11.2007	10:40:06.415	39.98	33.54	7	10:40:8.13	39.968	33.523	11.3
27.10.2007	03:30:16.715	40.37	35.53	7	03:30:20.36	40.329	35.342	5.2
25.10.2007	08:03:16.915	40.71	33.04	5	08:03:18.98	40.681	33.012	14.3
23.10.2007	18:50:42.915	41.09	36.66	12	18:50:43.14	40.912	36.68	9.8
23.10.2007	13:53:54.615	41.43	33.5	7	13:53:52.95	41.427	33.401	9.6
14.10.2007	19:24:53.315	41.02	33.64	7	19:24:52.57	41.048	33.691	13.2
10.10.2007	22:52:21.015	40.6	36.98	5	22:52:21.54	40.548	36.903	6.5
10.10.2007	07:49:20.015	40.37	34.13	7	07:49:21.16	40.356	34.102	15.1
09.10.2007	13:53:59.515	40.06	33.32	10	13:54:0.90	40.079	33.337	9.2

continues →

03.10.2007	11:25:28.015	40.89	33.66	10	11:25:29.45	40.865	33.628	14.4
18.09.2007	08:43:27.815	41.56	33.79	7	08:43:25.18	41.615	33.75	8.5
18.09.2007	08:11:37.415	40.67	33.01	2	08:11:39.55	40.666	33.002	12.7
11.09.2007	10:12:58.715	39.93	33.53	7	10:13:1.21	39.991	33.562	15
06.09.2007	04:21:23.915	40.97	33.22	6	04:21:23.86	40.971	33.3	8.1
17.08.2007	11:49:50.215	40.34	34.71	8	11:49:49.77	40.365	34.751	4
25.04.2007	07:00:24.820	41.08	35.42	5	07:00:27.85	41.199	35.522	14.5
22.04.2007	03:54:53.320	40.49	34.09	6	03:54:54.38	40.562	34.13	15.1
09.03.2007	16:11:09.320	40.51	34.15	6	16:11:11.59	40.558	34.127	15
26.12.2006	17:24:39.515	41.1	33.84	5	17:24:41.74	41.141	33.826	8
10.12.2006	08:50:45.215	40.67	36.18	15	08:50:44.80	40.665	36.196	9
08.12.2006	01:06:16.515	41.18	34.55	14	01:06:17.27	41.159	34.58	11.8
25.09.2006	10:06:25.515	41.54	33.93	24	10:06:26.87	41.539	33.911	5.7
02.09.2006	23:17:37.915	40.17	33.39	3	23:17:38.98	40.196	33.383	12.7
22.08.2006	20:32:50.015	40.65	33.97	12	20:32:51.99	40.699	33.923	14.3
15.08.2006	23:24:31.615	40.04	34.65	8	23:24:32.08	40.038	34.693	10.9
07.07.2006	07:43:58.715	40.82	33.09	25	07:43:57.66	40.728	32.99	13.6

Table A. 6. Focal mechanism orientations of 109 earthquakes determined in this study.

No	Date	Time	Lat. N (°)	Long. E (°)	Mag.	Dep. (km)	Strike (°)	Dip (°)	Rake (°)
1	31.01.2008	00:00:28.38	40.19	33.224	4.9	14.6	15.6	75.97	20.91
2	29.03.2008	03:11:38.94	40.59	34.802	4.5	11.9	6.6	50.73	-8.29
3	14.01.2008	02:05:36.64	40.553	34.824	4.3	14.9	358.96	65.82	18.32
4	01.04.2008	00:40:48.01	40.418	34.479	4.2	8.4	349.57	34.78	-42.19
5	02.04.2008	10:13:16.99	40.583	34.809	4.1	14.2	12	55.61	-6.93
6	29.03.2008	03:26:53.67	40.591	34.795	3.9	14.3	353.53	39.67	-26.03
7	14.02.2007	11:58:23.90	39.763	34.141	3.9	18.8	349.13	38.29	-47
8	13.04.2008	02:48:17.60	40.592	34.789	3.7	14.1	352.46	25.46	-10.59
9	31.03.2008	03:36:57.38	40.593	34.791	3.7	9.9	354.82	45.86	-9.85
10	17.06.2007	23:00:36.21	41.028	33.457	3.6	14.5	335.9	54.6	29.84
11	28.02.2007	16:04:19.45	40.467	32.981	3.6	10.4	8.94	45.86	-9.85
12	07.07.2006	01:20:18.33	40.689	32.946	3.6	25.3	35.3	86.79	39.89
13	05.04.2008	09:48:41.33	40.417	34.48	3.5	9.5	349.08	44.81	-44.81
14	01.04.2008	14:01:28.45	40.588	34.797	3.5	12	347.05	26.81	-20.42
15	24.09.2007	23:20:59.98	39.769	35.465	3.5	6.8	241.76	45	0
16	16.06.2007	17:35:34.11	40.096	37.332	3.5	24.9	241.7	63.05	-13.71
17	17.11.2006	07:24:7.68	40.842	33.585	3.5	10.3	21.51	60.5	5.73
18	17.04.2008	17:35:24.62	40.416	34.466	3.4	10.9	170.72	87.42	-14.78
19	14.04.2008	15:16:0.53	39.951	35.909	3.4	9.7	219.95	44.81	44.81
20	05.04.2008	02:11:35.35	40.594	34.804	3.4	12.5	343.12	50.73	-8.29
21	02.04.2008	10:42:19.82	40.582	34.787	3.4	9.4	176.4	75.97	-20.91
22	01.04.2008	05:52:14.34	40.424	34.461	3.4	1.7	359.03	42.06	-31.11
23	31.03.2008	20:12:34.47	40.584	34.787	3.4	14.6	47.85	33.23	61.81
24	31.03.2008	18:39:28.09	40.586	34.801	3.4	12.1	152.63	73.33	-31.23
25	29.03.2008	08:31:2.15	40.595	34.804	3.4	14.8	43.07	54.37	19.53
26	22.03.2008	03:45:1.50	40.703	35.302	3.4	13.5	210.69	58.23	25.7
27	26.11.2007	00:57:56.81	41.059	35.156	3.4	10.9	27.74	69.75	52.31
28	22.04.2007	01:58:14.29	40.563	34.124	3.4	15.1	52.23	39.67	26.03
29	17.01.2007	16:37:52.94	40.081	34.397	3.4	14.1	13.26	31.61	-36.26
30	11.04.2008	15:09:18.09	40.616	34.427	3.3	18.9	141.96	17.96	-55.73
31	31.03.2008	05:26:55.87	40.585	34.8	3.3	10.3	158.02	22.27	-25.51
32	31.03.2008	03:08:40.50	40.589	34.803	3.3	10	30.47	57.2	32.73
33	18.03.2008	18:23:42.04	40.747	34.072	3.3	15.4	29.46	35.31	-7.1
34	15.03.2008	23:48:8.79	40.749	34.054	3.3	14.5	15.46	46.92	14.51
35	07.03.2008	10:34:23.02	40.462	32.989	3.3	17.8	62.05	77.05	59.13
36	22.02.2008	01:04:9.91	40.586	33.028	3.3	14.9	332.27	22.27	-62.73
37	20.12.2007	16:14:51.60	40.19	36.049	3.3	9.9	176.61	79.45	-44.01
38	07.10.2007	01:14:24.42	40.656	36.398	3.3	13.1	208.34	44.81	44.81
39	10.12.2006	20:10:40.45	40.641	35.421	3.3	14.8	223.66	44.81	35.53
40	05.12.2006	20:28:35.93	40.99	33.283	3.3	11.6	159.23	25	0
41	19.07.2006	12:53:48.10	40.792	32.989	3.3	11.8	57.25	15.79	18.02
42	22.04.2008	11:32:43.37	40.585	34.814	3.2	14.1	340.54	85.3	-69.93
43	03.04.2008	07:16:24.31	40.58	34.798	3.2	14.9	23.02	80.61	69.72

continues →

44	01.04.2008	15:57:14.58	40.592	34.78	3.2	11.4	8.3	80.34	2.61
45	31.03.2008	15:10:23.44	40.591	34.79	3.2	11.2	332.66	35.53	-30.64
46	29.03.2008	21:58:59.59	40.591	34.789	3.2	6.6	206.76	87.42	9.67
47	29.03.2008	04:56:35.60	40.594	34.796	3.2	12	356.65	31.61	-36.26
48	14.02.2008	11:38:58.97	40.727	34.826	3.2	12.1	348.77	71.25	7.1
49	02.10.2007	11:11:6.51	40.366	34.756	3.2	5.7	37.33	65.1	-84.49
50	29.09.2007	22:15:42.54	40.369	35.667	3.2	10.7	145.71	42.27	-67.37
51	25.07.2007	16:45:8.86	40.711	33.021	3.2	13.3	61.82	70.08	-84.68
52	24.06.2007	20:50:9.11	40.613	35.347	3.2	13.7	11.28	38.29	-47
53	23.04.2007	17:00:57.03	40.876	35.951	3.2	12.5	196.53	73.33	-31.23
54	11.02.2007	00:03:5.81	40.68	34.886	3.2	14	305	35	-90
55	24.09.2006	21:09:35.72	40.665	34.891	3.2	12.5	357.28	83.28	-18.88
56	13.08.2006	13:37:27.46	40.582	34.552	3.2	14.9	170.57	69.75	-52.31
57	04.08.2006	11:15:29.38	41.133	34.247	3.2	7.4	8.96	65.82	18.32
58	19.04.2008	20:38:24.16	40.787	35.905	3.1	14.6	315.93	40.26	-82.25
59	17.04.2008	18:11:45.96	40.419	34.469	3.1	3.7	192.8	61.98	11.17
60	11.04.2008	12:21:18.93	40.587	34.831	3.1	14.3	12	90	25
61	09.04.2008	20:30:43.56	40.593	34.82	3.1	11.7	9.28	87.42	14.78
62	09.04.2008	19:29:24.48	40.598	34.83	3.1	7.1	182.81	61.12	-8.5
63	05.04.2008	18:01:26.46	40.592	34.796	3.1	11.2	37.06	90	70
64	03.04.2008	21:29:38.93	40.56	34.827	3.1	27.3	21.69	47.85	39.32
65	03.04.2008	15:19:24.65	40.599	34.8	3.1	12.8	226.43	54.6	45.28
66	02.04.2008	23:51:15.01	40.425	34.472	3.1	7.2	350.07	85.3	1.71
67	02.04.2008	00:02:43.79	40.595	34.777	3.1	6.8	2.74	36.22	-13.93
68	01.04.2008	21:01:5.29	40.592	34.787	3.1	10.9	152.58	54.37	-19.53
69	01.04.2008	18:58:2.86	40.594	34.793	3.1	10.6	358.75	74.24	19.66
70	01.04.2008	01:48:35.16	40.415	34.465	3.1	13	45.77	60.13	2.88
71	03.03.2008	23:43:51.19	40.829	34.72	3.1	12.6	313.68	50.14	-56.6
72	05.02.2008	07:01:26.40	40.231	33.275	3.1	14.7	37.5	39.67	57.6
73	31.01.2008	02:47:46.71	40.224	33.284	3.1	23.3	4.1	35.31	7.1
74	22.01.2008	08:58:26.98	40.625	32.987	3.1	18.5	154.55	70.79	29.84
75	14.11.2007	12:52:36.53	40.574	35.803	3.1	8.8	337.33	26.81	-67.35
76	23.10.2007	10:54:35.02	40.91	36.661	3.1	10.4	228.28	77.05	-59.13
77	10.10.2007	22:06:30.61	40.541	36.902	3.1	4.5	161.82	48.36	-62.76
78	22.04.2007	04:38:11.71	40.559	34.118	3.1	12.6	353.53	39.67	-26.03
79	12.01.2007	03:21:49.42	40.609	33.014	3.1	11.3	198.92	60.5	-28.34
80	15.12.2006	04:09:47.37	40.6	36.893	3.1	9.5	44.98	52.84	16.01
81	13.04.2008	01:16:37.29	40.59	34.799	3	14.5	14.5	85.47	64.92
82	10.04.2008	16:22:17.21	41.013	33.482	3	11.9	327.42	42.06	31.11
83	07.04.2008	19:39:41.48	40.84	33.654	3	12.2	10.43	41.03	11.69
84	07.04.2008	17:43:18.98	40.593	34.808	3	14.4	193.25	35.31	7.1
85	05.04.2008	01:34:19.30	40.595	34.792	3	15	340.72	42.06	-31.11
86	03.04.2008	01:05:22.71	40.019	35.194	3	10.6	139.92	77.76	-54.06
87	02.04.2008	00:05:58.80	40.591	34.789	3	10.3	171.25	82.56	-13.06
88	01.04.2008	22:04:52.43	40.586	34.773	3	2.1	181.88	26.81	20.42
89	01.04.2008	20:56:44.99	40.583	34.787	3	9.5	327.23	78.56	-49.02

continues →

90	01.04.2008	00:57:31.96	40.595	34.792	3	14.4	135.23	57.39	-66.04
91	31.03.2008	19:40:28.03	40.599	34.791	3	12.9	26.31	25	0
92	30.03.2008	12:16:52.50	40.586	34.774	3	5.4	33.08	48.44	48.07
93	29.03.2008	05:50:31.49	40.588	34.798	3	10.4	26.93	61.98	49.48
94	14.02.2008	11:59:34.39	40.458	33.433	3	10.5	39.7	40.26	-5.93
95	10.02.2008	15:21:8.86	40.511	35.546	3	12.9	336.31	64.34	-16.1
96	21.11.2007	01:14:37.76	40.841	33.683	3	12.9	94.71	61.98	67.2
97	27.10.2007	03:30:20.36	40.329	35.342	3	5.2	214.43	43.96	22.18
98	10.10.2007	22:52:21.54	40.548	36.903	3	6.5	152.46	28.9	-57.62
99	09.10.2007	13:54:0.90	40.079	33.337	3	9.2	279.14	50.18	-4.18
100	03.10.2007	11:25:29.45	40.865	33.628	3	14.4	190.89	69.3	-22.21
101	18.09.2007	08:11:39.55	40.666	33.002	3	12.7	142.3	43.96	-22.18
102	06.09.2007	04:21:23.86	40.971	33.3	3	8.1	110.16	60.5	-42.39
103	17.08.2007	11:49:49.77	40.365	34.751	3	4	223.44	62.97	37.45
104	25.04.2007	07:00:27.85	41.199	35.522	3	14.5	117.07	54.6	29.84
105	22.04.2007	03:54:54.38	40.562	34.13	3	15.1	253.25	74.24	-19.66
106	09.03.2007	16:11:11.59	40.558	34.127	3	15	289.79	61.12	72.81
107	26.12.2006	17:24:41.74	41.141	33.826	3	8	359.85	22.27	62.73
108	08.12.2006	01:06v17.27	41.159	34.58	3	11.8	265.22	60.22	54.82
109	22.08.2006	20:32:51.99	40.699	33.923	3	14.3	350.95	20.59	-13.47

Table A. 7. Average P- T-, and SHmax, SHmin orientations of 109 focal mechanisms calculated in this study.

No	Lat. N (°)	Lo. E (°)	P Strike (°)	P Dip (°)	T Strike (°)	T Dip (°)	SH Max Azim.	SHMin Azim.	Regime Code
1	40.19	33.224	147.1	4.2	239	24.6	148	58	SS
2	40.59	34.802	332	31.8	227.8	21.6	144	54	UF
3	40.553	34.824	311.3	5	218.5	29.5	130	40	SS
4	40.418	34.479	348.1	58.4	226.1	18.1	143	53	NF
5	40.583	34.809	334.2	26.8	235.3	16.8	149	59	SS
6	40.591	34.795	333.5	45.7	223.8	18.2	141	51	NS
7	39.763	34.141	345.3	61.1	229.4	13.6	144	54	NF
8	40.592	34.789	337.4	44	203.7	35.6	132	42	UF
9	40.593	34.791	323.5	35.4	215.2	23.9	134	44	UF
10	41.028	33.457	282.9	5.1	188.2	42	101	11	TS
11	40.467	32.981	337.7	35.4	229.3	23.9	148	58	UF
12	40.689	32.946	161.9	24.4	266.7	29.5	169	79	UF
13	40.417	34.48	333	58.5	228.6	8.7	142	52	NF
14	40.588	34.797	338.6	47.9	206.2	31.3	131	41	UF
15	39.769	35.465	206.5	30	97	30	17	107	UF
16	40.096	37.332	202.8	28	107.5	9.9	20	110	SS
17	40.842	33.585	340	16.7	241.2	27	156	66	SS
18	40.416	34.466	125.1	12.2	217	8.5	126	36	SS
19	39.951	35.909	160.5	8.7	56.1	58.5	158	68	TF
20	40.594	34.804	302.2	27.6	209.8	3.8	121	31	SS
21	40.582	34.787	133	24.6	224.9	4.2	134	44	SS
22	40.424	34.461	342.3	47.3	227.7	21.8	146	56	UF
23	40.584	34.787	338	14.5	206	68.9	154	64	TF
24	40.586	34.801	109.2	33.6	204.9	8.5	113	23	SS
25	40.595	34.804	359.7	19.4	253.4	38.1	174	84	UF
26	40.703	35.302	161.9	7.5	64.9	42	159	69	TS
27	41.059	35.156	141.4	19.3	256.2	50	148	58	TS
28	40.563	34.124	9.5	26.3	246.9	46.8	179	89	UF
29	40.081	34.397	359.4	50.5	254.4	9.6	169	79	NS
30	40.616	34.427	182.3	58.5	24.7	29.5	124	34	NF
31	40.585	34.8	159.3	50.3	18.8	32.6	125	35	UF
32	40.589	34.803	337.1	3.5	243.5	44.8	156	66	TS
33	40.747	34.072	9.5	41.3	244.6	31.6	171	81	UF
34	40.749	34.054	324.8	10.7	226.4	38.1	142	52	SS
35	40.462	32.989	174.4	28.5	302.1	48.3	7	97	UF
36	40.586	33.028	16.3	63.2	221.4	24.6	137	47	NF
37	40.19	36.049	126.6	37.8	233.7	20.7	137	47	UF
38	40.656	36.398	145.6	15.6	39.3	45.4	140	50	TS
39	40.641	35.421	178.4	19.4	64.4	49.8	171	81	TS
40	40.99	33.283	136.3	39.9	2.1	39.9	114	24	UF
41	40.792	32.989	26.3	38.4	235.7	47.7	4	94	UF

continues →

42	40.585	34.814	271	46	52.8	37.2	122	32	UF
43	40.58	34.798	129.9	32.6	270.4	50.3	147	57	UF
44	40.592	34.78	323.5	5	232.7	8.7	144	54	SS
45	40.591	34.79	322.2	50.9	203.8	20.3	123	33	UF
46	40.591	34.789	341.2	5	71.9	8.7	161	71	SS
47	40.594	34.796	355.2	55.2	228.5	22.5	148	58	NF
48	40.727	34.826	123.9	2.7	212.3	4.3	124	34	SS
49	40.366	34.756	318.5	69.4	123.2	19.9	30	120	NF
50	40.369	35.667	147.3	74.2	39.9	4.8	131	41	NF
51	40.711	33.021	340.6	64.5	147.7	24.9	55	145	NF
52	40.613	35.347	7.4	61.1	251.5	13.6	166	76	NF
53	40.876	35.951	153.1	33.6	248.8	8.5	157	67	SS
54	40.68	34.886	47.7	79.9	218	10	128	38	NF
55	40.665	34.891	311.4	26.2	41.4	1.3	131	41	SS
56	40.582	34.552	123.2	50.3	233.8	16.3	137	47	NS
57	41.133	34.247	322.3	5.4	228.9	31.9	141	51	SS
58	40.787	35.905	355.1	82.9	220.4	5	130	40	NF
59	40.419	34.469	325.9	3.2	55.7	19.6	146	56	SS
60	40.587	34.831	144.2	12.9	238.9	20.4	146	56	SS
61	40.593	34.82	143.2	1.8	233.8	10.4	143	53	SS
62	40.598	34.83	145	29.8	45	16.6	139	49	SS
63	40.592	34.796	145.9	41.6	288.2	41.6	173	83	UF
64	40.56	34.827	325.2	8.2	223.9	53.8	142	52	TF
65	40.599	34.8	167	2.5	73.4	51.9	166	76	UF
66	40.425	34.472	125	0.4	215	4.3	125	35	SS
67	40.595	34.777	340.5	42.2	221.7	28	144	54	UF
68	40.592	34.787	119.3	37.2	19.5	12.7	113	23	SS
69	40.594	34.793	130.5	2.1	221.5	24.9	131	41	SS
70	40.415	34.465	5.4	14.1	269.4	23.8	2	92	SS
71	40.829	34.72	290.8	65	20.8	0	111	21	NF
72	40.231	33.275	330.3	7.1	219.1	71	148	58	TF
73	40.224	33.284	329.7	31.8	209.8	38.9	136	46	UF
74	40.625	32.987	282.6	5.7	16.5	34.4	105	15	SS
75	40.574	35.803	21.4	67.7	230.5	19.7	145	55	NF
76	40.91	36.661	174.5	48.3	293.1	23	14	104	UF
77	40.541	36.902	142.9	70	52.9	0	143	53	NF
78	40.559	34.118	335	47.9	220.9	20.2	139	49	UF
79	40.609	33.014	163	39.8	70.4	3.2	161	71	NS
80	40.6	36.893	0.9	21.1	250	42.3	173	83	UF
81	40.59	34.799	126.1	35.6	259.9	44	145	55	UF
82	41.013	33.482	279.6	19.8	162.1	51.5	92	2	UF
83	40.84	33.654	330.9	26.1	217.6	38.9	141	51	UF
84	40.593	34.808	166.5	34.7	36	42.5	149	59	UF
85	40.595	34.792	336.1	52.6	204	26.5	126	36	NF
86	40.019	35.194	86	45.2	202.9	24.2	103	13	UF
87	40.591	34.789	127.4	4.5	217.1	11	128	38	SS

continues →

88	40.586	34.773	142.8	31.3	10.3	47.9	128	38	UF
89	40.583	34.787	275.5	41.6	27.1	22.5	109	19	UF
90	40.595	34.792	94.5	67.7	208.3	9.4	115	25	NF
91	40.599	34.791	359.8	35.1	228.9	43	162	72	UF
92	40.586	34.774	331.4	4.3	234	59.6	150	60	TF
93	40.588	34.798	143	10.2	246.8	53	147	57	TF
94	40.458	33.433	10.7	37.4	257	27.8	178	88	UF
95	40.511	35.546	297.2	32.3	206.4	1	117	27	SS
96	40.841	33.683	202.7	9.5	320.7	70.6	26	116	TF
97	40.329	35.342	164.7	16.7	58.2	43.9	159	69	TS
98	40.548	36.903	178	65.2	38.8	19.3	135	45	NF
99	40.079	33.337	243.3	29.5	138.4	24.4	55	145	UF
100	40.865	33.628	150	30	60	0	150	60	SS
101	40.666	33.002	117.8	44	8.5	18.9	106	16	NS
102	40.971	33.3	73.6	44.5	168.5	5.1	77	167	NS
103	40.365	34.751	342.2	12	81	37.5	166	76	SS
104	41.199	35.522	62.8	8.4	328	38.9	60	150	SS
105	40.562	34.13	204.8	17.1	304.7	8.5	30	120	SS
106	40.558	34.127	32.2	14.5	164.3	68.9	36	126	TF
107	41.141	33.826	293.8	22.2	140.4	65.5	109	19	TF
108	41.159	34.58	19.5	8.7	123.9	58.5	23	113	TF
109	40.699	33.923	343.1	46	201.3	37.2	132	42	UF

APPENDIX B

Outputs of calculated focal mechanisms in this study.